A Study of Indoor Ultra-wideband Propagation Measurement and Characterization

By

Ahmet Bayram

Time Domain and RF Measurement Laboratory

Thesis Submitted to the Faculty of

The Bradley Department of Electrical and Computer Engineering
Virginia Polytechnic Institute and State University

In partial fulfillment of the requirements for the degree of

MASTER OF SCIENCE
In
Electrical Engineering

Chairperson
Dr. Ahmad Safaai-Jazi

Committee Members
Dr. William A. Davis　　Dr. Sedki M. Riad
Dr. Brian D. Woerner

May 13th, 2004
Blacksburg, Virginia

Keywords: *UWB antennas, Indoor Propagation, Path Loss, Frequency-Domain Measurement Technique, Signal Distortion.*

A Study of Indoor Ultra-wideband Propagation Measurement and Characterization

By

Ahmet Bayram

Prof. Ahmad Safaai-Jazi, Chairperson
Electrical Engineering

(Abstract)

Ultra-wideband (UWB) communication is emerging as a new wireless technology, which promises high data rates with low interference and low power consumption. The development of such UWB systems requires a sufficiently large amount of data to characterize the propagation behavior of UWB signals in indoor environments and develop accurate channel models. This thesis focuses primarily on a frequency-domain approach for propagation measurements and characterization of indoor UWB channels. This approach is based on measurements of the amplitude using a scalar network analyzer and retrieval of the phase from the amplitude data using a Hilbert transform relationship.

Extensive propagation data are collected in a frequency range of 1 to 12 GHz in two buildings on Virginia Tech campus. Using the data, channel characterization results are obtained and compared to those based on time-domain measurements. Some statistical results for small-scale fading, path loss exponent, and signal quality are presented. This comparison validates the accuracy of measured results for the UWB measurement campaign. The measured data also reaffirms the immunity of UWB propagation to small-scale fading which is present in narrowband wireless communication systems.

In addition to channel propagation measurements, signal distortions in UWB links, due to bandwidth limitations of antenna characteristics as well as the dispersive behavior of building materials, are also examined. In particular, the distortion of radiated signals by TEM horn antennas along off-boresight directions are studied experimentally. Furthermore, pulse distortions resulting from propagation through dispersive walls are demonstrated by simulation. The roles of receive-transmit antennas in a UWB link are examined, and the requirements for gain, input impedance, polarization, and phase of the radiated signal necessary for minimization of signal distortions are pointed out.

Contents

Acknowledgements

I would like to praise God for His unscathed donation of belief and empowerment upon myself not only in course of this work towards my Master's degree but throughout my entire life.

I ought to convey my gratitude to Dr. Ahmad Safaai-Jazi at this moment for his unending yet always encouraging critics and guidance. Without him, my work at Virginia Polytechnic Institute and State University would be nothing but mundane. I would like to thank him for his belief in me. I also would like to thank Dr. Sedki M. Riad for providing help whenever needed and making me a part of Time Domain and RF Measurement Laboratory (TDL), a lab where friendship and superior work go hand in hand. I would like to thank other members of my committee, Dr. Brian D. Woerner and Dr. William A. Davis, for being an integral part of this work.

Without the friendship and the help of Dr. Ahmad M. Attiya and Dr. Ali H. Muquaibel, with whom I have worked for the last several years at TDL, would this work reach to this level, nor could there be any publications. I feel grateful to be able to work with such brilliant engineers and yet powerful characters. I also would like to thank Rachad, my colleague at TDL, and Randall Nealy from VTAG for his contributions to this thesis.

I should mention that without my family I would not even be where I am now. I am very blessed to have such a family and thank them with all my heart for their never-ending help and support for me in every aspect of life. I thank my dad, my mom, my brother Saffet, my sister Tekıye, and my beloved grandparents – you all have been inexplicably splendid in guiding me to the right path and giving me any support I thrived for. Although my grandmother passed away last year on my birthday, I know you are always with me in my heart. I should also convey my gratitude for my dearest cousins who provided any help and time when needed.

I would also like to express my deep gratitude to my best friends who are all over the USA and rest of the world and especially to greatest friends in Blacksburg, VA who made my stay here a memorable and valuable experience. I should thank Burç, Cem, Őzgű, Umur, Rahmi, and Umut and many others that I cannot list here for their help and time. I would like to mention my gratitude to Ídil, without her I could not succeed as much in life. I should also mention my gratefulness to Selen, my ex-fiancé, and her family, who have always been supportive of me in all aspects of my life.

This work was partly supported by Defense Advanced Research Projects Agency (DARPA) under DARPA/NETEX program.

List of Tables

List of Figures

Chapter 2

Chapter 3

Chapter 4

Chapter 5

Appendix A

Appendix B

Appendix C

Appendix D

CHAPTER 1

Introduction

Ultra-wideband (UWB) communication systems are highly promising because of their potentials for high data rate information transmission with low power consumption and low interference. UWB systems are deemed to bring about major changes to wireless communications within this decade. These systems can be good candidates for many indoor communication applications such as local area networks, wireless phone, security systems, etc. Applications such as high-resolution radar detection, precision location, and tracking systems comprise other targeted uses of this technology. Unlike the prevalent narrowband systems based on continuous sine-wave carriers, UWB systems use short duration pulses for transmission of information. The narrowband technology is nowadays approaching a state of saturation in bandwidth and channelization, whereas the UWB technology offers the potential for a much larger number of users distributed over an enormous bandwidth. In February 2002, the Federal Communications Commision issued a First Report and Order authorizing the commercial deployment of the UWB technology. This authorization marked an upsurge of interest and research activities in UWB communications worldwide.

Although Rayleigh or multipath fading is a continuous-wave phenomenon to which UWB signals are much less prone, the performance of UWB systems should be thoroughly tested in order to attain accurate channel models and thus develop efficient and optimum designs. For instance, the proposed rake receiver architecture, coherently adding multipath energies at the receiving point, would improve the signal-to-noise ratio (SNR). Therefore, the channel characterization of UWB signals in in-building as well as outdoor environments becomes inevitable. However, in order to perform the channel characterization of a UWB system in its entirety, it is imperative to scrutinize its constituent components individually. That is, one should examine the transmitting and receiving antennas, the transmission medium and the impacts of various building materials on the UWB signal propagation, the characteristics of the channel, and modulation/coding schemes. In this thesis, attention will be focused on some antenna issues, indoor channel measurements, and channel characterization.

The development of such UWB indoor communication systems requires the availability of ample data to characterize the propagation behavior of UWB electromagnetic signals in indoor environments. Also, efficient design of UWB systems calls for comprehensive and accurate channel models which, in turn, can be developed based on extensive propagation measurement data. Channel propagation measurements may be carried out using a variety of techniques which can be broadly divided into two groups, time-domain and frequency-domain methods. Recently, the Time-Domain and RF Measurement Laboratory of Virginia Tech conducted a UWB propagation measurement campaign, using both time-domain and frequency-domain techniques. This thesis focuses primarily on the frequency-domain approach and related results of the measurement campaign. Frequency-domain results for path loss parameters and signal quality are compared to those obtained from time-domain measurements. This comparison validates the accuracy of frequency-domain measurements and confirms the channel characterization results.

In addition to channel propagation measurements, signal distortions in UWB links are also examined. Such distortions can be attributed to two sources; namely, the antennas which constitute an integral part of wireless communication links, and the propagation medium. Radiation of UWB signals by simple antennas such as dipoles and the nature of distortions caused by the antennas are discussed. Also, the distortion of UWB signals due to dispersive properties of building materials (such as brick, blocks, drywall, etc) and their internal geometry (such as holes in bricks and blocks) are addressed. These distortions, which are negligible for narrowband signals, are separate from multipath effects present in both narrow-band and UWB systems.

In Chapter 2 a literature review of existing antennas intended for UWB applications along with their underlying theory and characterization are presented. The role of antennas in communication systems, especially in UWB systems, is emphasized. The characterization of the antennas used in the UWB measurements conducted at Virginia Tech is addressed. Chapter 3 reviews the main measurement techniques; namely, time-domain and frequency-domain methods. The details of the frequency-domain technique, the method selected for indoor channel measurements in this work, are examined more thoroughly. In Chapter 4, the measurement setup and the results for indoor UWB channel measurements are discussed. Several UWB characteristics of the measured channels such as path loss and signal quality for different scenarios are computed and discussed. Chapter 5 discusses significant components of signal distortion due to UWB antennas and the propagation medium. Finally, Chapter 6 summarizes the conclusions of this research and points out directions further work that can be undertaken.

CHAPTER 2

UWB Antennas

Antennas, from very early times of wireless communications, have been an indispensable component of communication links. A thorough understanding of antennas is required for further improving the efficiency of the UWB technology. Although not many commercial UWB antennas have been introduced so far, it is not unrealistic to see the emergence of a market driven by this technology in the near future. It is, nowadays, fully recognized that for practical implementation of UWB systems, efficient, ultra wideband antennas are required. An ideal UWB antenna should maintain a frequency-independent input impedance and produce a radiated electromagnetic field whose magnitude, phase and polarization satisfy certain requirements over the UWB frequency range in order to prevent distortions in radiated signals. In the following sections, first a brief literature survey of antennas intended for UWB applications is presented. Then, the required antenna characteristics for UWB applications are further discussed. Characterization of a well-known UWB antenna; namely, the TEM horn, which is extensively used in our indoor measurements, is also addressed.

2.1. Literature Survey

Although UWB antennas have only recently found applications in wireless communication, they have been researched and developed for pulsed radar and other specialized applications for several decades. This brief survey focuses only on the recent developments of UWB antennas.

Picosecond Pulse Lab (PSPL) has been involved in the design of UWB antennas since the early implementations of such systems [Pic03]. PSPL offers several different types of antennas, including discone and two types of monopoles. The discone antenna may be viewed as one-half of a truncated biconical transmission line, which is known to have a constant characteristic impedance at all frequencies. The second antenna is a common monopole which is essentially a simpler version of the discone with the cone half-angle reduced to zero. The third antenna is a modified monopole, called d*dot probe antenna, that behaves as a capacitor within a frequency range. Taniguchi *et. al.* have examined a variety of antennas for UWB applications, including bicone, finite monocone (or discone), and a volcano smoke antenna, and also proposed an omni-directional, low-VSWR antenna with a maximum gain of around 5 dBi in a region scanned between 40° and 70° and operating over a frequency range of 2 to 10 GHz.[Tak02]. Another type of wideband antenna has been reported by Agrawall *et. al.* which is a circular or elliptical disc monopole [Agra98]. This design was intended for achieving a wide impedance bandwidth.

Yarovoy *et. al.* introduced a novel modification to TEM horn by incorporating a dielectric wedge into the antenna structure [Yar02]. This antenna was intended for mainly ground penetrating radar (GPR) applications. Its bandwidth lies in lower gigahertz range; however, its efficiency increases significantly due to the tapering of field profile. Another modification to TEM horn has been proposed by Nguyen *et. al.*, who have designed this antenna using microstrip technology [Ngu01]. The fabrication can be implemented on a single substrate by a photolithographic process, and there is no need for baluns or transition units. They have reported a high gain in an almost 20 GHz of measured bandwidth. The concept of TEM horn has been used by Chevalier *et. al.* to design and fabricate resistively loaded wire antennas with the capability of producing uniform electric field [Chev99]. These antennas consist of four wires arranged in a horn-like structure. Baluns are needed for impedance transformation and matching. Esselle *et. al.* have applied the resistive loading technique on a thin-film V-monopole to achieve a constant gain and linear phase variations over a frequency range of 22 MHz to 1.1 GHz [Esse91]. This antenna was then tested successfully in receiving a 520 ps electromagnetic pulse over an angular range of up to 45° from the boresight direction.

Aurand has carried out extensive work on a TEM horn antenna with a dielectric lens [Sand96]. This TEM horn was designed for very short pulse (10s of picoseconds) propagation applications, UWB channel measurements, and ultra-wideband material characterization. The antenna provides about 10 GHz of bandwidth. Another TEM horn was introduced in 1978 by researchers at the National Bureau of Standards (NBS) [Law78]. The TEM horn exhibited good performance between 100 MHz and 6 GHz. Similar TEM horn antennas with a performance close to that of Aurand have also been fabricated in the Time Domain and RF Measurement Laboratory (TDL) of Virginia Tech, and have been extensively used in this and other works.

Time Domain Corporation has also been involved in manufacturing of UWB antennas. The BroadSpec antenna, a product of Time Domain Corporation, is claimed to work efficiently between 1.5 GHz and 6 GHz [TDC01]. Another product by Time Domain Corporation intended for UWB applications is the diamond dipole that is essentially an inverted bow-tie antenna with triangular elements [Sch01]. It has nearly an omni-directional radiation pattern except for the usual dipole-related null on the axis of the antenna.

Impulse radiating antennas (IRAs) are also desirable candidates for UWB communication systems. Farr *et. al.* provide details about the design and testing of a lensed IRA with a TEM structure of aperture diameter 61 cm [BaFa95],[BaFa93].

Wicks *et. al.* have introduced a novel design as a polarization diversity antenna for use in UWB systems [Wick93]. This antenna is comprised of a truncated conical ground plane with four radiating elements. The antenna has similar properties as a TEM horn. By varying the size of the antenna, different wideband frequency ranges were tested, and satisfactory gain results were measured over a range of 0.5 to 18 GHz.

The analysis of UWB antennas has also attracted considerable attention. Mikheev *et. al.* has proposed an approximate solution for pulse radiation by a TEM horn array by modeling the horn structure as an ensemble of V-antennas suggested by Podosenov *et. al.* [Mikh01],[Pod96]. Another analysis of radiation by TEM horns is carried out by Shlager *et. al.* [Shla96]. They carry out their analysis using the finite-difference time-domain (FDTD) technique and provide comparisons with experimental results for two different TEM horn antennas. The FDTD method is also used by Manoley *et. al.* in order to accurately analyze different antennas designed for pulse radiation [Mal93]. Some of the antenna types included in their work are parallel-plate radiators and conical monopoles. The numerical results exhibit very close agreement with experimental measurements.

Attiya *et. al.* have proposed a simple model for analyzing TEM horns in the receiving mode by considering a horn as an array of V-dipoles [Attiy03]. Their analysis gives a closed form current distribution induced by an arbitrary incident pulsed plane wave. They also show close agreement with experimentally obtained received pulses. Attiya *et. al.* base their analysis on the work by Smith who has carried out a time-domain analysis of simple wire receiving antennas with plane-wave excitation [Smit02]. Another perspective on UWB antenna reception is presented by Robertson *et. al.* [Rober95]. They introduce frequency-dependent effective length, which in turn is used to define the gain of the antenna.

Much effort has also been devoted to characterization of antennas. Boryssenko has characterized monopole and dipole antennas designed for pulse radiation as examples [Bory99]. The paper by Allen *et. al.* provides closed form expressions for many parameters involved in antenna characterization in the time domain [Ond93]. They have specified that fidelity of the transmission or reception in the frequency domain is contingent upon two formidable restrictions: one being the flat amplitude response and second being the linear behavior of the phase, both over the frequencies of operation. On the other hand, fidelity of the transmission or reception in the time domain is waveform specific. That is, for transmission, fidelity is the measure of antenna's capability to reproduce the voltage applied to the antenna terminals as the integral of the transmitted field. Similarly, for reception, it is the measure of ability to reproduce the incident field as received voltage at the antenna terminals [Ond93], [Kand86]. This explains clearly why some waveforms may result in much worse fidelity for the same antenna structure, and that the time-domain characterization does provide better insight about an antenna's performance. Allen *et. al.* also consider the energy content of the received or transmitted signal resulted from arbitrary excitation of an antenna structure. They subsequently summarize many parameters as a function of the excitation waveform in closed forms. The parameters include directivity, fidelity, radiation resistance, antenna beam solid angle, effective area, gain, polarization, radiation efficiency, and effective height. They have provided experimental results using a short pulse with a full-width half-maximum (FWHM) of 400ps and a set of TEM horns as well as a set of resistively loaded TEM horns. The results contain fidelity and pattern plots.

2.2. Role of Antennas in UWB Links

Radiation of UWB signals by antennas requires a treatment different from that of narrow-band signals. In this section, we provide an overview of signal propagation in a UWB link and explain the role of the antenna as a transmitter or as a receiver and its impact on the signal. Figure 2.1 illustrates the schematic of the transmitter circuit of the link. The information source is modeled as a voltage source V_g with an internal impedance Z_g. The information signal, say in the form of a train of short pulses, is carried to a transmit antenna by means of a transmission line with characteristic impedance Z_o, complex propagation constant $\gamma_o=\alpha_o+j\beta_o$, and length l. The radiated signal, after traveling some distance away from the transmitter, reaches the receive antenna located in the far-field of the transmit antenna. The receive antenna picks up the radiated

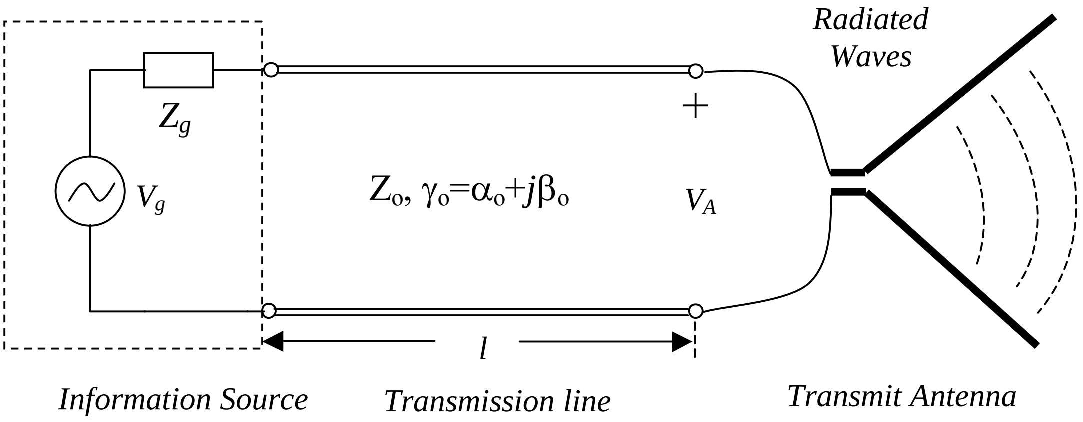

Figure 2.1 The schematic of the transmitter side of a communication link.

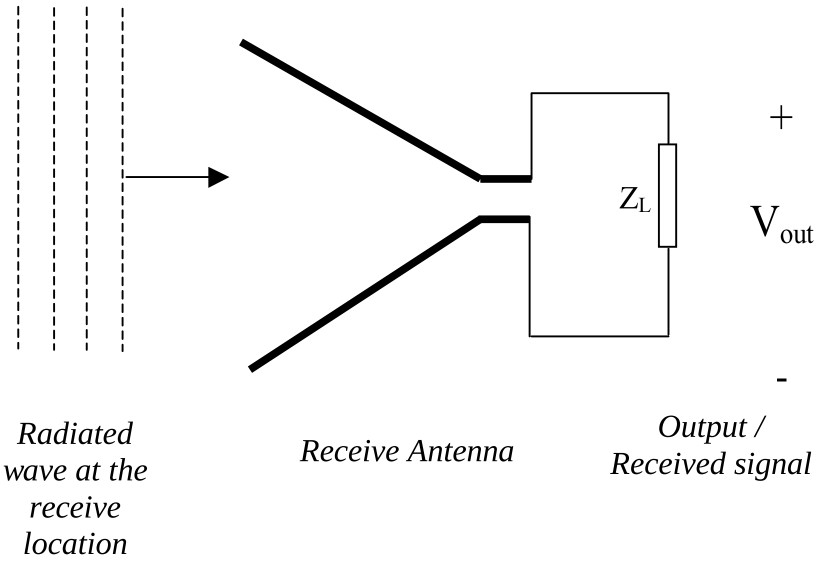

Figure 2.2 The schematic of the receiver side of link.

wave and produces a voltage signal as its output. The circuitry and hardware involved in the receiver side following the antenna are modeled as a load impedance Z_L. Figure 2.2 illustrates the schematic of the receiver side of the link.

The signal source and the transmission line, seen at the input of the transmit antenna, can be modeled as a voltage source $\overline{V_g}$ with an internal impedance $\overline{Z_g}$ using the Thévénin equivalent concept, while the transmit antenna is modeled as an impedance load $Z_A = R_A + jX_A$ which is, in fact, the antenna input impedance. The circuit model of the transmit side of the link is shown in Figure 2.3. Using the transmission line theory, it can be shown that

$$\overline{V_g} = V_g \frac{Z_o}{Z_o \cosh(\gamma_o l) + Z_g \sinh(\gamma_o l)}, \tag{2.1}$$

$$\overline{Z_g} = Z_o \frac{Z_g + Z_o \tanh(\gamma_o l)}{Z_o + Z_g \tanh(\gamma_o l)}. \tag{2.2}$$

When $Z_g = Z_o$, transmission line is matched to the signal generator. In this case, (2.1) and (2.2) reduce to

$$\overline{V_g} = V_g . e^{-\gamma_o l} = V_g . e^{-\alpha_o l} e^{-j\beta_o l}, \tag{2.3}$$

$$\overline{Z_g} = Z_o . \tag{2.4}$$

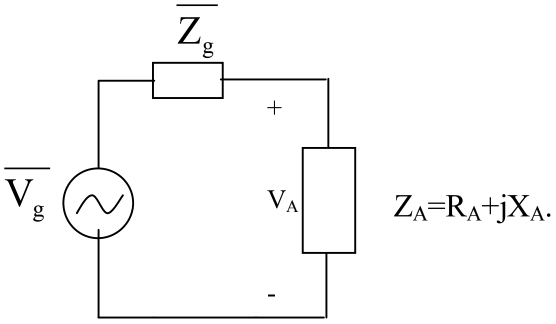

Figure 2.3 Equivalent circuit of the transmit side of link.

Under this condition, the radiated power will be maximum if $Z_A = Z_0^* = \overline{Z}_g^*$. In many practical situations, Z_g, Z_o, and $\overline{Z_g}=Z_o$ are real, thus if Z_A is not real, a matching unit will be needed between the antenna and the transmission line in order to maintain maximum transfer of power to the antenna. For narrowband signals, matching can be achieved relatively easily. However, for ultra-wideband signals, maintaining a constant antenna input impedance over the ultra-wide bandwidth of the signal is a challenging task. If the antenna used for radiating the UWB signal is not matched to the transmission line and its input impedance is frequency dependent, the signal entering the antenna suffers distortions. Thus, antenna impedance mismatch is the first source of signal distortion in a UWB link. The extent of distortions depends on the nature of the frequency dependence of the real and imaginary parts of the antenna input impedance. In addition to signal distortion, antenna impedance mismatch also results in the reduction of radiated power. The reduction factor is $\Gamma = |(Z_A - Z_0)/(Z_A + Z_0)|^2$, which is in fact the power reflection coefficient. Further distortions due to other antenna characteristics may also occur as discussed below.

In order to examine other signal distortions caused by the antenna, we examine the radiation of the information signal by the transmit antenna. Here, we assume that the antenna is matched to the transmission line which itself is assumed to be distortionless. Accordingly, the antenna input voltage $v_A(t)$ is, apart from some attenuation and delay, identical to the original information signal. That is,

$$v_A(t) = \frac{1}{2} e^{-\alpha_o l} v_g(t - \frac{l}{v_0}), \ v_o = \frac{\omega}{\beta_o}. \tag{2.5}$$

The voltage $v_A(t)$, compared to $v_g(t)$ that represents the information signal, is delayed by the amount l/v_0 and is attenuated by the factor $e^{-\alpha_0 l}/2$. This voltage results in an input current $i_A(t) = v_A(t)/Z_0$, which in turn establishes a current distribution $\vec{J}(\vec{r}';t)$ on the antenna structure.

The current distribution $\vec{J}$ gives rise to electromagnetic fields $\vec{E}(\vec{r};t)$ and $\vec{H}(\vec{r};t)$ which are governed by Maxwell's equations. The solutions for $\vec{E}(\vec{r};t)$ and $\vec{H}(\vec{r};t)$ can be obtained by two approaches: (i) using a time-domain technique such as FDTD (Finite-Difference Time-Domain), (ii) using a frequency-domain technique and inverse Fourier transforming the solutions to the time domain. The latter technique can be formulated more conveniently and is discussed further below.

We begin by considering a sinusoidal input signal of frequency ω. This has a phasor representation as $e^{j\omega t}$. The resulting far-field solutions for the electric field $\vec{E}_1$ is obtained as

$$\vec{E}_1\left(\vec{r};t;\omega\right) = -j\omega\mu\frac{e^{j(\omega t-\beta r)}}{4\pi r}\vec{P}_1\left(\theta,\varphi\ ;\omega\right), \tag{2.6}$$

where

$$\vec{P}_1\left(\theta,\varphi\ ;\omega\right) = \vec{P}\left(\theta,\varphi\ ;\omega\right) - [\vec{P}\left(\theta,\varphi\ ;\omega\right).\hat{r}]\hat{r}, \tag{2.7}$$

$$\vec{P}(\theta,\phi\ ;\omega) = \int_{V'}\vec{J}(\vec{r}';\omega)e^{j\beta\vec{r}'.\hat{r}}dv'. \tag{2.8}$$

If the current distribution in (2.8) is of surface or filamentary type, $\vec{J}(\vec{r}';\omega)dv'$ is replaced by $\vec{J}_s(\vec{r}';\omega)ds'$ or $I(\vec{r}',\omega)d\vec{l}'$, respectively and the volume integral becomes a surface or line integral. Also, in (2.6) to (2.8) $\beta = \omega\sqrt{\mu_0\varepsilon_0} = \omega/c$ in free space and $\vec{r}$ and $\vec{r}'$ are position vectors for the observation and source points.

If the antenna input current, instead of being sinusoidal, has an arbitrary time variation described by $f(t)$ the corresponding time-domain radiated electric field can be obtained by means of the inverse Fourier transformation. The result is

$$\vec{E}\left(\vec{r};t\right) = -\frac{\mu}{4\pi r}\int_{-\infty}^{\infty}\frac{1}{2\pi}j\omega F\left(\omega\right)\vec{P}_1\left(\theta,\varphi\ ;\omega\right)e^{j(\omega t-\beta r)}d\omega, \tag{2.9}$$

where $F\left(\omega\right) = \Im\left\{f\left(t\right)\right\}$. Introducing $\vec{G}(\theta,\varphi;\omega) = F(\omega)\vec{P}_1(\theta,\varphi;\omega)$, this result may be cast into a more suitable form as

$$\vec{E}\left(\vec{r};t\right) = -\frac{\mu}{4\pi r}\frac{\partial}{\partial t}\left[\vec{g}\left(\theta,\varphi\ ;t-{r}/{c}\right)\right], \tag{2.10}$$

where $\vec{g}\left(\theta,\varphi\ ;t\right)$ is the inverse Fourier Transform of $\vec{G}\left(\theta,\varphi\ ;\omega\right)$.

Before discussing the significance of (2.10), it is helpful to show how this result can be derived. In doing so, a system approach is employed. The transmit antenna is regarded as a linear system as illustrated in Figure 2.4. The linearity of this system is based on the fact that the governing Maxwell's equations are linear. When the input signal to this system is $e^{j\omega t}$ the output radiated electric field is $\vec{E}_1\left(\vec{r};t;\omega\right)$ given by (2.6). Since the system is linear, the response to the input $a\,e^{j\omega t}$, where a is a constant (with respect to spatial variables r,θ,ϕ), is $a\,\vec{E}_1\left(\vec{r};t;\omega\right)$. We choose this constant to be $a = F(\omega)/2\pi$. Once again, the linearity property of the system allows us to integrate both the input and the output of the system with respect to ω over an arbitrary range of ω. We choose this range to be from $-\infty$ to $+\infty$. Accordingly,

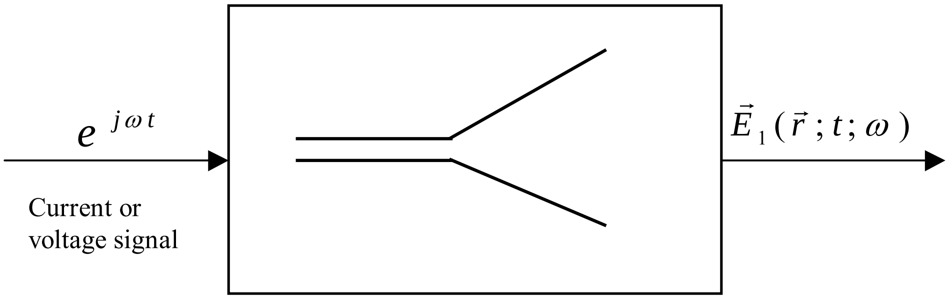

Figure 2.4 A system representation of transmit antenna

$$e^{j\omega t} \;\Rightarrow\; \vec{E}_1(\vec{r};t;\omega), \tag{2.11a}$$

$$\frac{1}{2\pi}F(\omega)e^{j\omega t} \;\Rightarrow\; \frac{1}{2\pi}F(\omega)\vec{E}_1(\vec{r};t;\omega), \tag{2.11b}$$

$$\int_{-\infty}^{\infty}\frac{1}{2\pi}F(\omega)e^{j\omega t}d\omega \;\Rightarrow\; \int_{-\infty}^{\infty}\frac{1}{2\pi}F(\omega)\vec{E}_1(\vec{r};t;\omega)d\omega. \tag{2.11c}$$

However, if $F(\omega)$ is chosen to be the Fourier transform of $f(t)$, then the left-hand-side of (2.11c) is indeed $f(t)$ and the right-hand-side of it will be the response of the system to the input $f(t)$. In other words, the radiated electric field of the antenna to an arbitrary input signal $f(t)$ is

$$f(t) \;\Rightarrow\; \vec{E}(\vec{r};t) = \int_{-\infty}^{\infty}\frac{1}{2\pi}F(\omega)\vec{E}_1(\vec{r};t;\omega)d\omega \tag{2.12a}$$

$$=\int_{-\infty}^{\infty}\frac{1}{2\pi}F(\omega)[j\omega\mu\frac{e^{j(\omega t-\beta r)}}{4\pi r}\vec{P}_1\left(\theta,\varphi\ ;\omega\right)]d\omega \tag{2.12b}$$

$$=\frac{\mu}{4\pi r}j\omega\int_{-\infty}^{\infty}\frac{1}{2\pi}\vec{G}(\theta,\phi\ ;\omega)e^{j(\omega t-\beta r)}d\omega \tag{2.12c}$$

$$=\frac{\mu}{4\pi r}\frac{\partial}{\partial t}\vec{g}(\theta,\phi\ ;t)\,. \tag{2.12d}$$

After obtaining the electric field from (2.12), the associated magnetic field is calculated from

$$\vec{H}(\vec{r};t)=\frac{1}{\eta}\hat{r}\mathrm{X}\vec{E}(\vec{r};t)\,, \tag{2.13}$$

where $\eta=\sqrt{\mu_0/\varepsilon_0}$ is the intrinsic impedance of free space.

Next, we explore the requirements for distortionless radiation of the input signal by the transmit antenna. We first consider the case when $\vec{P}_1\left(\theta,\varphi\ ;\omega\right)$ does not vary with frequency and is real; that is, $\vec{P}_1\left(\theta,\varphi\ ;\omega\right)=\vec{P}_0(\theta,\phi)$, then

$$\vec{E}\left(\vec{r};t\right)=-\frac{\mu}{4\pi r}\vec{P}_0(\theta,\phi)\frac{\partial}{\partial t}f\left(t-{r}/{c}\right). \tag{2.14}$$

Under this condition, the radiated field is proportional to the first time-derivative of the antenna input signal. The differentiation, for example, modifies a Gaussian monopolar pulse to a bipolar one. Although, strictly speaking, any deviation from the original signal other than attenuation and delay, amounts to distortion, the mere differentiation should not be regarded as distortion, as the exact replica of the original signal can be constructed through an integration process (although in practical situations such integration is not required). But, what are the implications of $\vec{P}_1\left(\theta,\varphi\ ;\omega\right)$ being frequency independent? Since $|\vec{P}_0\left(\theta,\varphi\right)|$ represents the radiation pattern of the antenna, the implication is that the antenna has a frequency-independent directive gain. It is known that wideband antennas provide nearly a constant gain over a large frequency range. However, the question is whether constant gain is sufficient to prevent distortion. To answer this question, we note that if $\vec{P}_1\left(\theta,\varphi\ ;\omega\right)$, which is generally complex, has only a frequency-independent magnitude but its phase varies with frequency nonlinearly, the antenna would still provide a constant directivity over a wide bandwidth; however, the frequency dependent phase of $\vec{P}_1\left(\theta,\varphi\ ;\omega\right)$ results in distortions in the radiated signal as implied from (2.12b). Consequently, antennas with wide gain bandwidth such as log-periodic, helical, and spiral antennas are not necessarily suitable candidates for UWB applications. If the phase of $\vec{P}_1(\theta,\varphi\ ;\omega)$ varies with frequency linearly, then the effect in the time-domain will be merely a delay.

In summary, if an antenna, over the bandwidth of a UWB signal, has a constant input impedance and produces radiation fields with constant magnitude and linearly varying phase versus frequency, its impact on the signal is limited only to delay and time differentiation. The polarization of an antenna may yet be another source of distortion. But, this happens in conjunction with the receive antenna.

In order to illustrate the impact of bandwidth-limited antennas on UWB signals, we analyze the radiation of a Gaussian pulse by a simple antenna such as a dipole of length *L*. The input current to the dipole is assumed to vary with time as $f(t)=\exp(-t^2/2\sigma^2)$. Assuming a sinusoidal current distribution on the dipole wire, the expression for $\vec{P}_1(\theta,\varphi\ ;\omega)$ is given as [Stutz98].

$$\vec{P}_1(\theta,\varphi;\omega)=\frac{c}{\omega}\frac{\cos\left(\frac{\omega L}{2c}\right)-\cos\left[\frac{\omega L}{2c}\cos\theta\right]}{\sin\theta}\hat{\theta}. \tag{2.15}$$

Clearly, the magnitude of $\vec{P}_1(\theta,\varphi\ ;\omega)$ varies with frequency and the radiated signal will suffer distortions if the signal bandwidth exceeds the bandwidth of the dipole. Let us assume that the dipole length is L=1 m, and σ=1 μsec, 0.1μsec, 0.01μsec. For σ=1 μsec and 0.1μsec, the dipole is short compared to all wavelengths in the signal bandwidth. Thus, $\omega L/2c \ll 1$ and using the approximations

$$\cos(\omega L/2c)\approx 1-(\omega L/2c)^2, \tag{2.16a}$$

$$\cos[(\omega L/2c)\cos\theta]\approx 1-(\omega L/2c)^2\cos^2(\theta/2), \tag{2.16b}$$

(2.15) reduces to

$$\vec{P}_1(\theta,\varphi,\omega)\cong\frac{1}{2}\frac{c}{\omega}\left(\frac{\omega L}{2c}\right)^2\sin\theta\ \hat{\theta}=\frac{1}{2}c\left(\frac{L}{2c}\right)^2\sin\theta\ \omega\ \hat{\theta}, \tag{2.17}$$

and

$$\vec{E}(\vec{r};t)=\frac{c_o}{r}\sin\theta\frac{d^2f(t)}{dt^2}\hat{\theta},\quad c_o=const. \tag{2.18}$$

It is interesting to note that the radiated field by a short dipole is proportional to the second derivative of the input signal with respect to time. For σ=0.01 μsec and smaller, the short dipole approximation is no longer valid, hence (2.15) must be used directly. We have calculated the radiated fields for the above three values of σ using IFFT (inverse fast Fourier transform). The results are plotted in Figure 2.5. It is clearly seen that when σ=0.01 μs, significant ringing occurs in the radiated signal, which may be viewed as much more severe distortions compared to the cases of σ=1.0 μs and σ=0.1 μs.

The final point in discussing the role of antenna is the function of antenna as a receiver. The equivalent circuit of the antenna in receiving mode is shown in Figure 2.6. In this circuit V_{oc} is given by (2.19) in which L_{eff} is defined as the effective length of the antenna.

$$V_{oc} = \frac{1}{I_{in}} \int_V \vec{E}_{rad} . \vec{J}_t dv = \vec{E}_{rad} . \vec{L}_{eff} , \tag{2.19}$$

where

$$L_{eff} = \frac{c}{\omega} \sqrt{\frac{4\pi G R_r}{\eta_o}} . \tag{2.20}$$

In (2.20), G is the gain and R_r. is the radiation resistance of the antenna [Rober95]. It has been shown that [Mal95]

$$V_{oc} \propto \frac{\partial}{\partial t} E_{rad} , \text{ for a short dipole,} \tag{2.21}$$

$$V_{oc} \propto E_{rad} , \quad \text{for a TEM horn.} \tag{2.22}$$

Combining (2.18) and (2.22), it becomes apparent that for a link with two short dipoles as transmit and receive antennas, the received signal is proportional to the third derivative of the signal on the transmit side. That is,

$$V_{oc} \propto \frac{\partial^3}{\partial t^3} f(t), \qquad \text{for a short dipole.} \tag{2.23}$$

And, for a link with two TEM horns as transmit and receive antennas, from (2.14) and (2.22) it is concluded that

$$V_{oc} \propto \frac{\partial}{\partial t} f(t), \qquad \text{for a TEM horn.} \tag{2.24}$$

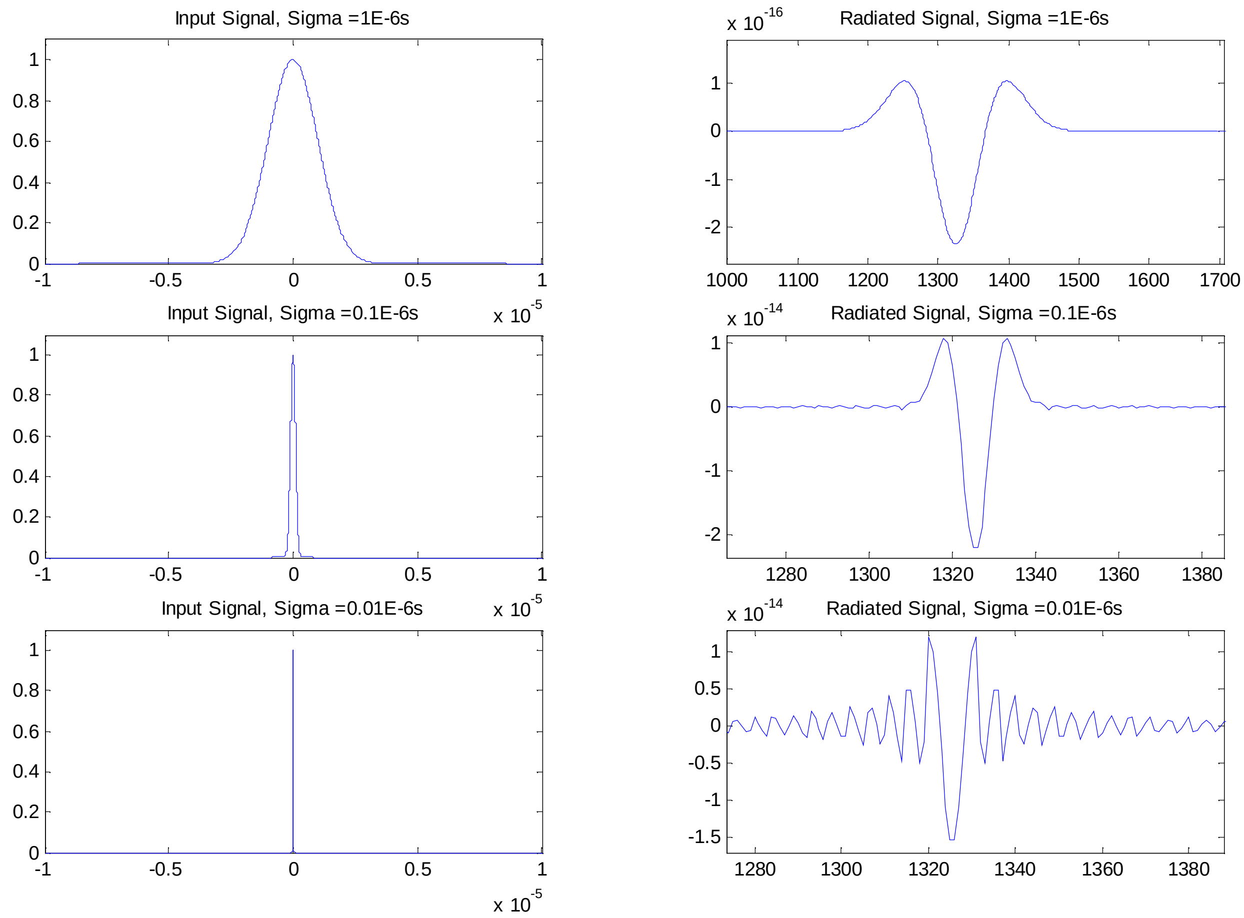

Figure 2.5 Radiated fields of a 1m dipole at $\theta = \pi/2$ with Gaussian pulse excitations of different durations.

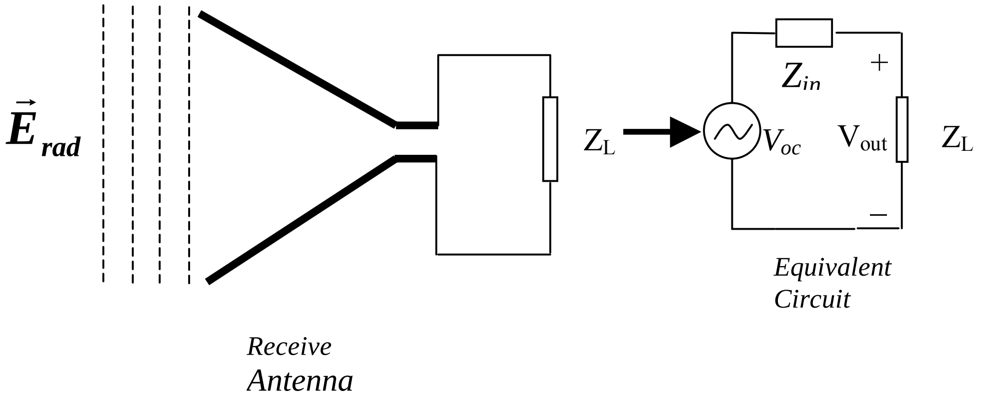

Figure 2.6 Antenna in receiving mode and its equivalent circuit.

2.3. Characterization of UWB Antennas

For radiated measurements involving very short pulses TEM horn antennas have been suggested by [Law78]. TEM horns are quite broadband in both magnitude and phase. Two pairs of these antennas have been fabricated in the Time Domain and RF Measurements Laboratory at Virginia Tech. Both pairs were extensively used for UWB indoor propagation measurements. In this section characterization of these antennas are addressed. In particular, their radiation pattern, gain, and input impedance characteristics are measured. The two pairs of TEM horns have the same basic structure, but one pair provides a larger bandwidth. Each antenna of the set with smaller bandwidth is referred to as antenna A, while each TEM horn with the larger bandwidth is called antenna B. Antenna B has a broader band and TEM can be assumed at sufficiently far distances. It consists of an array of two smaller horns whereas antenna A is comprised of one horn structure. All four horns are equipped with baluns and are fed through coaxial cables.

Antenna radiation patterns were measured in the anechoic chamber facility of Virginia Tech. Pattern measurements were performed in the frequency range of 1.10 GHz to 12 GHz. Below 3.80 GHz spherical measurements covering the entire space were carried out. However, above 3.80 GHz, the anechoic chamber facility was not able to proceed with spherical measurements and hence switched to planar measurements in two dimensions. Figures 2.7 and 2.8 illustrate selected radiation patterns for antenna A covering the frequency range of 1.1 to 12 GHz. Similarly, Figures 2.9 and 2.10 show the radiation patterns for antenna B in the same frequency range. In all these figures the red lines indicate the field patterns in E-plane whereas the blue lines refer to ones in H-plane. In view of Figure 2.7, it is observed that radiation patterns up to 4 GHz indicate less directionality and more side lobes. Between 4 and 8 GHz the antenna demonstrates high directionality and fewer number of side lobes. It can also be observed that E- and H- field patterns become similar between 4 and 8 GHz. For higher frequencies up to 12 GHz, in view of Figure 2.8, the patterns indicate more distinct side lobes. Similar tendencies in patterns are observed for Antenna B as indicated by Figures 2.9 and 2.10. One important difference is that Antenna B exhibits more distinct side lobes even in lower frequencies (Figure 2.9) due to its double horn structure.

The gain and half-power beamwidth of the TEM horns were also obtained from the measurements performed in the anechoic chamber. The results for gain and beamwidth are shown in Figures 2.11 and 2.12, respectively. Finally, input impedance measurements were carried out using a vector network analyzer (VNA) in the Time Domain and RF Measurement Laboratory. The antenna under test was surrounded by absorber slabs on all sides. The (VNA) was operated in its step mode with 128 tracing averages and swept from 1 to 12 GHz. From the measured s-parameter (s_{11}) the normalized input impedance can be computed from

$z_{in} = (s_{11} + 1)/(s_{11} - 1)$. Figure 2.13 depicts the real and imaginary parts of the input impedance versus frequency. The curves in Figure 2.13 are average fits to the measured data. It is observed that the fit for input impedance is very close to (50+j0) ohms, which is desirable for both antennas.

In view of the pattern plots, gain and HPBW graphs, and input impedance measurements, both TEM horns do provide close to constant input impedance with high directivity (especially higher frequencies) and relatively well-behaved gain over 11 GHz bandwidth. As discussed in the last section, these properties of TEM horns along with the time- and frequency- domain propagation measurements do indicate that the antennas are indeed ultra-wideband.

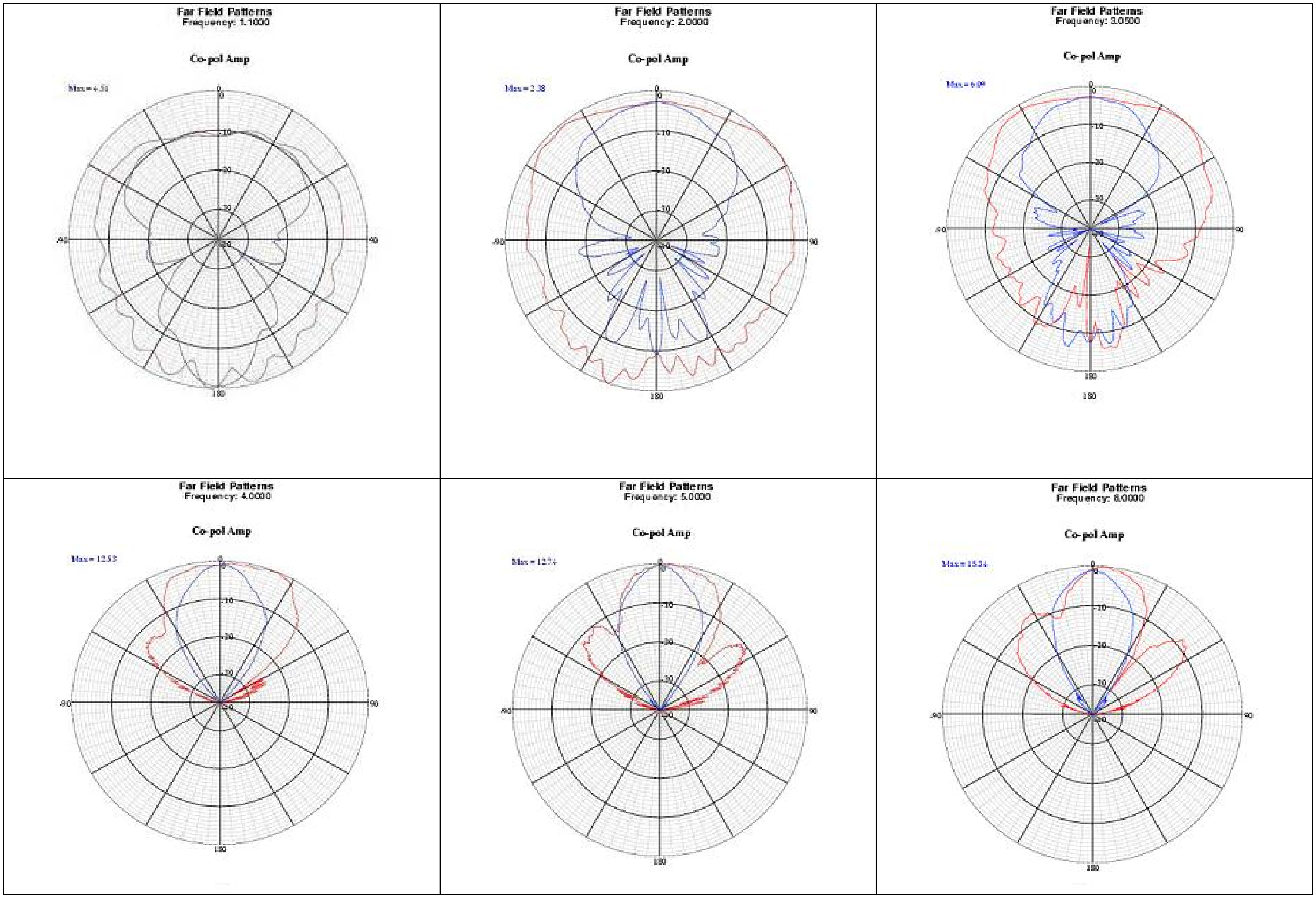

Figure 2.7 E- and H-plane radiation patterns for antenna A in the frequency range of 1.1 to 8 GHz.

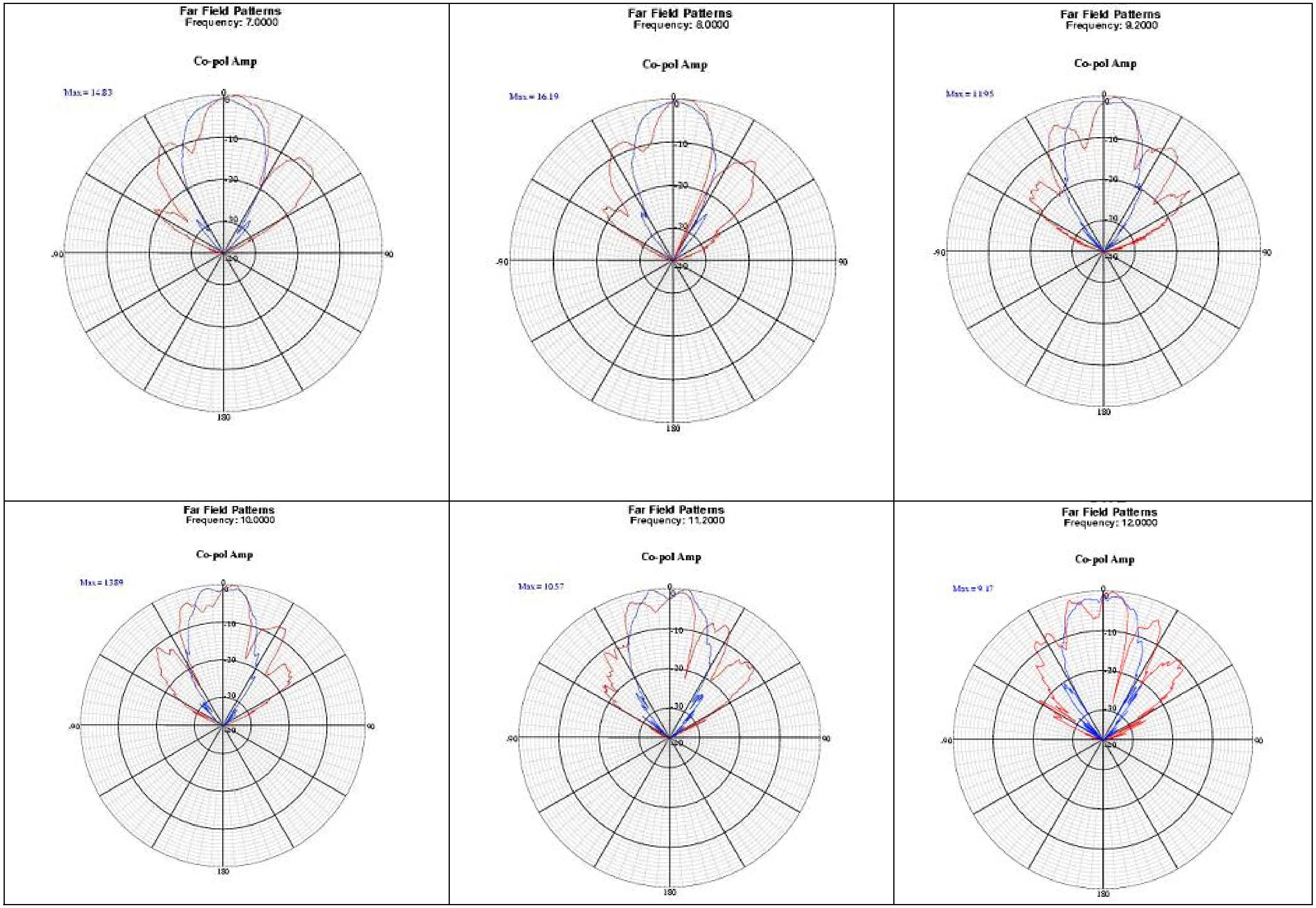

Figure 2.8 E- and H-plane radiation patterns for antenna A in the frequency range of 8 to 12 GHz.

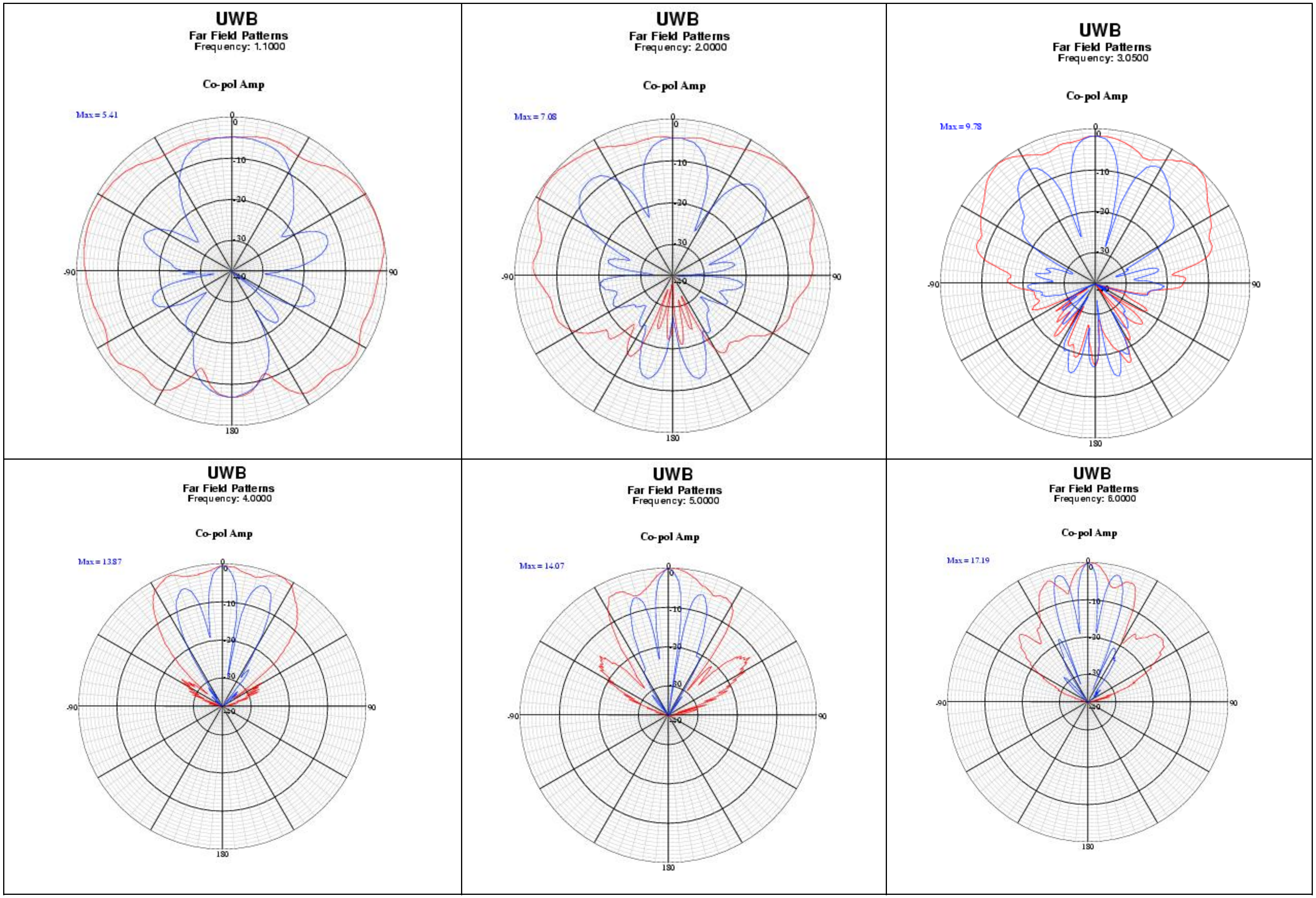

Figure 2.9 E- and H-plane radiation patterns for antenna B in the frequency range of 1.1 to 8 GHz.

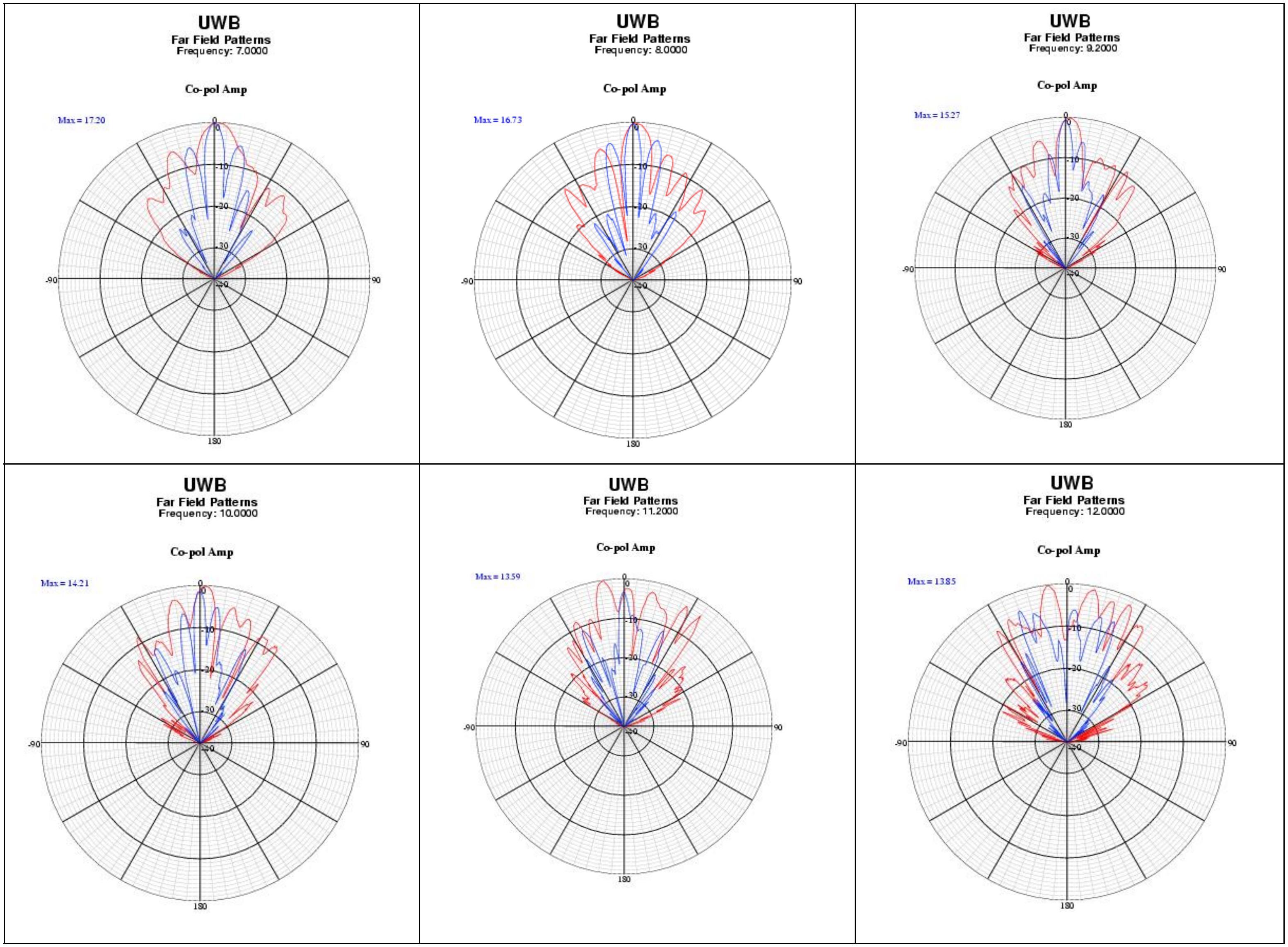

Figure 2.10 E- and H-plane radiation patterns for antenna B in the frequency range of 8 to 12 GHz.

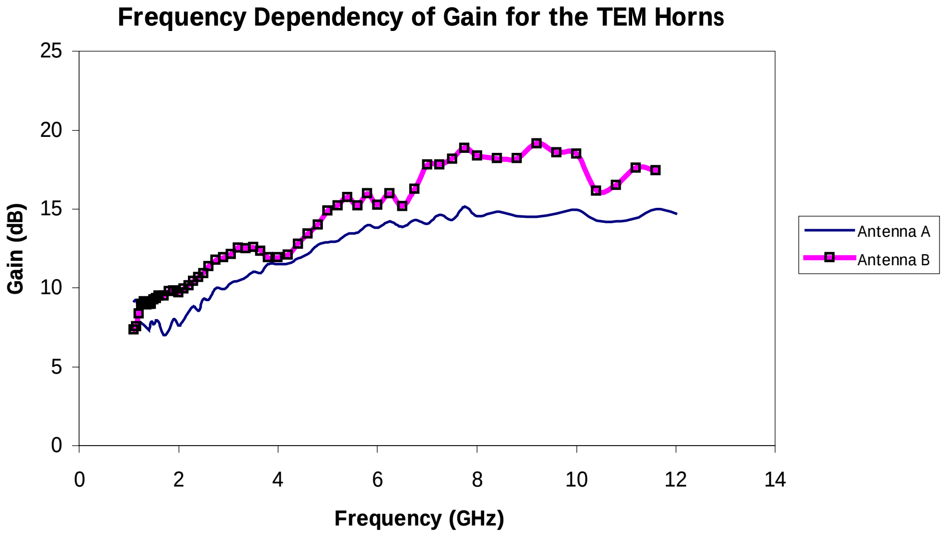

Figure 2.11 Gain versus frequency for TEM horns A and B.

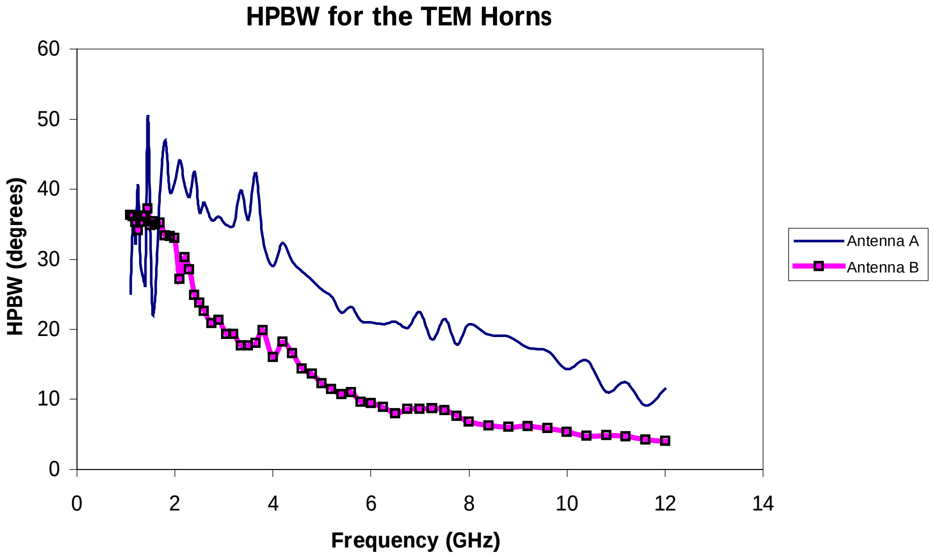

Figure 2.12 Half-power beamwidth (HPBW) versus frequency for TEM horns A and B.

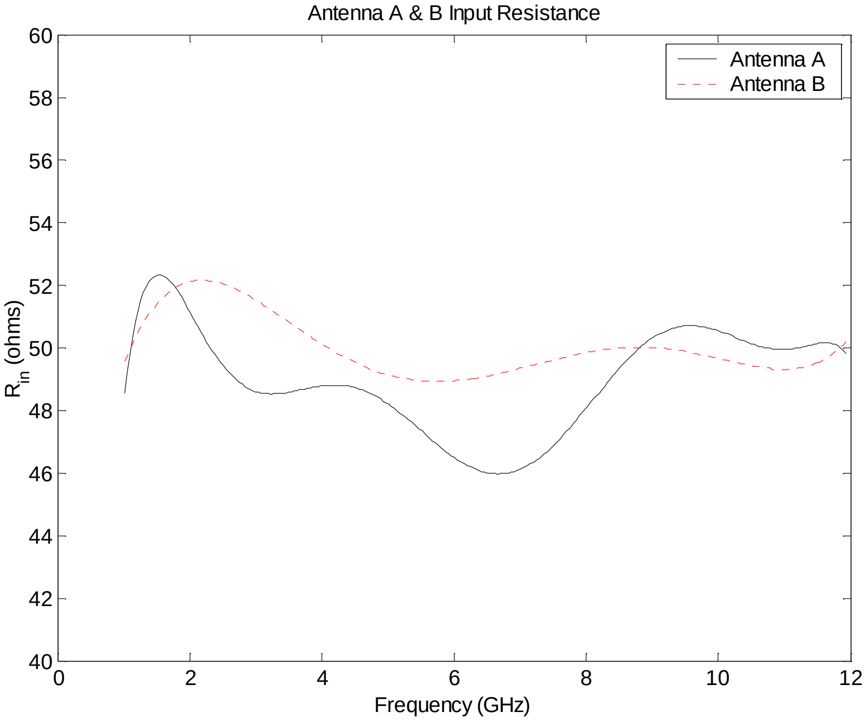

(a)

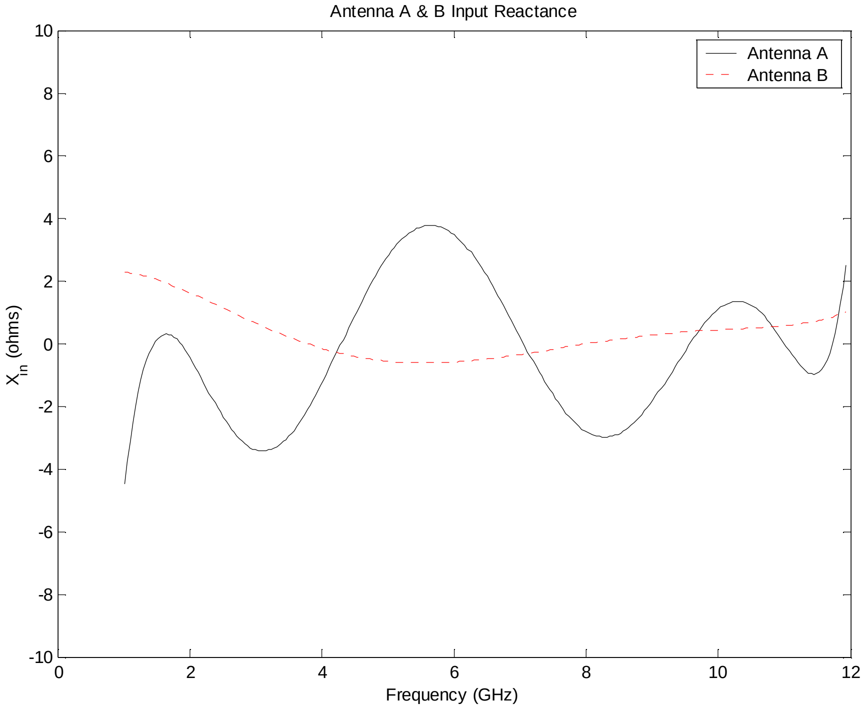

(b)

Figure 2.13 Measured input impedances for antennas A & B: (a) resistance (b) reactance

CHAPTER 3

Measurement Techniques

The problem of UWB channel characterization has been treated experimentally by different approaches in recent years. These approaches can be classified into two main categories - direct time-domain measurement technique using short pulse generators and digital sampling oscilloscope and frequency-domain measurements using vector network analyzers. The channel impulse response in indoor environments can be obtained from the time-domain measurement data and the use of deconvolution [Win97], [Win02], [Muq03]. It can also be obtained from frequency-domain measurement results and the use of inverse Fourier transformation [Str01], [Kei02], [Mac02], [Gha02], [Dona96]. In this chapter, we first present a brief literature review of the two measurement techniques and point out their advantages and disadvantages. Then, we discuss the basic theory of phase retrieval from the magnitude data and illustrate the technique analytically through simple examples simulating multiple reflections.

3.1. Frequency Domain vs. Time Domain: Pros and Cons

Although, the direct time-domain approach is more intuitive and provides a clearer and better understanding of the UWB propagation characteristics, it requires more sophisticated equipments to perform the measurements, such as ultra-short pulse generators and digital sampling oscilloscopes. In addition, the sensitivity of sampling scopes is generally less than the sensitivity of frequency-domain network analyzers. The main aim of this chapter is to introduce a simple low-cost frequency-domain approach that can be used for UWB channel characterization with a comparable accuracy to direct time-domain measurements. Win *et al.* have used 1024 sampling points to capture a 50ns time window [Win97], [Win02]. However, they have mentioned neither the bandwidth of the pulses nor those of the antennas used in their measurements. Muqaibel *et al.* have used 5120 sampling points to sample the same time window, and used TEM horn antennas of bandwidths up to 12GHz and pulses with FWHM (full-width half-maximum) less than 100 ps [Muq03].

Keignart and Daniele [Kei02], and Ghassemzadeh *et al.* [Gha02] used experimental setups based on the VNA to characterize UWB channels. Their measurements are based on measuring the complex scattering parameter s_{21} between the transmitting and receiving antennas. They used low-loss coaxial cables to bring the signals to the vector network analyzer. These cables are a major limiting factor in frequency-domain measurements, because the cable attenuation increases with both the length as well as the frequency of operation. In these two measurement efforts, an upper frequency of 6GHz is not exceeded. Keignart and Daniele [Kei02] have presented their results for a bandwidth covering the frequency range 2 to 6GHz, while Ghassemzadeh *et al.* [Gha02] presented their results for a bandwidth from 4.375 to 5.625GHz.

Street *et al.* [Str01] and Macedo *et al.* [Mac02] improved the aforementioned frequency-domain experimental setup by using a multimode optical fiber in lieu of long coaxial cables. Optical fibers are characterized by extremely low-loss and excellent interference immunity compared with coaxial cables. Thus, optical fiber systems can be used to characterize UWB channels involving distances much longer than those that can be measured by coaxial cables. However, the operating bandwidth becomes a significant limiting factor. Wideband optical fiber systems can substantially increase the cost of measurement equipment. Street *et al.* [Str01] have presented their results for a bandwidth from 2.4 to 2.48GHz, while Macedo *et al.* [Mac02] performed their measurements in the frequency range 1.7 to 1.9GHz. These bandwidths are relatively narrow when compared to the UWB bandwidth which spans the frequency range of 3.1 to 10.6GHz.

By comparing the time- and frequency-domain measurement techniques which have been used for UWB channel characterization, it can be noted that there is a great difference in the distances that can be reliably measured due to the attenuation of connecting RF cables; hence the motivation to introduce a new approach for UWB frequency-domain measurements which requires neither long RF cables nor cost prohibitive optical fiber systems.

Donaldson *et al.* [Dona96] studied the propagation of UHF in indoor environments. They used an experimental setup based on the VNA quite similar to that used by Keignart and Daniele [Kei02]. However, they used only the magnitude values of the measured s_{21} and obtained the phase information from the magnitude data using a Hilbert transform relationship based on the causality and analyticity of the received signal. Tesche [Tes92] had discussed this technique earlier, while Páez *et al.* [Paez02] have proposed an analogous approach using a spectrum analyzer instead of the VNA, but did not describe the details of their measurement setup. They have used their measurement data to calculate the main parameters of propagation channels, such as *rms* time-delay and the information carrying capacity. This technique is widely used in circuit analysis, digital signal processing, image reconstruction, and remote sensing [Hay80], [Opp99].

In this work we introduce an experiment setup based upon the same idea of phase reconstruction detailed by Donaldson *et al.* [Dona96], but with the use of a scalar network analyzer (SNA) instead of the VNA. A synthesizer sweeper is directly connected to the transmitting antenna and the detector of the SNA is connected to the receiving antenna. The only connecting cable between the transmitting and the receiving sides is the sweep in/out cable to synchronize the sweeping of the SNA and the synthesizer sweeper. The sweep signal is a saw-tooth signal of a frequency that is nearly equal to 1 Hz and has a peak amplitude of about 10 V. Thus, essentially any cable can be used for this purpose.

3.2. Theory of Phase Retrieval in Frequency-Domain Measurements

The purpose of the UWB channel characterization is to obtain the impulse transfer function of the channel, which can be represented either in frequency-domain or in time-domain The relationship between the two domain responses is governed by the Fourier and inverse the Fourier transformations. The calculation of the impulse response requires both the magnitude and phase of the frequency-domain channel transfer function. For narrowband channel characterization, phase data are less important because the channel is characterized around specific carrier frequencies. This is not the case for UWB channels where phase is a critical parameter and the nature of its variations with frequency can significantly impact the time-domain response. Unless the phase varies linearly with frequency over the bandwidth of the signal, distortions in the signal will occur. However, accurate phase measurements in environments involving long distances may not be easily achieved. On the other hand, amplitude measurements are much simpler than phase measurements for the same case. This is the main motivation in introducing a technique for obtaining the phase information from the amplitude data.

The signal at the receiving end satisfies the causality and analyticity conditions. That is, it cannot be detected before the propagation time between the transmitter and the receiver has elapsed. Moreover, for finite energy pulses, the pulse amplitude must approach zero as time goes to infinity. The spectrum of a causal analytic signal is characterized by a Hilbert transform relationship between its real and imaginary parts as follows,

$$R(\omega) = X(\omega) + jY(\omega) = X(\omega) + j\mathrm{H}[X(\omega)], \tag{3.1a}$$

where

$$H[X(\omega)] = \frac{1}{\pi}\int_{-\infty}^{\infty} \frac{X(\overline{\omega})}{\omega - \overline{\omega}} d\overline{\omega} \tag{3.1b}$$

It is emphasized that the causality of $r(t) = \Im^{-1}[R(\omega)]$ implies that $r(t)=0$ for t<0. The causality condition is also referred to as minimal phase condition. In the frequency-domain, this condition is equivalent to all poles and zeros of R(s) lying on the left half of the s-plane, or the poles and zeros of the z-transform of r(t) lying within the unit circle. Thus, for a causal analytic signal the real part of its spectrum is sufficient to reconstruct the total signal. However, the known part of measured data for S_{21} is not the real part but the amplitude of the spectrum. The logarithm of the spectrum can be used to separate the amplitude and phase as follows

$$\widehat{R}(\omega) = \ln(R(\omega)) = \ln(|R(\omega)|) + j\Phi(\omega) . \tag{3.2}$$

The function $\widehat{R}(\omega)$ represents the spectrum of another function, which can satisfy causality and analyticity only if all the poles and the zeros of $R(\omega)$ lie inside the unit circle in the complex *z*-plane [Dona96], [Paez02]. In this case, (3.1) can be applied directly to (3.2), resulting in the following relationship between the amplitude and phase of $R(\omega)$,

$$\Phi(\omega) = \mathrm{H}(\ln(|R(\omega)|)) . \tag{3.3}$$

Thus, the complex spectrum can be represented in terms of its amplitude as stated below,

$$R(\omega) = |R(\omega)| \exp\left[j\mathrm{H}\left(\ln(|R(\omega)|)\right)\right] . \tag{3.4}$$

It should be noted that the phase obtained from (3.3) represents the minimum phase of $R(\omega)$. If not all poles and zeros of $R(\omega)$ lie inside the unit circle in the complex *z*-plane, a non-minimum phase part should be added to the minimum phase obtained by (3.3). This non-minimum phase part corresponds to the phase of an all-pass filter multiplied by the minimum phase spectrum as follows,

$$R(\omega) = |R(\omega)| \exp\left[j\mathrm{H}\left(\ln(|R(\omega)|)\right)\right] G_{all}(\omega) , \tag{3.5}$$

where $|G_{all}(\omega)| = 1$. It can be noted that the phase of this all-pass filter cannot be predicted by the Hilbert transform because the logarithm of its amplitude is zero. The evaluation of this non-minimum phase portion is the most complicated part of the phase retrieval procedure from the amplitude of spectrum; it may require a long iterative and optimization process [Ko02], [Yag99], [Sar98]. As far as the problem of UWB channel characterization is concerned, obtaining the non-minimum phase is even more complicated because of the ultra wide spectrum and the large number of data points. However, Páez *et al.* [Paez02] has mentioned that the minimum phase part gives results that do not differ drastically from the exact value, such that it can be of practical use in the estimation of the real value. Thus, (3.4) is used as the basis of measurement procedure in this work. Finally, the time-domain response can be obtained by the inverse Fourier transform of (3.4). That is

$$r(t) = \mathrm{IFFT}\left(|R(\omega)| \exp\left[j\mathrm{H}\left(\ln(|R(\omega)|)\right)\right]\right) . \tag{3.6}$$

3.3. Illustration of Phase Retrieval Technique

Before embarking on frequency-domain measurement of indoor channels, based on the signal amplitude as discussed above, it is most helpful to discuss the validity of this approach through a simple example. In this example a train of bipolar Gaussian pulses are used to simulate multiply reflected pulses incident on a receiving antenna. These bipolar pulses may be viewed as monopolar Gaussian pulses radiated by a UWB antenna. A bipolar Gaussian pulse is described by

$$g(t,t_0,\tau)=[-2(t-t_0)/\tau^2]\exp(-(t-t_0)^2/\tau^2), \tag{3.7}$$

where t_0 and τ define the center and temporal width of the pulse, respectively. A train of these pulses, simulating multiple reflections in an indoor scenario, is assumed to be as follows;

$$f(t)=g(t,5,0.05)-0.75g(t,6.5,0.05)+0.5g(t,7.5,0.05). \tag{3.8}$$

Figure 3.1 shows this pulse train in the time-domain. Fourier transforming $f(t)$, the magnitude and phase of the pulse train in the frequency-domain are obtained. Figure 3.2 illustrates the normalized magnitude and the unwrapped phase of the spectrum.

In practical measurements, the amplitude cannot be reliably determined below a certain minimum value defined mainly by the dynamic range and the sensitivity of the measurement setup. This limitation determines the upper frequency limit of the frequency-domain measurements. However, the corresponding incremental time step in the time domain is inversely proportional to the maximum frequency of the measured spectrum. Thus, for better comparison with time-domain measurements, it is required to increase the measured spectrum using zero padding. Thus, the question that arises is about the validity of zero padding in obtaining the time-domain response from the frequency-domain response. Figure 3.3 further shows the spectrum of the original pulse where its amplitude is forced to –70dB when its original amplitude is less than -40dB. Figure 3.4 compares the original pulse and the pulse obtained by the inverse Fourier transform of the zero-padded spectrum. It is noted from this plot that the effect of zero padding is negligible such that it can be used to extend the spectrum of the measured spectrum without a significant effect on the corresponding time-domain response.

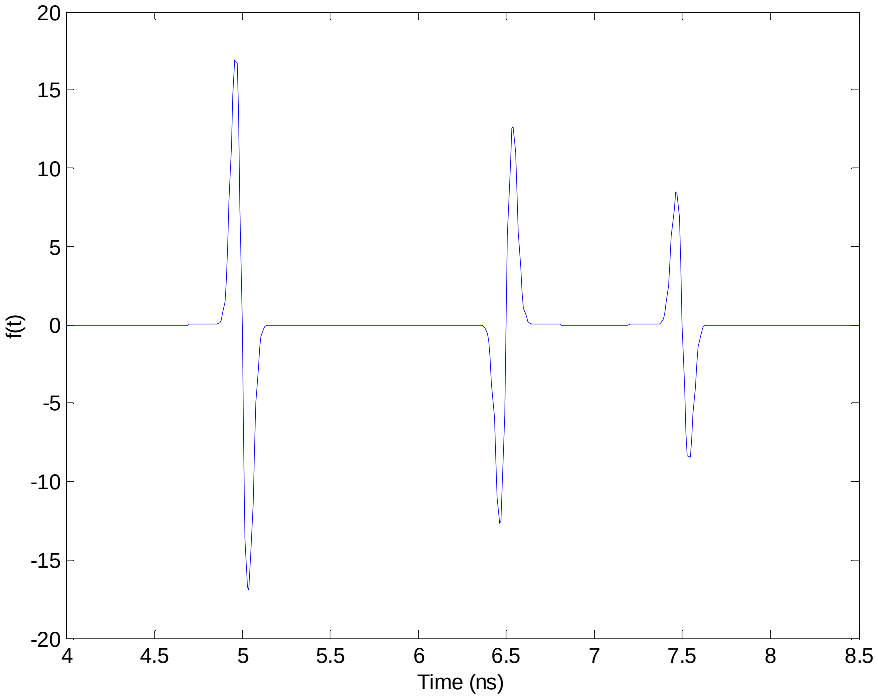

Figure 3.1 A train of first derivative Gaussian pulses simulating ensemble of multiple reflected signals.

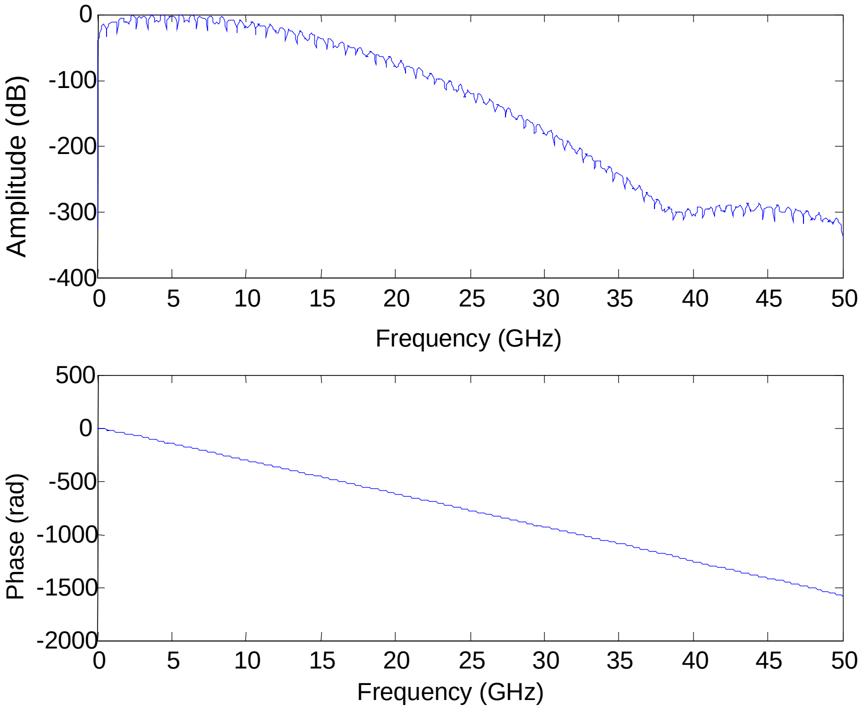

Figure 3.2 The normalized magnitude in dB and phase in radians for the pulse train.

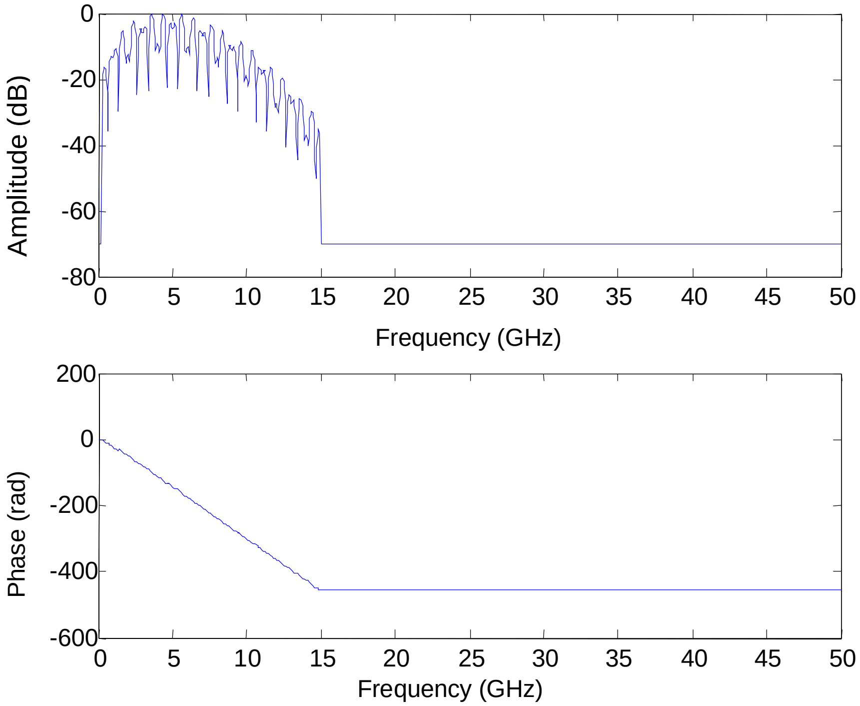

Figure 3.3 The normalized amplitude in dB and phase in radians for the zero-padded spectrum of the pulse train. The zero padding is performed from 0 to 0.2 GHz and from 15 to 50 GHz.

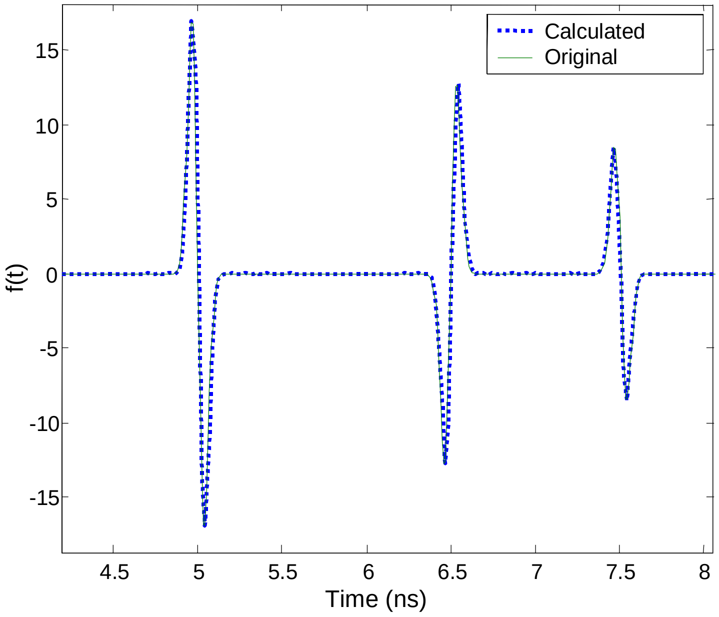

Figure 3.4 Comparison between the original pulse and the calculated pulse after zero padding.

In the next step, the amplitude of the zero-padded spectrum, shown in the first plot of Figure 3.3, is used to obtain the corresponding phase distribution. Figure 3.5 shows the difference between the exact phase and the phase obtained from the magnitude using (3.3). Adding this phase difference to the phase given in Figure 3.3 gives the phase calculated from the magnitude spectrum. It should be noted that the phase difference in Figure 3.5 is small compared with the phase of the signal obtained using the Fourier transform. However, this minimum phase part has a significant effect on the shape of the resultant time-domain signal. Figure 3.6 compares the reconstructed time-domain signal obtained by the inverse Fourier transform of the zero-padded spectrum with the original pulse train. It is observed that the reconstructed pulse train agrees well with the original pulse train, reaffirming the validity of phase retrieval technique. In summary, it is concluded that the use of SNA in conjunction with the phase retrieval technique based on Hilbert transform is a reasonable alternative to time-domain and VNA measurement techniques.

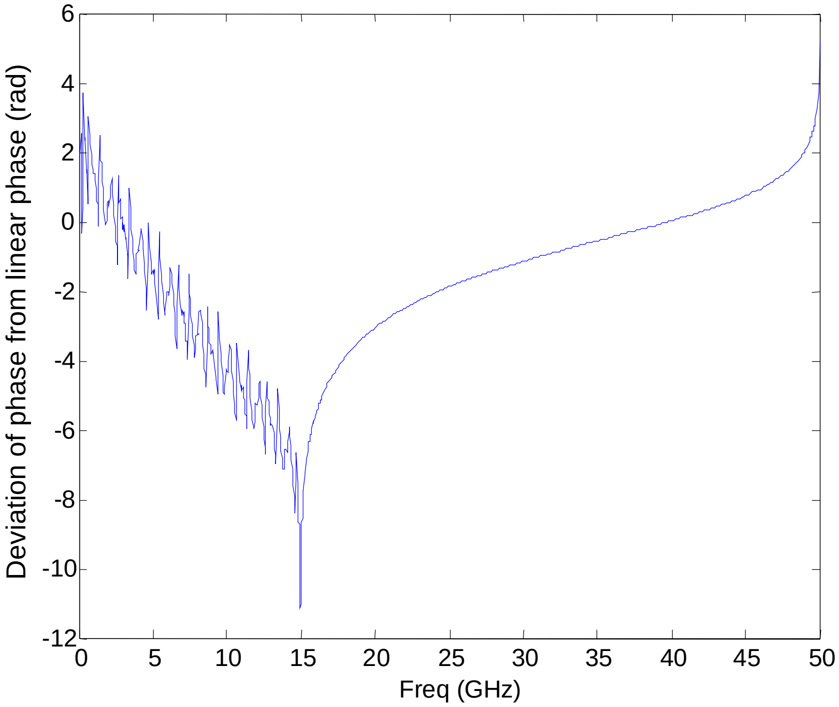

Figure 3.5 Difference between the exact phase and the phase calculated from the Hilbert transform of the zero padded spectrum.

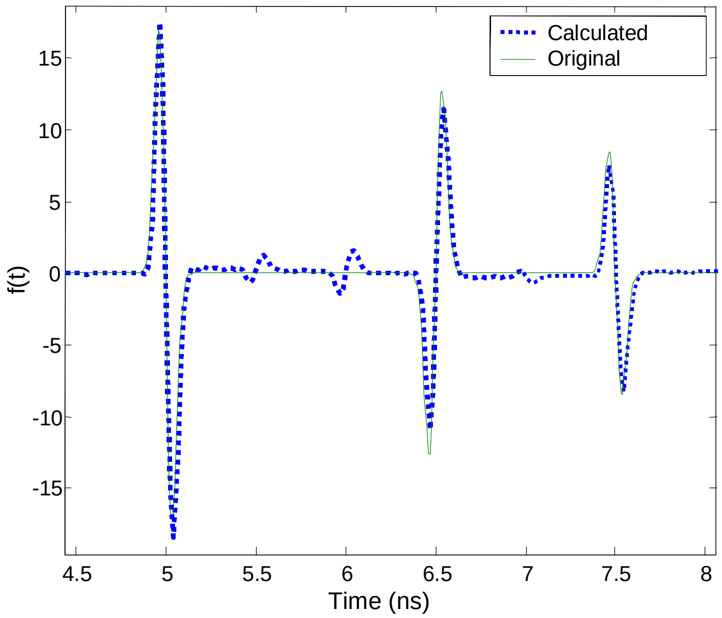

Figure 3.6 Comparison between the original pulse train and the reconstructed pulse train calculated from zero-padded magnitude spectrum.

CHAPTER 4

UWB Indoor Channel Measurements

In this chapter, we present frequency-domain characterization for UWB propagation in indoor environments. Then, the frequency-domain channel characterization results are compared with the counterpart time-domain measurements for the same propagation environments reported before [Muq03a]. This comparison of two different measurement approaches validates the accuracy of the measured channel characteristics. The measurements are performed in the frequency domain using a scalar network analyzer. Only the amplitude of the link transfer function is measured. However, to obtain the time-domain impulse response of the link, the phase distribution is also required to be included in the inverse Fourier transform. Direct phase measurements can be made with a vector network analyzer, but this would work for relatively short distances. For longer distances, the attenuation of long coaxial cables, which are needed in the VNA-based measurements, makes reliable measurements very difficult. The phase of the link transfer function is determined from a Hilbert transform relationship as discussed in Chapter 3.

In section 4.1, the measurement set up is discussed in detail. All measurements are performed at the same locations where time-domain measurements had been made previously. This will facilitate the comparison of time-domain and frequency-domain measurement results. In section 4.2, a signal-processing algorithm, developed for the comparison of direct time-domain measurements and the time-domain responses obtained from the frequency-domain data, is discussed. In section 4.3, impulse responses based on time-domain and scalar frequency-domain measurements are compared. Section 4.4 presents the channel characterization results for two building on Virginia Tech campus. Small- and large-scale analyses are carried out using the data collected.

4.1. Measurement Setups for Frequency-Domain Measurements

Figure 4.1 shows the experiment setup that is used for the frequency-domain channel measurements with the scalar network analyzer (SNA). A signal generator producing a square-wave pulse of amplitude 5 $V_{p\text{-}p}$ and a frequency of 27.8 kHz is used to modulate the output amplitude of the RF sweep synthesizer. On the other hand, the SNA is adjusted to detect the modulated RF signal. This modulation improves the signal-to-noise ratio of the signal detected by the SNA. The synchronization between the source and the SNA is achieved by connecting the sweep-out of the RF synthesizer to the sweep-in of the SNA. The received signal is amplified using two 10 dB UWB amplifiers before it is detected using a wideband RF detector.

The output of the sweep synthesizer is expected to be constant for all frequencies. However, such flat power level may not be achieved due to different practical aspects such as the frequency dependence of the connectors, the connecting cables, and the internal electronics of the synthesizer itself. Thus, the output of the source should be calibrated to subtract the effect of the source from channel measurements. Figure 4.2 shows a schematic diagram for the source calibration setup. The output of this measurement setup is stored in dB as a source calibration file. The frequency-domain channel transfer function is obtained by subtracting the pre-stored source calibration file from the spectral output (measured in dB) of the setup shown in Figure 4.1.

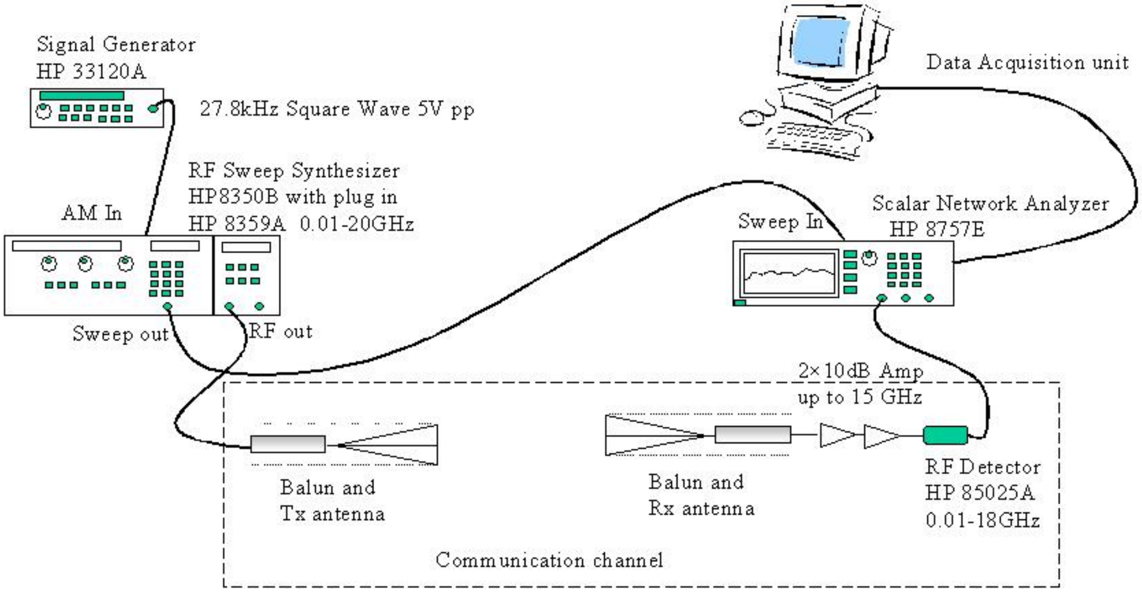

Figure 4.1 The measurement setup for frequency domain UWB channel characterization using scalar network analyzer (SNA)

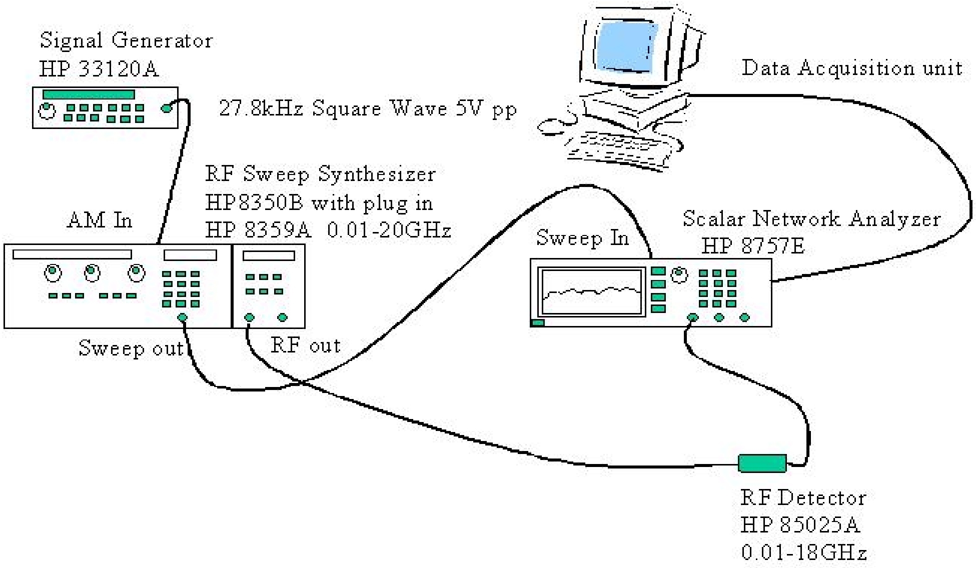

Figure 4.2 Source calibration setup.

4.2. Signal Processing of Frequency Domain Measurements

Frequency-domain measurements for line-of-sight (LOS) scenarios are recorded by the SNA in a frequency band of 100 MHz to 12 GHz; however, data acquisition is limited to 401 points, dictated by the SNA capability. Therefore, sampling at approximately 30 MHz increments is achieved. For non-line-of-sight (NLOS) scenarios, due to smaller signal-to-noise ratios, data are collected in two frequency bands of roughly 6 GHz each, with a total of 802 points. Because we intend to compare the frequency-domain results with their time-domain counterparts presented in [Muq03], the data sizes from both techniques need to be identical. The output of the SNA consists of 401 frequency points representing a spectrum from 100 MHz to 12 GHz. The incremental time step of the corresponding time-domain response is inversely proportional to the maximum frequency of the measured spectrum. That is why zero padding is required to increase the maximum frequency of the measured spectrum using the SNA. To simplify fast Fourier transform (FFT) and inverse fast Fourier transform (IFFT) computations, the data are arranged at 1024 points for all procedures. Thus, the maximum frequency is nearly 30.6 GHz, which corresponds to an incremental time step of 32.6ps in the time domain. The Hilbert transformation technique is used for the phase retrieval from the amplitude data obtained by the SNA.

The time-domain response of the pulsed source used for the time-domain measurements is defined at a 5ns window, using 1k sampling points with an incremental step of 5ps. The corresponding time-domain channel measurements are defined at a 100ns profile using 10k sampling points with an incremental step of 10ps. The spectrum of the pulsed source and time-domain channel measurements can be obtained using FFT. However, due to different sizes of the time windows and the incremental time steps introduced by different methods, the calculated spectra have different bandwidths and incremental frequency steps. To facilitate the comparison with the frequency-domain measurements, all the spectral points are interpolated such that we have the same frequency band from 0 to 30.6 GHz and the same number of sampling points of 1024. The corresponding response in time domain is presented in a 16.3 ns window with an incremental step of 32.6ps. Such time-window is found to be enough to cover the significant part of the multiple reflections for the channel propagation.

4.3. Comparison of Time-Domain and Frequency-Domain Impulse Responses

The IFFT of the frequency-domain data provides the impulse response (IR) of the channel. It is emphasized that in this investigation the channel includes the propagation medium as well as the transmit and receive antennas. To obtain the corresponding IR using the time-domain data, the FFT of the channel measurement is divided by the FFT of the source. This result can be compared directly in the frequency domain with the frequency-domain channel measurements. Or, it can be converted to time domain via IFFT and be compared with the impulse response obtained from frequency-domain measurements. Alternatively, one can obtain the time-domain response by multiplying the frequency-domain measurement data with the spectrum of the pulsed source and converting the result back to time domain via IFFT. This result can then be compared with the corresponding direct time-domain channel measurements.

Figure 4.3 shows the flowchart for the aforementioned procedures used for comparison of frequency-domain and the time-domain channel measurements. Figure 4.4 compares the amplitude of the frequency-domain channel response measured with the SNA with the corresponding response obtained from the time-domain measurements. Figure 4.5 depicts the phase retrieved by using the Hilbert transform. This phase corresponds to a time-domain signal starting at zero on the time axis. Thus, an additional linear phase can be added to this phase to introduce the appropriate time shift in the corresponding time-domain response to be compared with the time-domain measurement. Figure 4.6 compares the time-domain response obtained from the SNA measurements and the directly measured time-domain response. As noted, there is a good agreement between the responses obtained from the frequency-domain measurements (in conjunction with the phase retrieval via Hilbert transform) and the direct time-domain measurements.

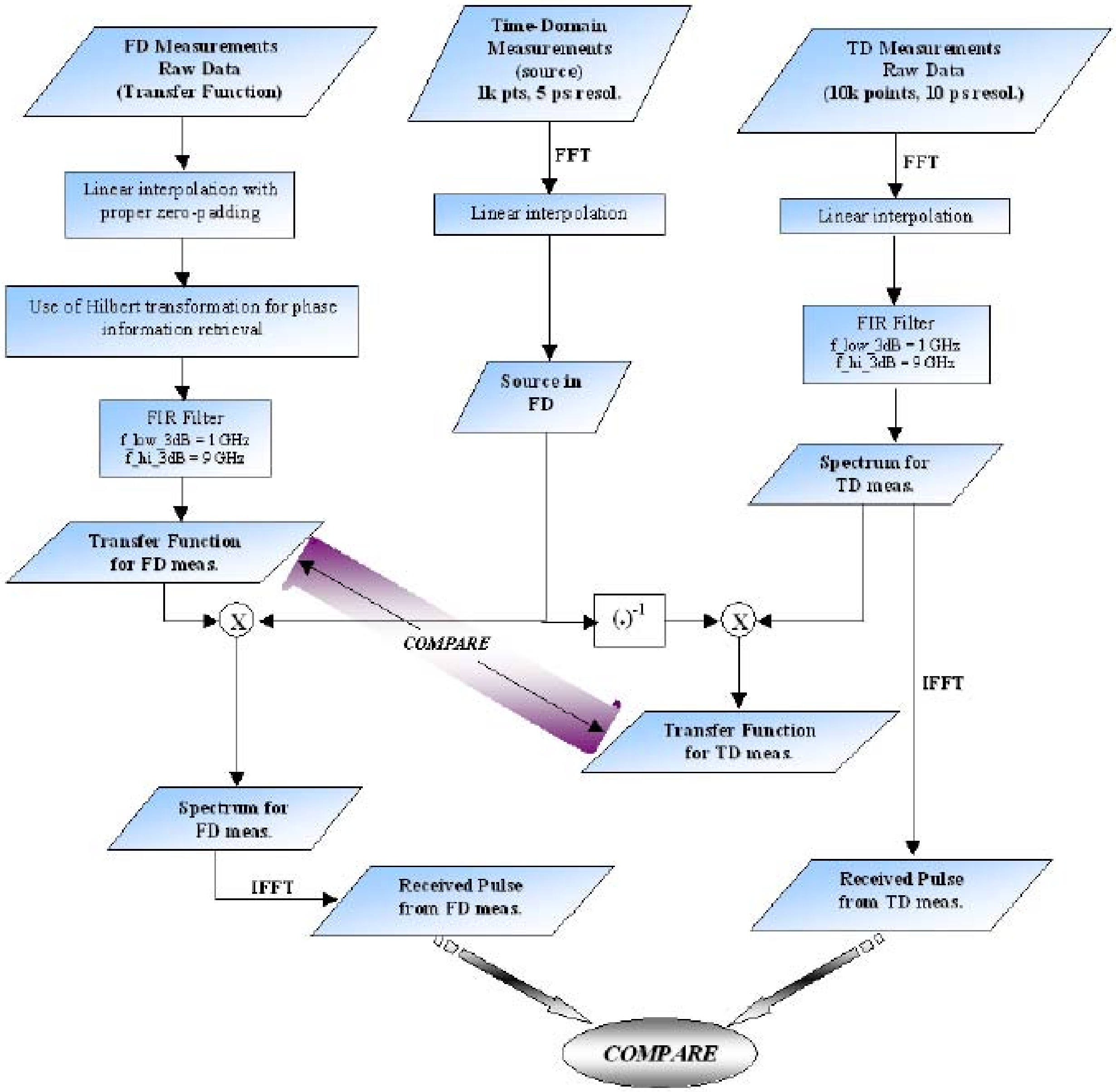

Figure 4.3 Flowchart demonstrating the main steps of the signal processing for comparing time-domain and frequency-domain measurements of UWB channel characterization.

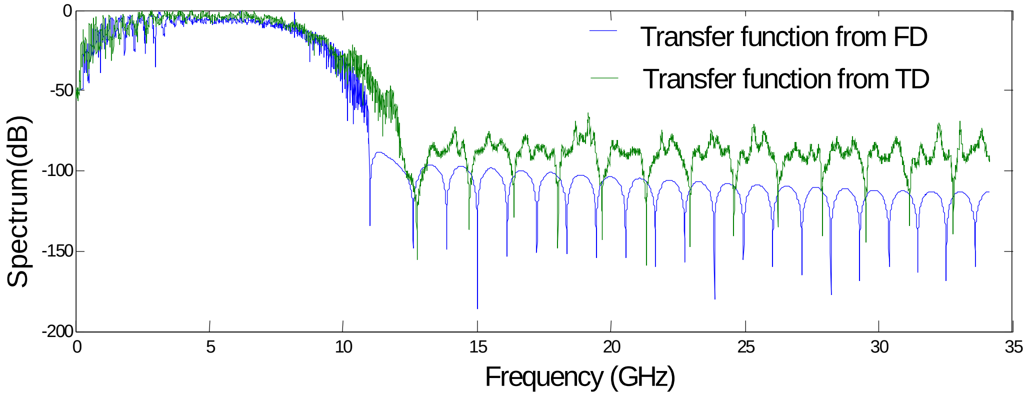

Figure 4.4 Comparison between channel transfer functions obtained from frequency-domain (SNA) and time-domain measurements.

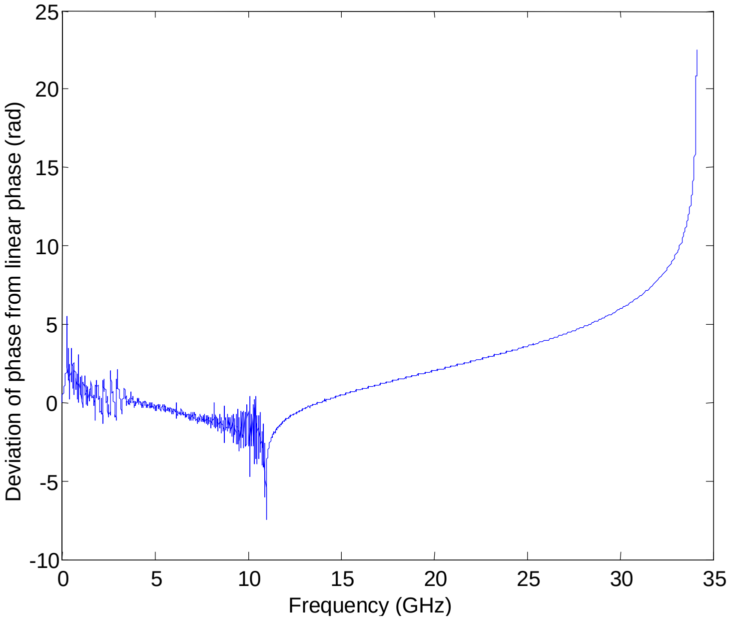

Figure 4.5 The phase retrieved from measured amplitude data and the use the Hilbert transform.

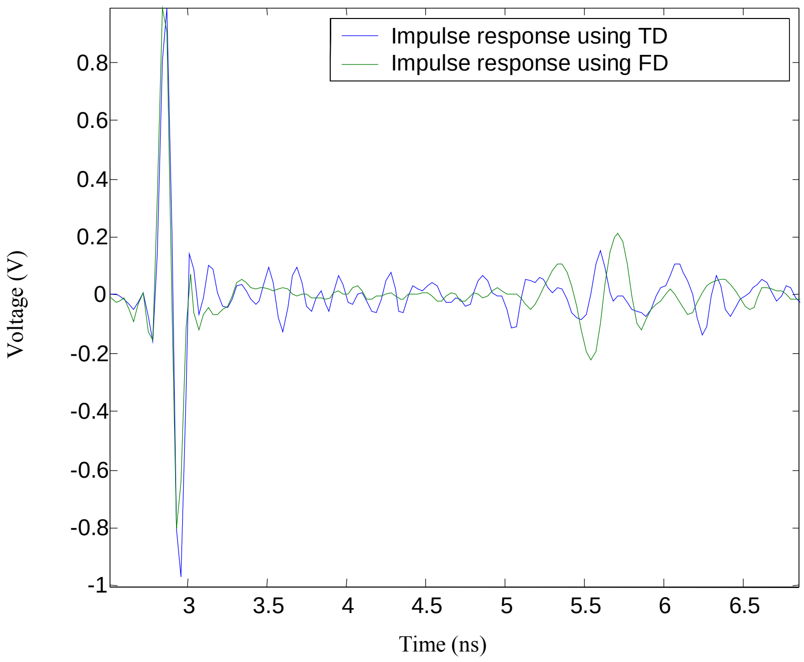

Figure 4.6 Comparison of impulse responses obtained from time-domain (TD) and frequency-domain (FD) measurements.

4.4. Data Analysis and Experimental Results for Indoor Environment

We performed two sets of measurements using TEM horn antennas and biconical antennas. The receive and transmit antennas were placed on plastic moving carts at a height of about 1.25 m above the floor. The TEM horn antennas were aligned for maximum boresight reception. The TEM horn antenna has a narrow beamwidth and thus is highly directional. With TEM horns fewer multipath components are detected, and essentially none from behind the receiver. On the other hand, biconical antennas are omni-directional and hence may prove more useful for mobile applications. The biconical antennas used in this investigation are not designed as impulse antennas; however, they are impedance-matched over a very wide bandwidth. To avoid the impact of human movements on the measured data, measurements were conducted during low activity periods.

The measurements were carried out with the aim of doing both small-scale and the large-scale channel characterization. A 7×7 grid with 15cm spacing between adjacent points was designed and used for the examination of small-scale fading. However, repeated measurements indicated that there is no significant small-scale fading due to phase cancellation over the grid area. Thus, it was determined that reducing the number of grid points over the same area is reasonable. Similar conclusion was also obtained for the time-domain work [Muq03a].

Accordingly, the small-scale measurement points were reduced from 49 to 9 points by using a 3×3 grid, with 45 cm between the adjacent points.

We chose two buildings (Whittemore Hall and Durham Hall) on Virginia Tech campus as our measurement locations. Whittemore Hall is comprised mainly of offices and classrooms. In general, its walls are made of drywalls with metallic studs, while some are made of cinderblock and poured concrete. In Durham Hall, the walls are mostly made of not only drywalls but also cinderblocks. It should be noted that floors are covered with tiles in hallways and laboratories. Both halls have carpet inside the offices and conference rooms.

In Whittemore Hall, the measurements were performed in three floors, specifically in a hallway on the second floor, in a narrow corridor on the fourth floor, and in a conference room on the sixth floor. In Appendix A, Figures A.1 and A.2 show the blueprints and the photographs of the measurement locations. In Durham Hall, all measurements were carried on the fourth floor. Five different transmitter locations were considered. For every location, measurements at different receiver locations were performed, as indicated on the blueprints in Figure A.3a.

Various scenarios were considered in the measurement campaign, including LOS and NLOS in hallways, within a room and room-to-room. Table 4.1 summarizes the LOS measurement specifications. The first column lists the abbreviations for measurement locations. The first capital letter refers to the main location of measurement; for example, 'W' for Whittemore Hall, and 'D' for Durham Hall. The single digit following the first letter indicates the recorded transmitter position number, while the ending capital letter identifies the specific receiver location. The table also includes number of profiles, i.e. small-scale measurements, taken for both sets of antennas along with the corresponding mean antenna separation for each scenario.

Non-line-of-sight measurements were carried out only in Whittemore Hall in four different floors as indicated in the Appendix B. In each of the four figures given in the Appendix B, an approximate distance is given for a rough estimate of the antenna separation for the NLOS measurements. As in the figures presented in Appendix A, the transmitter and receiver locations are marked with black squares and circles, respectively. Seven different transmitter locations were considered along with several receiver locations for each transmitter locations.

Table 4.1 Specifications of LOS measurement scenarios

Abbreviation	Location	Description	# profiles (TEM)	# profiles (Biconical)	$\overline{d}$ (m)
W2.A	Hallway in 2nd floor	Hallway	9	9	9.3
W2.B	Hallway in 2nd floor	Hallway	9	9	17.6
W2.E	Hallway in 2nd floor	Hallway	9	9	15.4
W2.F	Hallway in 2nd floor	Hallway	9	9	30.9
W2.G	Hallway in 2nd floor	Hallway	9	9	49.1
W4.A	Corridor in the 4th floor	corridor	9	9	1
W4.B	Corridor in the 4th floor	corridor	9	9	3.9
W4.C	Corridor in the 4th floor	corridor	9	9	8.5
W4.D	Corridor in the 4th floor	corridor	9	9	12.7
W4.E	Corridor in the 4th floor	corridor	9	9	18.2
W6.A	Conference Room in 6th floor	Within a room	9	9	5.1
W6.B	Conference Room in 6th floor	Within a room	9	9	6.2
D1.A	Tx in Room 475 Rx in Room 471	Room-to-room	9	9	Varying
D1.B	Tx in Room 475 Rx in Room 471	Room-to-room	9	9	Varying
D1.C	Tx in Room 475 Rx in Room 476	Room-to-room	9	9	Varying
D2.A	Hallway in 4th floor	Hallway with concrete walls	9	9	8.2
D2.B	Hallway in 4th floor	Hallway with concrete walls	9	9	14.6
D2.C	Hallway in 4th floor	Hallway with concrete walls	9	9	20.4
D3.A	Hallway + open environment	Hallway with open space in the middle	9	9	20.3
D3.B	Hallway + open environment	Hallway with open space in the middle	9	9	30.7
D4.A,B,C	Tx and Rx both in Room 476, MPRG Lab.	Cubical office Environment	3x9	3x9	Varying
D5.A	Tx in Room 423, MPRG Reception, Rx in Room 433	LOS/NLOS , Room-to-Room	3	3	5.6
D5.B	Tx in Room 423, MPRG Reception, Rx in Hallway	Room-to-Hallway, (obstructed, NLOS)	9	9	5.9
D5.C	Tx in Room 423, MPRG Reception), Rx in Hallway	Through glass wall	9	9	7.5
D5.D	Tx in Room 423, MPRG Reception), Rx in Hallway	Through glass wall	9	9	9.5

4.4.1. Results for Indoor LOS and NLOS Measurements

In this section, several LOS scenarios corresponding to locations W2.E, W4.E, W6.B, D1.B, and D4.A, as representative examples, are presented and compared with their time-domain counterparts reported in [Muq03]. These results are given in Appendix C. For each scenario the first plot given in each figure shows the spectrum of the impulse response; that is, the transfer function of the system versus frequency in GHz. The second plot illustrates the impulse response, while the third plot depicts the received pulse versus time in ns. Such set of plots is initially shown for the measurements taken by biconical antennas, then repeated for those taken by TEM horns. Therefore, for instance, Figure C.1 corresponds to the measurements taken by biconical antennas in the hallway on the 2nd floor of Whittemore Hall, approximately at 15.4 m antenna separation. Similarly, Figure C.2 is for the same location but, instead, it depicts the response obtained by TEM horns. These example scenarios are specifically chosen so as to explore the effects at disparate environments. The hallway in the second floor of Whittemore Hall is a typical hallway in office building environments. The fourth floor includes corridors between laboratories, usually much smaller in width and height. The sixth floor measurements shed some light on the UWB performance in a room filled with many accessories such as tables, chairs, picture frames, and so forth. Durham Hall measurements examine a room-to-room scenario along with a typical cubical office environment.

In order to assess the agreement between the time-domain and frequency-domain measurements, a percent difference in received pulse energy is defined for each set of plots provided. For the frequency-domain spectral representation (transfer function), the percent difference between two methods – direct frequency-domain measurements and time-domain counterparts – is taken in modulus form and averaged out by the number of points. The bandwidth used for these computations is from 1 to 11 GHz. For the time-domain received voltage signals, the energy is computed through squaring the points, then the percent difference is evaluated in a manner similar to the case of frequency domain mentioned above.

It is observed that the results when compared in the time domain exhibit less difference between the two methods than when compared in the frequency-domain. Table 4.2 summarizes the percent differences obtained for each scenario. Overall, the differences are noted be less than 15% between the two methods for the FD representation and less than 5% for the TD representation. It should be kept in mind that the time-domain measurements [Muq03] were not recorded at the same time as the direct frequency-domain measurements; hence exactly the same locations and surroundings could not be realized for these LOS measurement scenarios.

Table 4.2 Percent difference in received pulse energy evaluated in time domain (TD) and frequency domain (FD) for selected LOS scenarios.

	TEM		**Bicone**	
	FD	**TD**	**FD**	**TD**
***W*2.E**	**11.17**	**4.25**	**9.72**	**3.28**
***W*4.E**	**23.64**	**2.47**	**10.04**	**1.99**
***W*6.B**	**16.05**	**2.21**	**8.97**	**2.25**
***D*1.B**	**15.65**	**3.90**	**13.35**	**14.45**
***D*4.A**	**15.17**	**2.40**	**15.03**	**5.68**

NLOS measurements are carried out in four different floors of Whittemore Hall both in time- and frequency-domains, and using both sets of antennas along with several receiver locations in each scenario. However, for the sake of brevity, results for only four different NLOS transmitter locations are given in Appendix C. In each figure, the first row corresponds to the measurement results from bicones and the second to those from TEM horns. The first column represents the transfer function in dB and the second one shows normalized received signal in volts. Examination of Table 4.3 indicates that the percent difference between the two measurement methods is less than 15% when frequency-domain representations are compared. When time-domain representations are compared the percentage difference is even less. However, percent differences for NLOS with TD representations are generally larger than those for LOS scenarios.

Table 4.3 Percent difference in received pulse energy evaluated in time domain (TD) and frequency domain (FD) for selected NLOS scenarios.

	TEM		**Bicone**	
	FD	**TD**	**FD**	**TD**
***Rx*4b**	**8.61**	**7.09**	**13.88**	**17.80**
***Rx*5c**	**11.65**	**5.71**	**10.90**	**4.95**
***Rx*9c**	**11.84**	**7.01**	**10.08**	**5.41**
***Rx*1b**	**12.87**	**1.05**	**16.28**	**4.51**

4.4.2. Small-Scale Statistics and Signal Quality

Small-scale fading in narrowband systems results in a significant reduction in signal level due to destructive interference of multipath components at the receiver resulting from sub-wavelength changes in the receiver position [Rap96], [Dur00]. However, in UWB systems, since there is a range of wavelengths rather than a single one, the change in the receiver position might be considered to be on the order of sub-spatial-width of the transmitted pulse. For UWB signals no destructive interference can occur over the entire bandwidth of the pulse. The largely invariant signal over the grid points confirms the absence of small-scale fading. In assessing this effect, the following term as a measure of signal quality is defined as in [Win98b],

$$Q = 10\log_{10} E - 10\log_{10} E_0, \tag{4.1}$$

where E is the received signal energy given by:

$$E = \int_0^T r^2(t)dt, \tag{4.2}$$

and $r(t)$ is the voltage amplitude of the measured multipath profile and T is the time where all multipath signals are completely damped and can be neglected. E_0 is the energy measured at a reference location, which is nominally chosen to be at a Tx-Rx separation of 1m. In the frequency-domain the energy expression can be obtained with the use of Parseval's theorem,

$$E = \int_0^\infty |r(t)|^2 dt = \int_0^\infty |R(f)|^2 df\ , \tag{4.3}$$

which can be approximated for practical signals as follows

$$E \approx \int_0^T |r(t)|^2 dt \approx \int_{f_{low}}^{f_{hi}} |R(f)|^2 df\ , \tag{4.4}$$

where f_{low} and f_{hi} are the lower and upper frequencies of the signal bandwidth. In this work, these frequencies are 100 MHz and 12 GHz.

In order to assess the signal quality, two specific locations are examined. First, five different LOS measurement sets involving 45 profiles in the 2nd floor of Whittemore Hall are clustered and the received energy is divided into different bins commensurate with the number of total profiles. Then, the number of occurrences is plotted against the specific bins. The emerging histograms for both sets of antennas are given in Figures 4.7a and 4.7b. The Tx-Rx separation distances for these LOS measurements range from 9m to nearly 50m. To understand this distribution better, the cumulative distribution functions are overlaid on these plots and a percent scale is provided on the left y-axis. Similarly, two different LOS measurement sets totaling 18 profiles in the conference room located on the 6th floor of Whittemore Hall are plotted in Figures 4.8a and 4.8b.

Figure 4.9 illustrates the cumulative distribution function (CDF) of the received energy collected locally at 9 points of the 3x3 grid. This figure includes 24 sets of measurements taken in Whittemore Hall and Durham Hall, totaling 216 energy measurements excluding the sets D5.A and D4.B (see Table 4.1) due to the fact that no received signal much different from the noise could be identified for these locations. The results are presented separately for different sets of antennas for clarity. Specifically, Figures 4.9a and 4.9b show the signal quality curves resulted with TEM horns and biconical antennas, respectively. From these figures it can be noted that there is only negligible small-scale fading due to interference for both sets of antennas. Cases such as the location D4 exhibited more fading than expected, mainly due to transmitter and/or receiver locations being too close to walls. In [Rap89] it has been mentioned that such obstruction during the measurement would result in undesired fading. It is observed that the shown profiles exhibit no more than 3dB difference when compared to their average signal quality levels. The robustness of UWB communication systems, insofar as multipath is concerned, is manifested by their small variations in signal quality at various grid locations [Sch97].

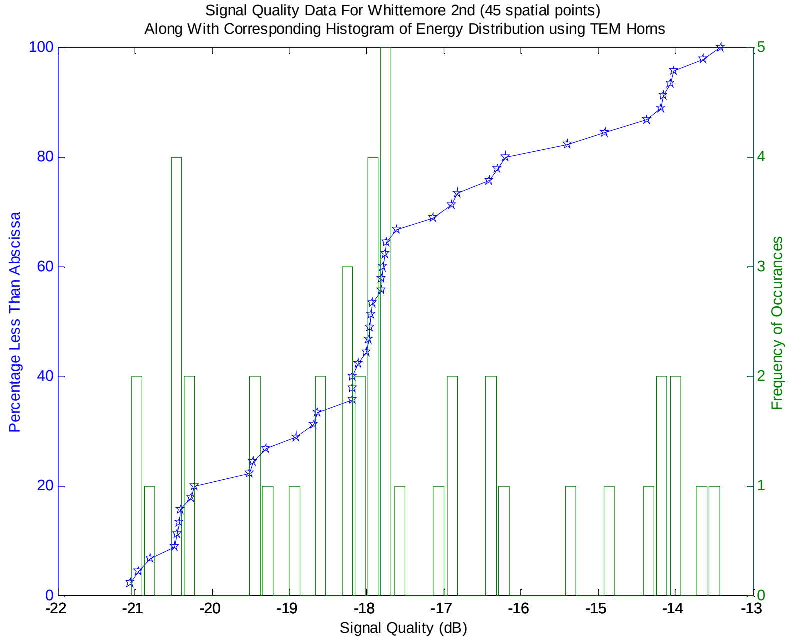

(a)

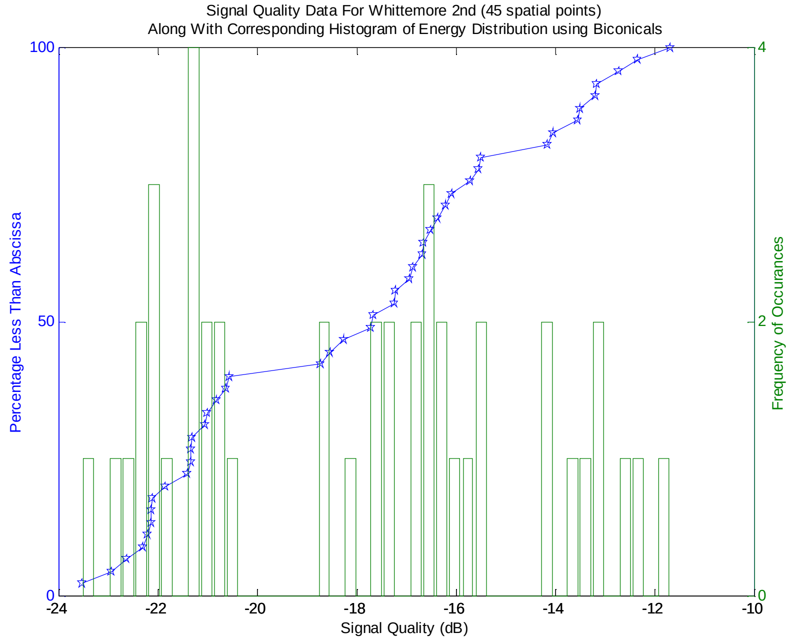

(b)

Figure 4.7 Histogram of energy distribution for Whittemore Hall, 2nd floor, LOS data and CDF of received energy at each specific measurement location (a) using TEM horns (b) using biconical antennas.

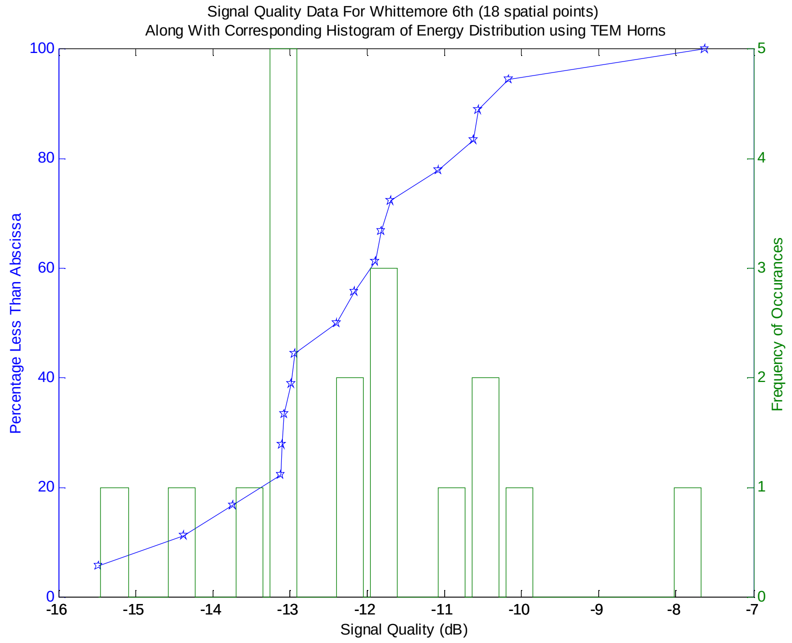

(a)

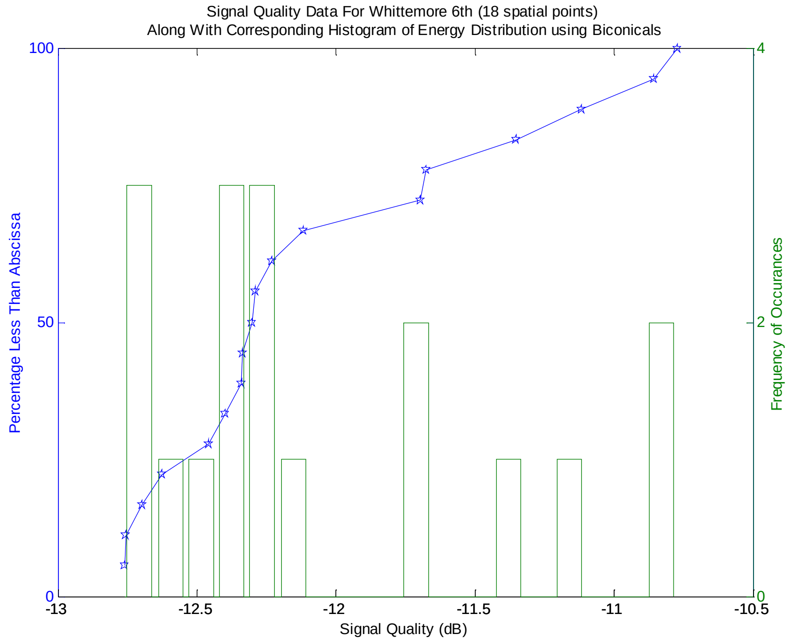

(b)

Figure 4.8 Histogram of energy distribution for Whittemore 6th floor LOS data and CDF of received energy at each specific measurement location (a) using TEM horns (b) using biconical antennas.

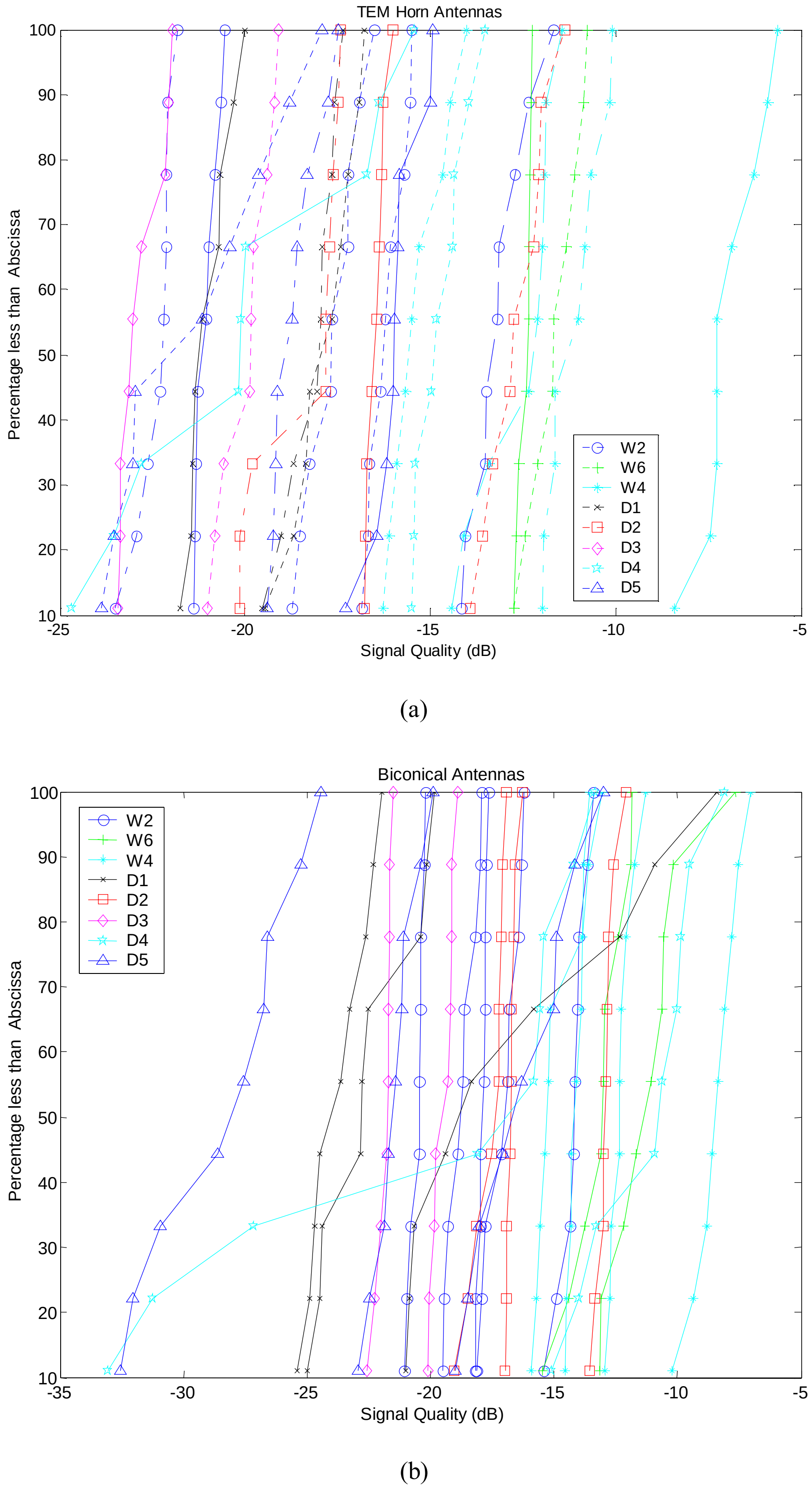

(a)

(b)

Figure 4.9 The cumulative distribution of signal quality based on 9 spatial sample points, (a) with TEM horns, (b) with bicones.

4.4.3. Large-Scale Analysis and Path loss

It is a well-known fact that the mean path loss, in a statistical sense, varies with $1/d^n$, where *d* is the transmitter-receiver separation and *n* is referred to as the path loss exponent for the medium of propagation. The exponent *n* represents the level of decay in signal power at certain distance. A simple model for path loss is as follows:

$$\overline{PL}(d) = \overline{PL}(d_0) + 10n\log_{10}\left(\frac{d}{d_0}\right) + X_\sigma, \tag{4.5}$$

where d_0 is the reference distance (usually chosen to be 1m), $\overline{PL}(d_0)$ is the average measured energy at the reference distance and X_σ is a zero-mean Gaussian distributed random variable in dB with an RMS value of σ dB [Rap96]. The far-field condition at high frequencies around and above 10 GHz may not be fully met; however, this has an insignificant impact on the results, as the radiated signal by the TEM horn is very weak above 10 GHz. Calculation of the path loss exponent and its standard deviation can be achieved by first plotting logarithmically a scatter curve of energy against distance. Next, a line fit through such a curve gives out the path loss exponent. In order to compute the standard deviation for the Gaussian random variable, one has only to obtain the deviation from the path loss exponent formerly obtained.

Equation (4.5) reveals the importance of an accurate reference measurement as it defines the intercept with the vertical axis and hence affects the slope of fitted line. In the current analysis, a reference measurement was carried out in the same environment wherein propagation measurements were performed. As a justification, a different set of reference measurements in a quasi-anechoic setting was collected; then a similar path loss analysis was undertaken and compared with the original reference measurements. It was readily observed that the exclusion of the multipath components that can be found in real environments decreases the total reference power. Thus, the measured power level relative to the reference value increases and consequently the slope of the fitted path loss exponent decreases. Also, the use of an omni-directional antenna versus a directional antenna may change the slope.

Distances were measured directly on the spot and also once for each scenario at the position (1,4) which corresponds to the center of the first row in the measurement grid. Using the grid dimensions and simple trigonometric relations, one can compute the distances corresponding to the remaining grid points. Using this approach, any small distance measurements were avoided and only one longer transmitter-receiver separation measurement was taken. Figure 4.10 shows the scatter plot for the entire set of propagation measurements including LOS and NLOS for both sets of antennas.

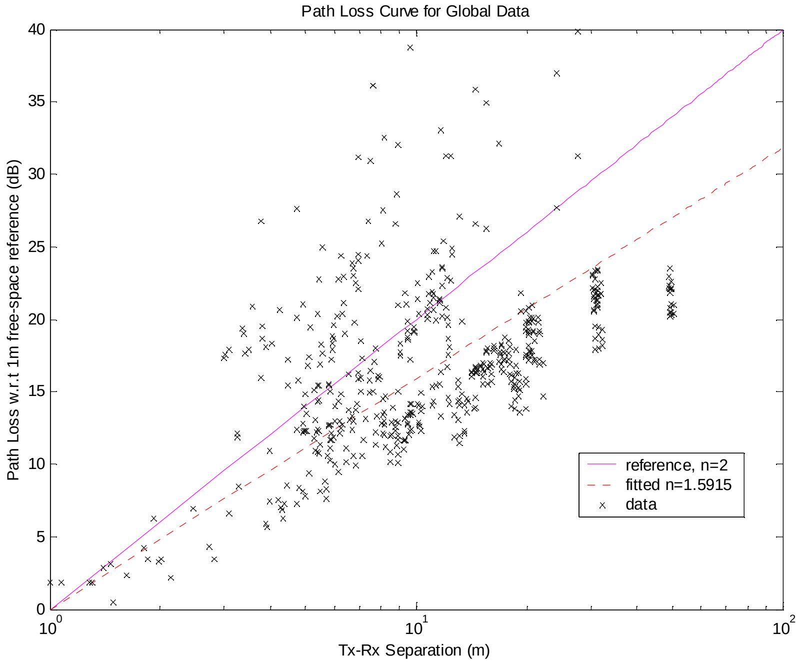

Figure 4.10 Path loss versus distance for the entire set of propagation measurements including LOS and NLOS for both sets of antennas.

Table 4a summarizes computed large-scale parameters from the measurements and Figures 4.11 and 4.12 exhibit the scatter curves for LOS and NLOS. It is observed that the minimum path loss exponent is 1.17 and 1.21 for the case of the narrow corridor located on the 4th floor, Whittemore Hall – a channel resembling a lossy waveguide structure. The maximum path loss exponent is 2.33 and 2.48 in the obstructed scenario D1 in Durham Hall. The global line-of-sight parameters are n=1.54 and σ=5.29 dB for the TEM horns and n=1.53 and σ=4.00 dB for the biconical antennas. Generally, for NLOS scenarios path loss exponents are greater than 2 and also have larger σ values associated with them. A global set of parameters is obtained for the NLOS scenarios in Whittemore Hall. These are n=2.37 and σ=9.22 dB for TEM horns and n=1.97 and σ=6.02 dB for biconical antennas. Figures 4.13a and 4.13b illustrate the path loss versus frequency for TEM horns and bicones, respectively. The higher path loss exponent for TEM horns is due to the fact that these antennas are very directional and less energy is captured by the receive antenna in NLOS positions. On the other hand, omni-directional biconical antennas would capture more energy of the transmitted pulse. Figure 4.14 compares the path loss exponents obtained from time-domain measurements [Muq03] with those obtained in this work using frequency-domain measurements. Tables 4a and 4b contrast the path loss exponents from the two measurement techniques for different scenarios.

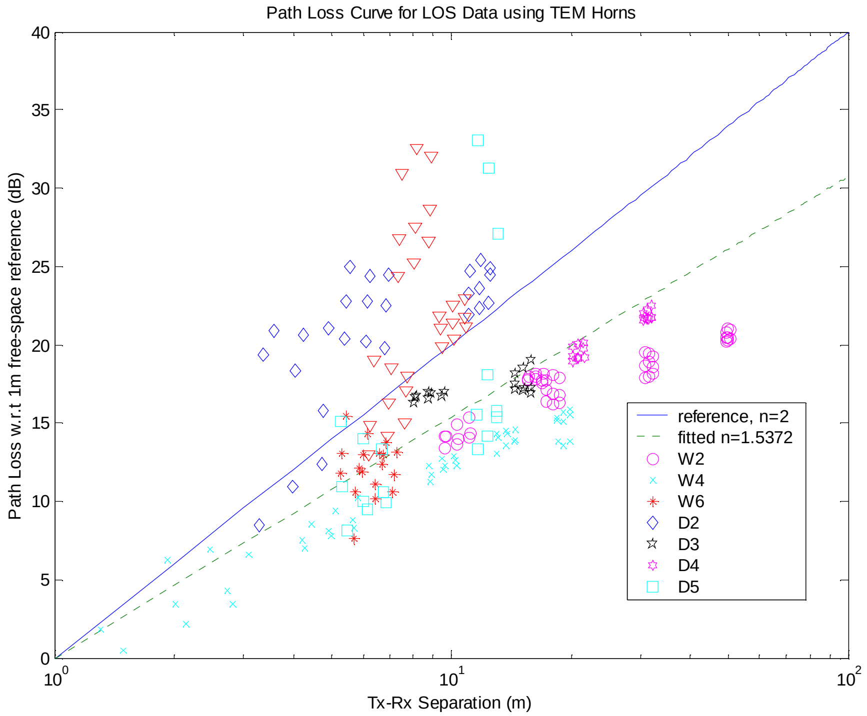

(a)

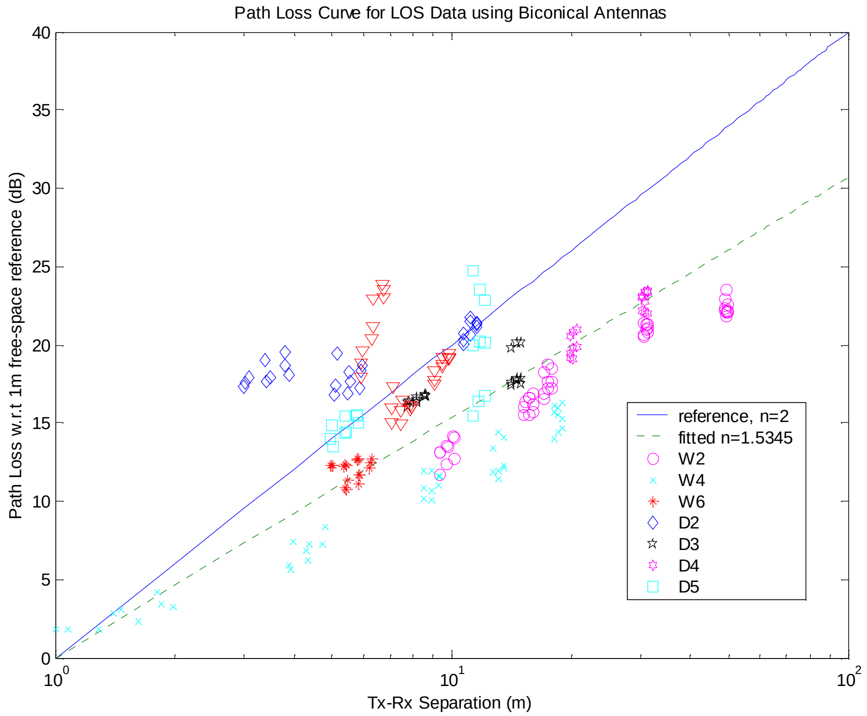

(b)

Figure 4.11 Scatter plot for the relative path loss versus frequency for all locations and LOS, (a) for measurements with TEM horn antennas, (b) for measurements with biconical antennas.

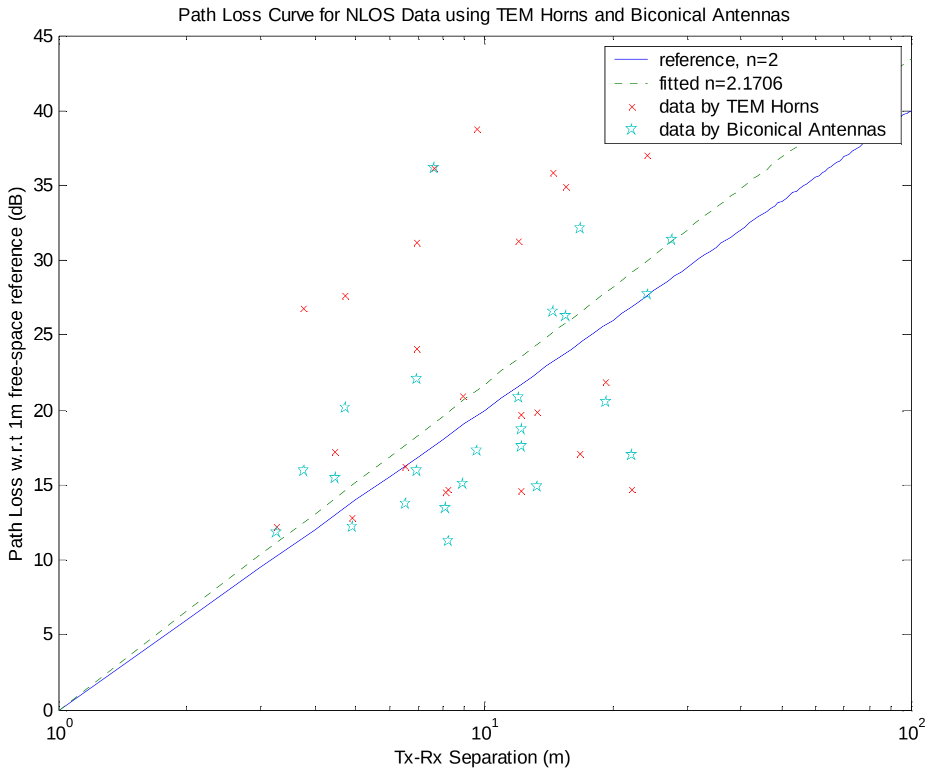

Figure 4.12 Overall scatter plots for path loss versus distance for NLOS scenarios.

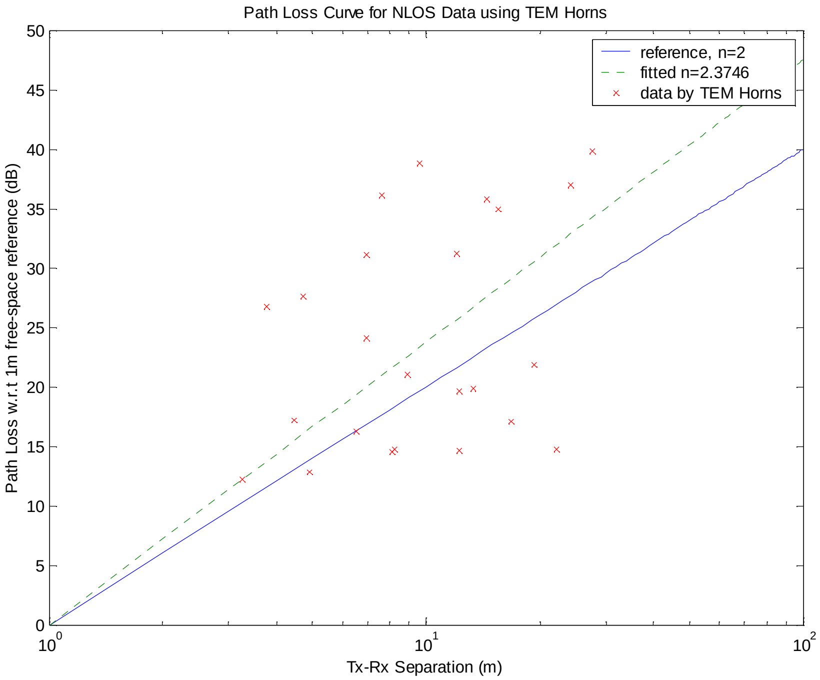

(a)

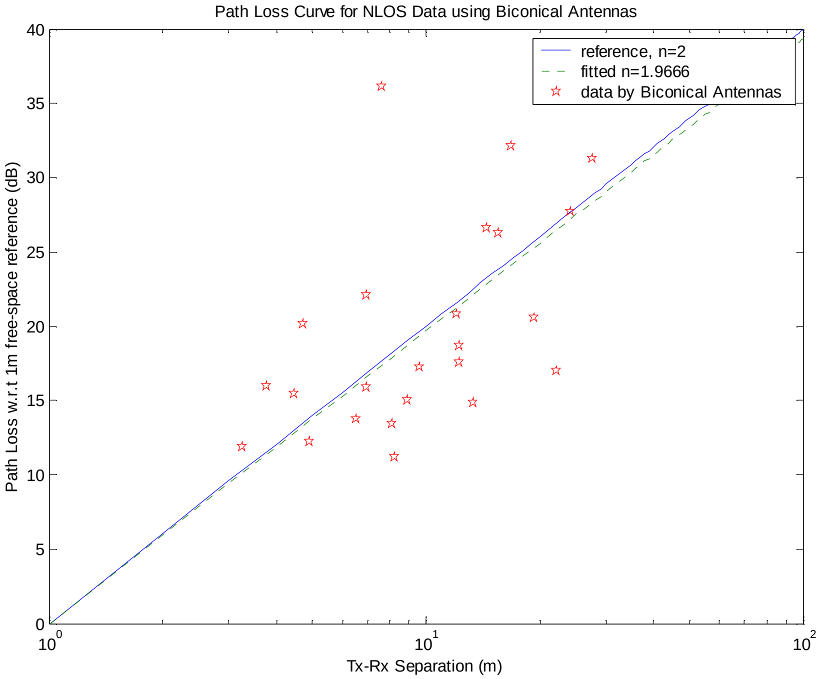

(b)

Figure 4.13 Path loss curves for NLOS scenarios using (a) TEM Horns (b) biconical antennas.

Table 4.4 Large-scale path loss parameters for both TEM horn and biconical antennas:

(a) Using frequency-domain approach,
(b) Using time-domain approach [Muq03a].

Antenna Type	*TEM Horn*		*Biconical*	
Location	n	σ	n	σ
W	**1.2973**	**1.6406**	**1.3281**	**1.5736**
W2	**1.3099**	**1.4292**	**1.3684**	**0.7838**
W4	**1.2074**	**0.9908**	**1.1668**	**0.9169**
W6	**1.5261**	**1.9015**	**1.6088**	**0.7678**
D	**1.7849**	**6.1580**	**1.7495**	**4.3407**
D1	**2.4789**	**3.8909**	**2.3269**	**3.9052**
D2	**1.6006**	**1.6016**	**1.6687**	**1.4131**
D3	**1.4696**	**0.3855**	**1.5314**	**0.6167**
D4	**1.7250**	**5.9602**	**1.9150**	**2.3777**
D5	**2.3952**	**5.1387**	**2.0875**	**3.3386**
LOS	**1.5372**	**5.2874**	**1.5345**	**4.0016**
NLOS	**2.3746**	**9.2273**	**1.9666**	**6.0288**

W: Whittemore Hall, D: Durham Hall

(a)

Antenna Type	*TEM Horn*		*Biconical*	
Location	n	σ	n	σ
W & D	**1.8274**	**5.7291**	**1.7482**	**4.2585**
W	**1.5602**	**1.7196**	**1.5653**	**2.0095**
W2	**1.5454**	**1.6763**	**1.5807**	**1.3494**
W4	**1.2744**	**0.4763**	**1.3035**	**1.9032**
W6	**1.7845**	**0.7160**	**1.8192**	**1.0235**
D	**2.0401**	**6.5007**	**1.9103**	**4.8007**
D1	**3.2883**	**2.6456**	**2.9655**	**1.8769**
D2	**1.6591**	**1.0542**	**1.5365**	**1.5381**
D3	**1.7986**	**2.3358**	**1.7983**	**2.2394**
D4	**1.6478**	**1.3841**	**1.7870**	**3.9154**
D5	**2.6701**	**5.6894**	**2.2455**	**1.8009**
LOS	**1.6077**	**1.5816**	**1.5826**	**1.9135**
NLOS	**2.6039**	**6.0840**	**2.4118**	**3.2698**

W: Whittemore Hall, D: Durham Hall

(b)

Narrowband results by [Rap96] and UWB measurements by [Gha02] are comparable to the results presented above. [Rap96] states that n=1.6 to 1.8 for indoor narrowband LOS scenarios and n=4 to 6 for NLOS obstructed scenarios. UWB measurements by [Gha02] also provide some standard deviation values for the lognormal shadow approximation along with path loss exponents; n=1.7, σ=1.6 dB for LOS and n=3.5, σ=2.7 dB for NLOS scenarios. These results are in close agreement with ours presented in Table 4.4a.

Similar results based on time-domain measurements by [Muq03a] are in close agreement with the channel parameters obtained here, as demonstrated in Figures 4.14 and 4.15 as well as in Tables 4.4a and 4.4b. Figure 4.14 compares the signal quality; the left-hand-side plots show the CDF curves for both sets of antennas using the time-domain technique [Muq03a], while the right-hand-side plots are based on frequency-domain measurements. Moreover, in Figure 4.14, the frequency-domain plots include additional profiles than the time-domain counterpart - four in scenario W4 and one in scenario D5. For both sets of antennas, this additional profile in scenario D5, which corresponds to a NLOS measurement from room-to-hallway, there is 6 dB signal degradation. For one of the profiles in scenario D4, the frequency-domain based results indicate about 7 dB degradation in signal quality for TEM horns and 15 dB for bicones, whereas such degradations are not present in the time-domain counterparts. For all other profiles there is close agreement between signal qualities obtained from the two measurement techniques.

Figure 4.15 summarizes the path loss data for both techniques. The overall time-domain measurements in the left-hand-side plots [Muq03a] for both sets of antennas resulted in larger values of path loss exponent, n, when compared to the overall frequency-domain measurements shown in right-hand-side plots. This trend is excepted for the scenario D4 where frequency-domain data exhibited larger n, as tabulated in Table 4.4. Overall n and σ values are consistent for both sets of antennas and techniques. It should also be stated that the global LOS path loss exponents using TEM horns are very close to the ones using biconical antennas in both frequency- and time-domain measurements. Another point to be made is that the NLOS path loss exponents in frequency-domain are smaller than those reported in [Muq03a]. A reason for this difference is that additional NLOS measurements performed in the frequency domain contain scenarios where only a hallway door was used as an obstruction. Such scenarios in turn result in smaller path loss exponents on average due to high penetration capability of UWB signals through non-metallic obstructions. Another reason might be the larger sensitivity of the frequency domain measurement equipment compared with that of the time domain equipment, allowing weaker NLOS signals to be measured.

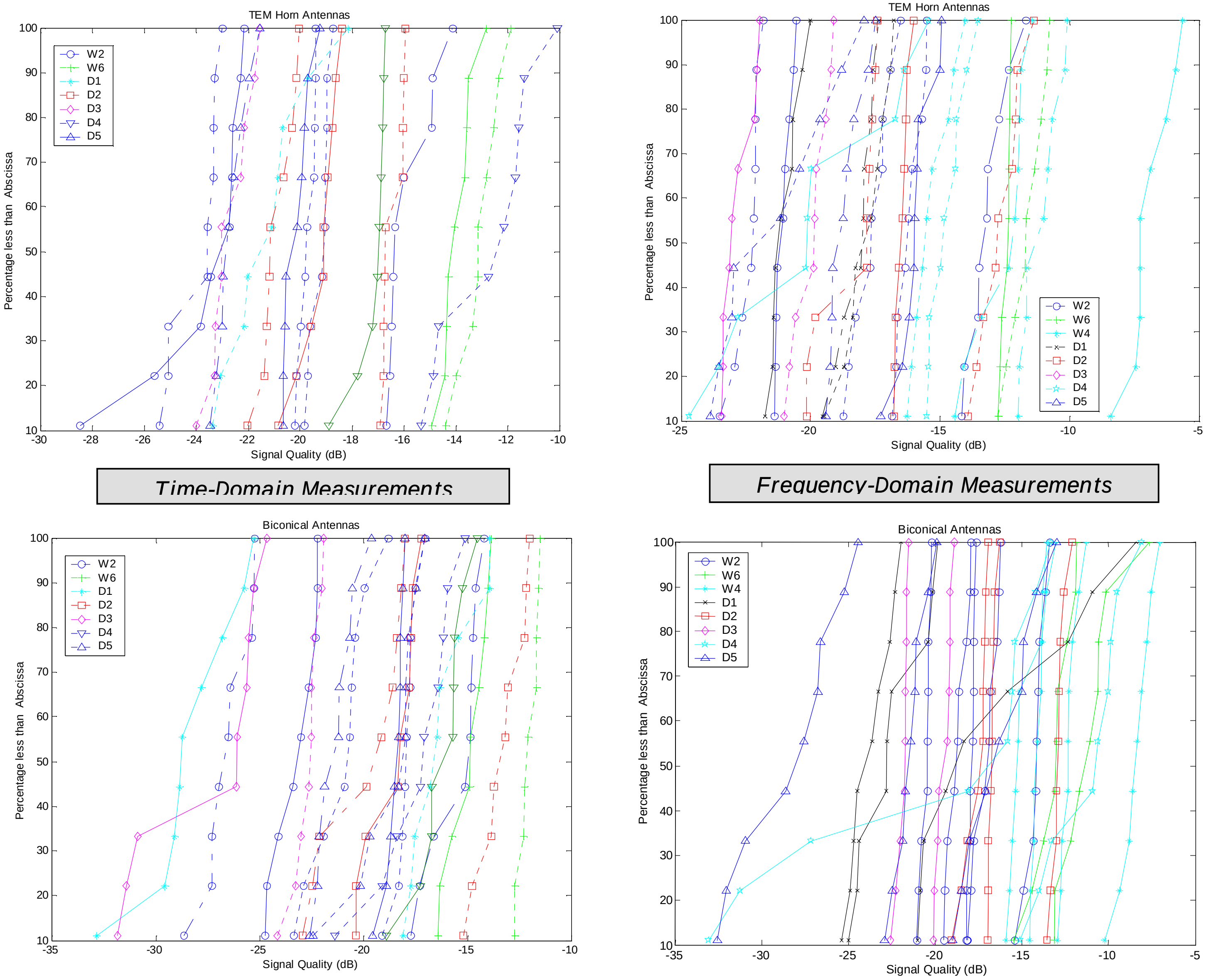

Figure 4.14 Comparison between the time-domain [Muq03a] and the frequency-domain measurements for signal quality measured by both TEM horns and the biconicals. The left- hand- side-figures compare time-domain results, while the right-hand-side figures compare the frequency-domain results.

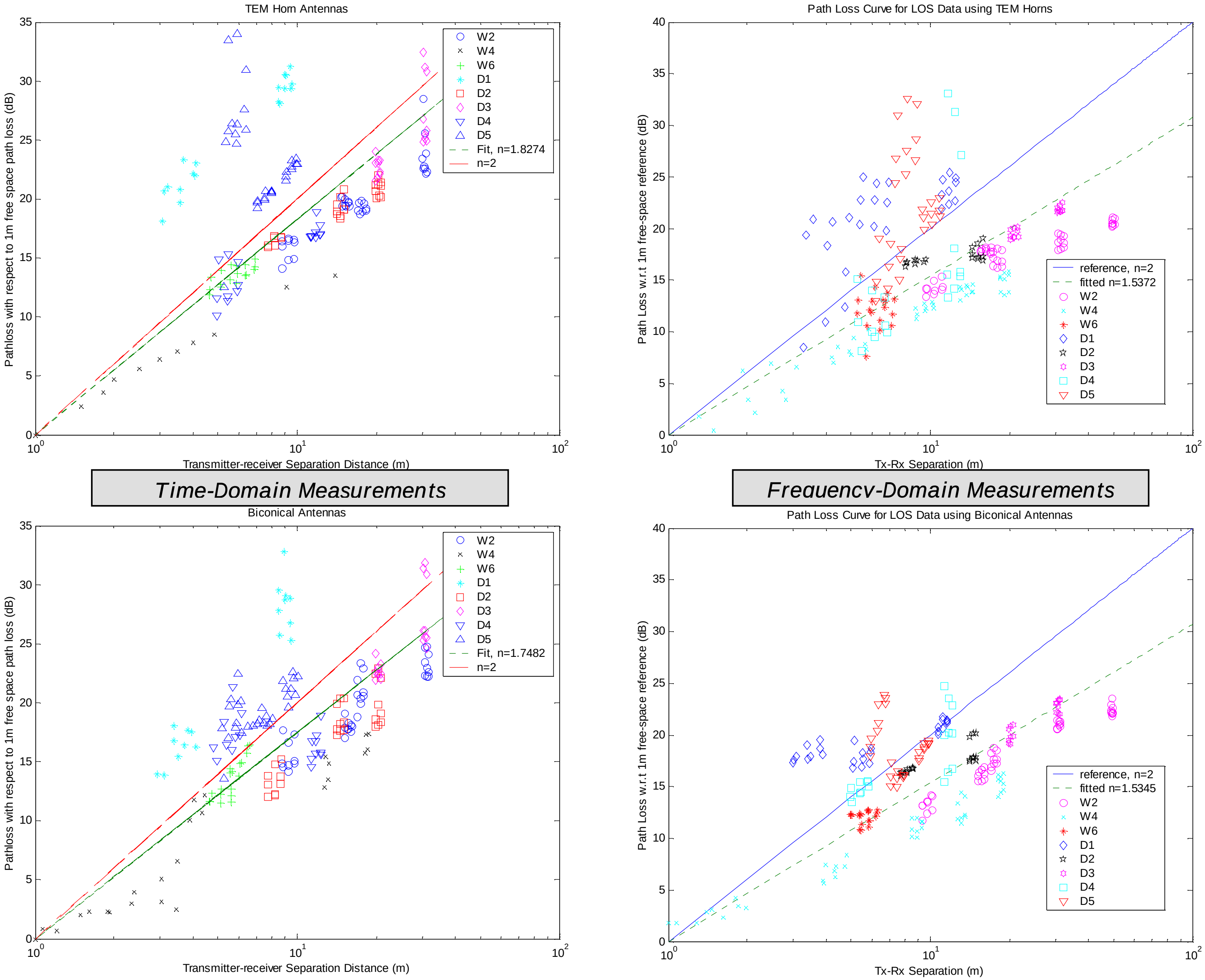

Figure 4.15 Comparison of path loss exponents obtained from time-domain measurements [Muq03a] and frequency-domain measurements (this work). The left-hand-side figures are the time-domain results.

CHAPTER 5

Signal Distortion

UWB signals suffer distortions due to frequency dependent antenna characteristics, dispersive behavior of building materials in the transmission medium, and the geometrical structures of propagation paths which give rise to multiple reflections and scattering. For instance, when propagating through walls, UWB signals suffer more severe degradations than narrowband signals, because of the effects of frequency dependent dielectric constants of wall materials in the propagation paths. In narrowband signals, the entire spectrum travels with same speed and suffers the same attenuation, thus no material dispersion effect. On the other hand, in ultra-wideband propagation, each spectral component of the signal undergoes a different amount of delay and suffers a different amount of attenuation, because the complex dielectric constant varies with frequency. In this chapter, signal distortions due to the antennas actually used in UWB channel measurements as well as distortions resulting from the inhomogeneity of certain building materials such as brick and concrete block are examined.

5.1. Antenna Distortions

In order to examine signal distortions caused by the TEM horns used in the indoor measurement campaign detailed in Chapter 4, we devise a setup with the TEM horns first placed horizontally at a height of 1m above the ground. The separation of the antennas is kept roughly at 3m, ensuring a far-field distance for the TEM horns. Then, the receiving antenna, attached to a rotary platform, is moved in the direction of interest. All measurements are observed with a digital oscilloscope and 2048 points are taken per frame using a sample interval of 5ps/point. This procedure corresponds to a 5ns/window configuration for each plot attained in this experiment. The pulse used in these measurements is identical to that used in indoor propagation measurements presented in Chapter 4.

As discussed in Chapter 2, antenna distortions can occur due to bandwidth limitations of the input impedance, directive gain, and the polarization of the Tx/Rx antennas. This study highlights the distortions due to variations of the antenna directive gain with frequency. To illustrate this distortion, the transmitting antenna is kept in a fixed position, while the receiving antenna is rotated in the direction of the spherical coordinate, θ, as shown in Figure 5.1. Received pulses are recorded along the angular directions corresponding to $\theta = 0$, $\pm 15^0$, $\pm 30^0$, $\pm 45^0$, $\pm 60^0$ in the yz-plane. It is emphasized that, strictly speaking, the angle θ is positive varying between 0 and 180 degrees. However, in Figure 5.1, θ is considered positive for y<0 and vice versa. Each received signal contains the LOS pulse and the first multipath from a nearby wall. Also, amplitudes in Figure 5.1 refer to individual waveforms and are not drawn to scale whereas time axes are identical. Comparison of received LOS pulses along different directions clearly indicates a gradual deterioration of the pulse shape away from $\theta = 0$ direction. This deterioration, or signal distortion, is attributed to two effects: (i) the antenna directive gain, $G(\theta,\phi)$, becomes less and less constant with frequency over the pulse bandwidth as $|\theta|$ increases, (ii) the phase of the radiated field becomes less and less linearly varying with frequency as $|\theta|$ increases. Figure 5.2 shows individual waveforms in the time domain corresponding to various profiles collected for different angles stated above. Similar measurements were carried out in the H-plane along different azimuthal directions, ϕ. It was noted that distortions in the H-plane were even worse than the case for the E-plane.

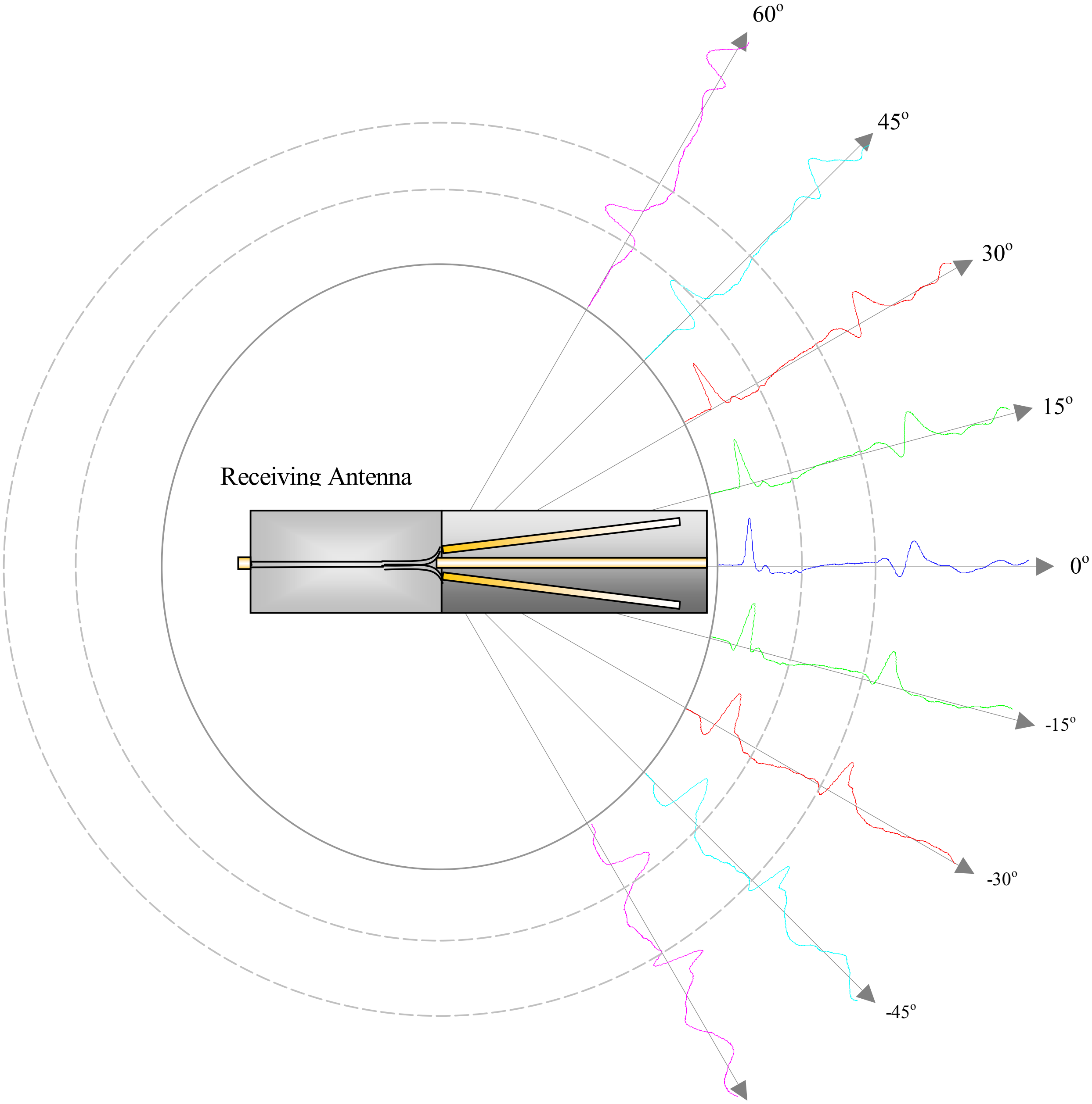

Figure 5.1 Received profiles upon rotation of the receiving TEM horn in the E-plane for angles from –60° to +60° presented in a polar form.

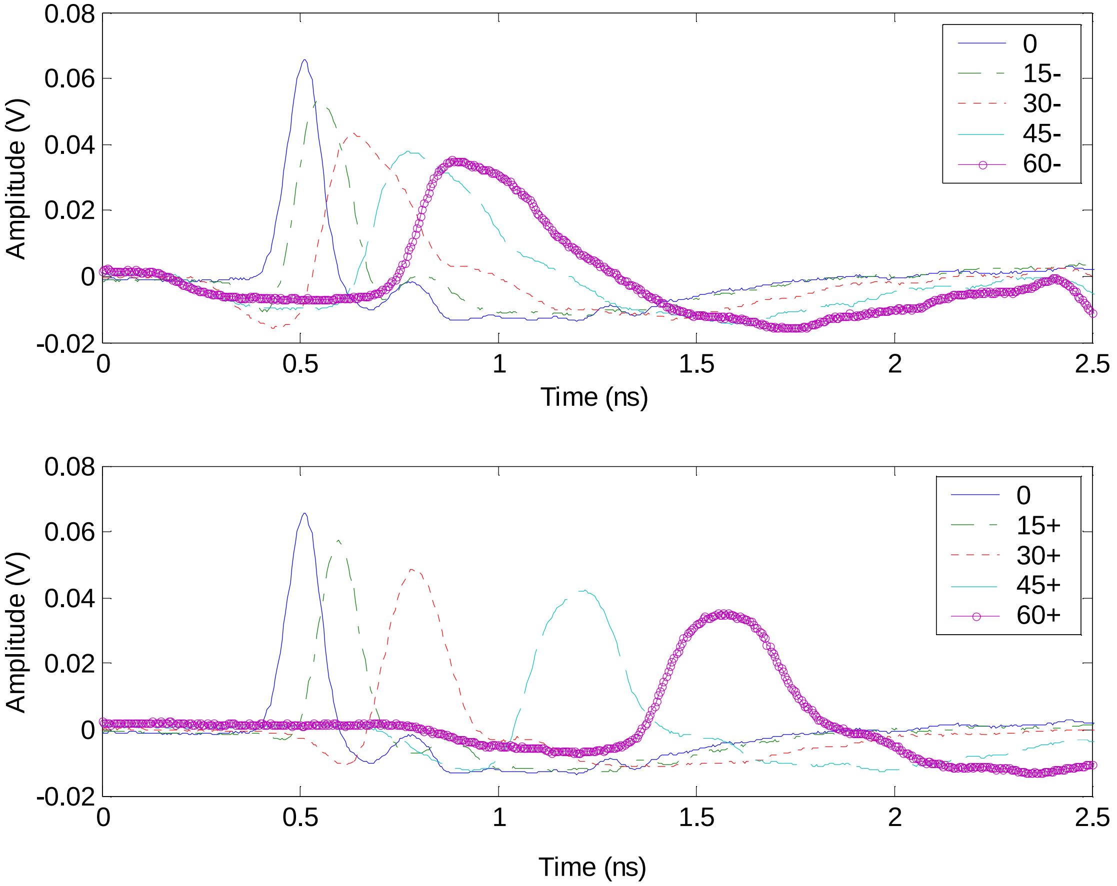

Figure 5.2 Received profiles upon rotation of the receiving TEM horn in the E-plane for angles from –60° to +60° shown in rectangular form.

5.2. Signal Distortion Due to Material Dispersion

In order to appreciate the significance of signal distortion in UWB applications due to dispersive behavior of building materials, let us examine the propagation of a short bipolar Gaussian pulse through a brick wall and a door. This problem can be treated using the transmission-line method in conjunction with the Fourier and inverse Fourier transforms. The waves incident on and refracted from the walls are assumed to be plane waves. The effects of transmitting and receiving antennas are not included in the simulation. The distance between the wall and either antenna is assumed to be large enough such that the plane-wave assumption holds. It is also assumed that the incident plane wave is normal to the walls. Using these assumptions, the problem can be reduced to a multiple section transmission line that can be solved systematically using a matrix approach [Ishi91]. Using this technique in conjunction with Fourier and inverse Fourier transform, transmission of a UWB pulse through walls can be simulated.

Figures 5.3a and 5.3b compare the free-space transmission with transmitted signals through a brick wall and a wooden door, respectively. The input signal is a bipolar Gaussian pulse, which is essentially the time-differentiated form of a monopolar Gaussian pulse generated upon radiation by a TEM horn antenna. It is noted that the signal transmitted through the brick wall has suffered significant distortions, whereas the signal transmitted through the door, apart from some loss, has largely maintained its shape. For brick, as will be implied in the next section, the dielectric constant (ε_r') varies more strongly with frequency than the dielectric constant of the door. This phenomenon together with the larger thickness of the brick wall compared to that of the door causes the transmitted signal through the brick wall to become more severely distorted than the signal transmitted through the door.

As an example of pulse distortion occurring in a UWB indoor environment, we consider a system of two walls as shown in Figure 5.4a where a brick wall precedes a wooden door. The received signal is obtained as shown in Figure 5.4b. It is apparent that in addition to distortion in the first pass signal, there is some ringing which can be attributed to multiple reflections between the walls.

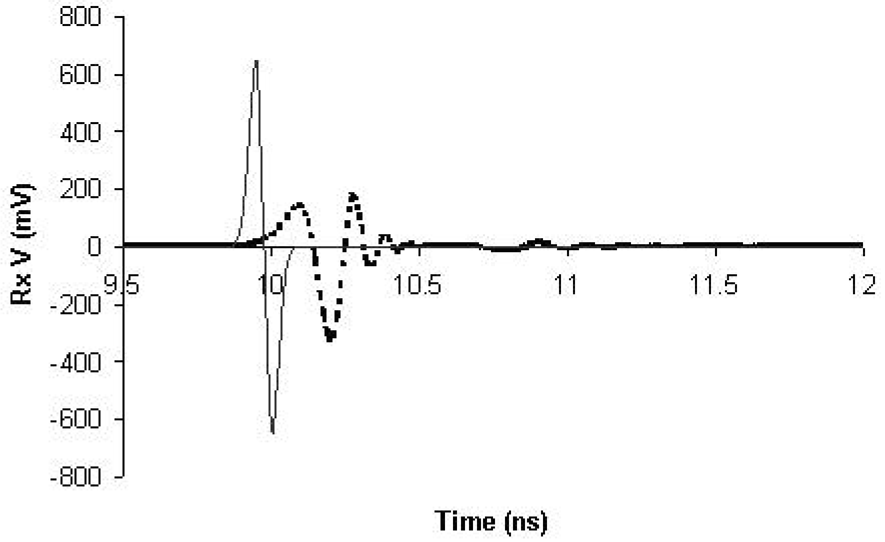

(a)

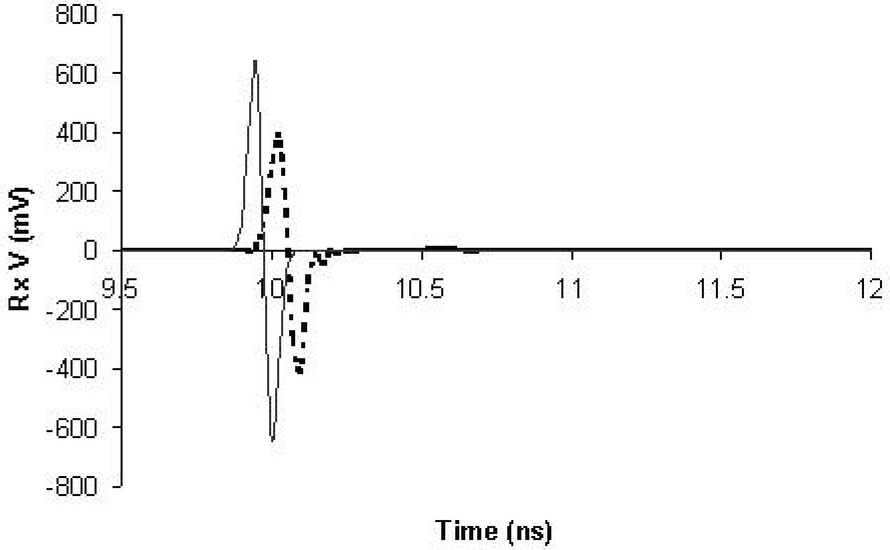

(b)

Figure 5.3 Comparison of free-space (solid line) and through-wall (dashed line) transmissions for (a) brick wall and (b) wooden door.

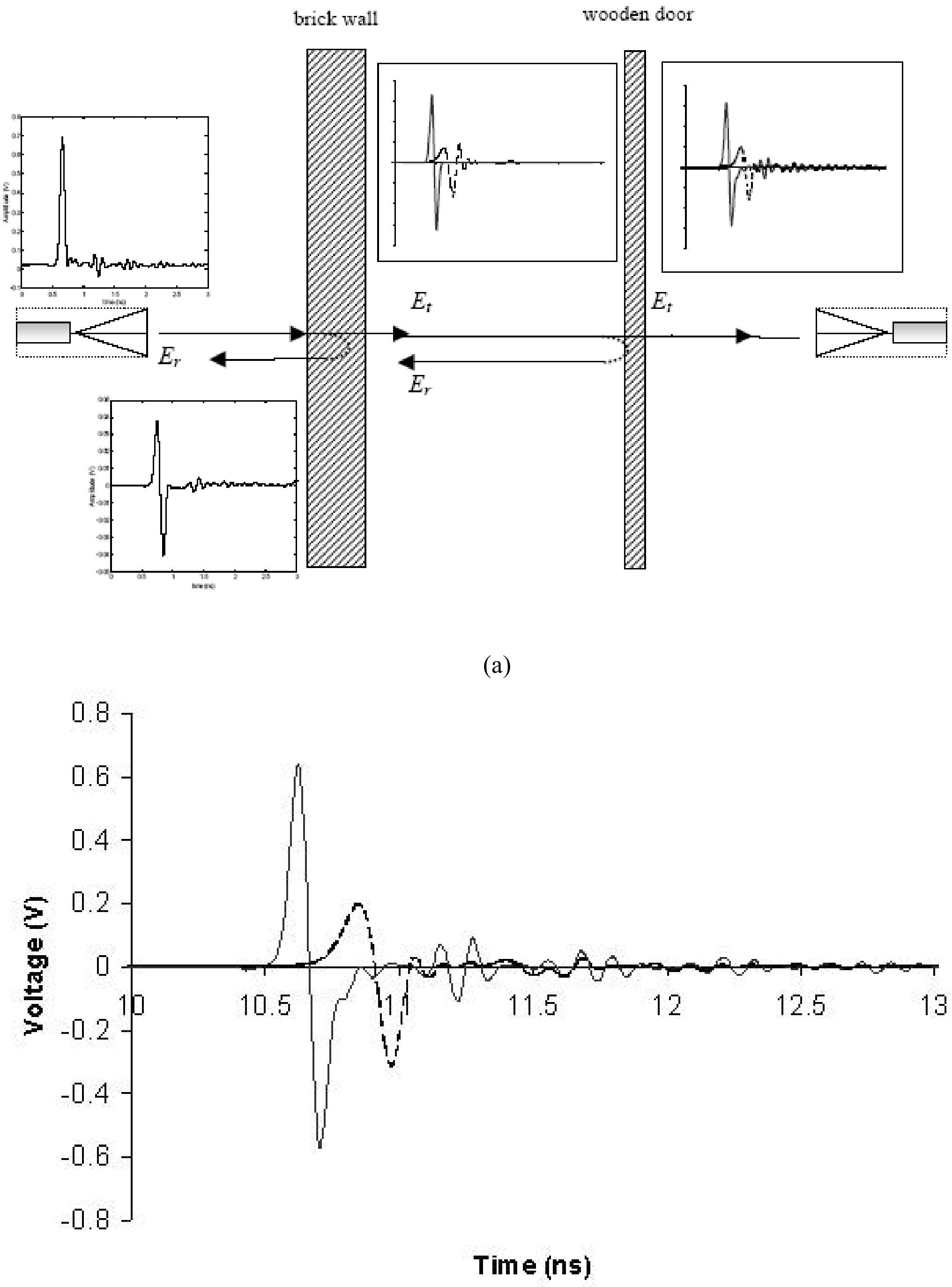

(a)

(b)

Figure 5.4 (a) Illustration for UWB partition dependent analysis using a brick wall and a wooden door (b) Comparison between free space transmission (solid line) and transmission through a brick wall and a wooden door separated by 20 cm (dashed line).

5.3. Simulation of Non-homogeneous Material for UWB Propagation

In order to investigate how material inhomogeneity of certain building materials such as brick might contribute to signal distortion, we calculate the equivalent dielectric constant of a wall consisting of two uniform loss-less $\left(\varepsilon_r^{''} = 0\right)$ slabs of permittivity $\varepsilon = \varepsilon_0 \varepsilon_r$ and thickness w separated by a distance d, as shown in Figure 5.5a. This wall is modeled as an equivalent uniform slab of total thickness 2w+d and effective permittivity, ε_{eff} , as shown in Figure 5.5b. The wall and its equivalent yield the same transmitted fields $\left(\vec{E}^t, \vec{H}^t\right)$ for the same incident fields $\left(\vec{E}^i, \vec{H}^i\right)$, thus the two walls have the same transmission coefficient $T = E^t / E^i$. The transmission coefficient of each wall can be derived by writing the electromagnetic fields in different regions and applying the boundary conditions at air-slab interfaces, as summarized in Appendix D. For given values of ε_r, d, and w, the effective dielectric constant of the equivalent wall can be determined. Figure 5.6 illustrates variations of the real part of the effective dielectric constant versus frequency for ε_r=4, w=2.2cm and several values of d.

These results clearly demonstrate the influence of the internal geometry of a nonuniform wall on the effective dielectric constant. In particular, it is observed that, for example, for d=4 cm the effective dielectric constant tends to increase with frequency. This behavior is consistent with that of the brick wall measured in [Muq04]. Also, the resonance behavior of loss tangent for block at several frequencies is attributed to its interior cavity-like structure. The variations of the effective dielectric constant with frequency amount to material dispersion, which in turn causes pulse distortions.

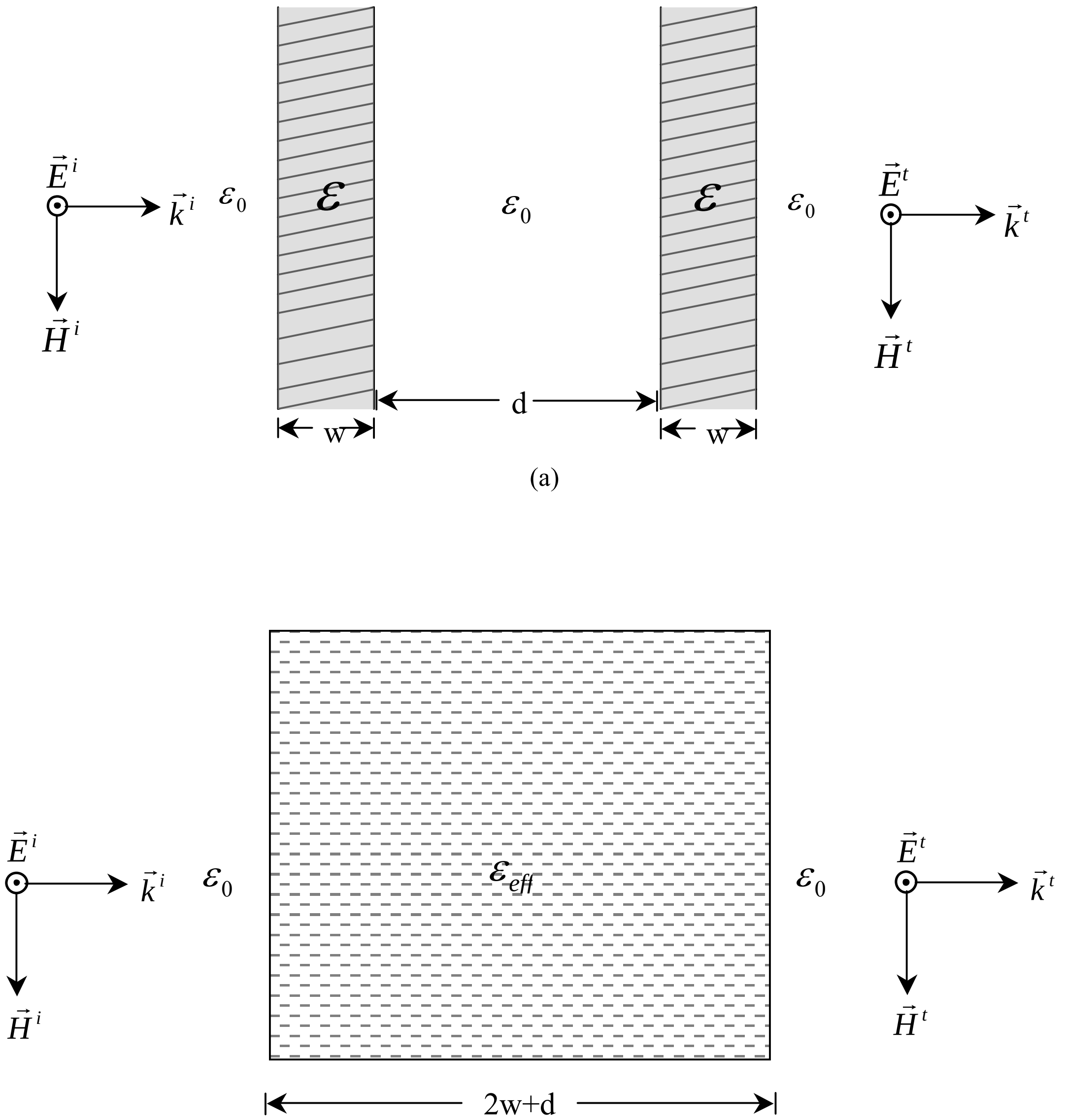

(a)

(b)

Figure 5.5 Geometry and parameters for (a) a nonuniform wall consisting of two slabs, and (b) its equivalent uniform wall of the same thickness.

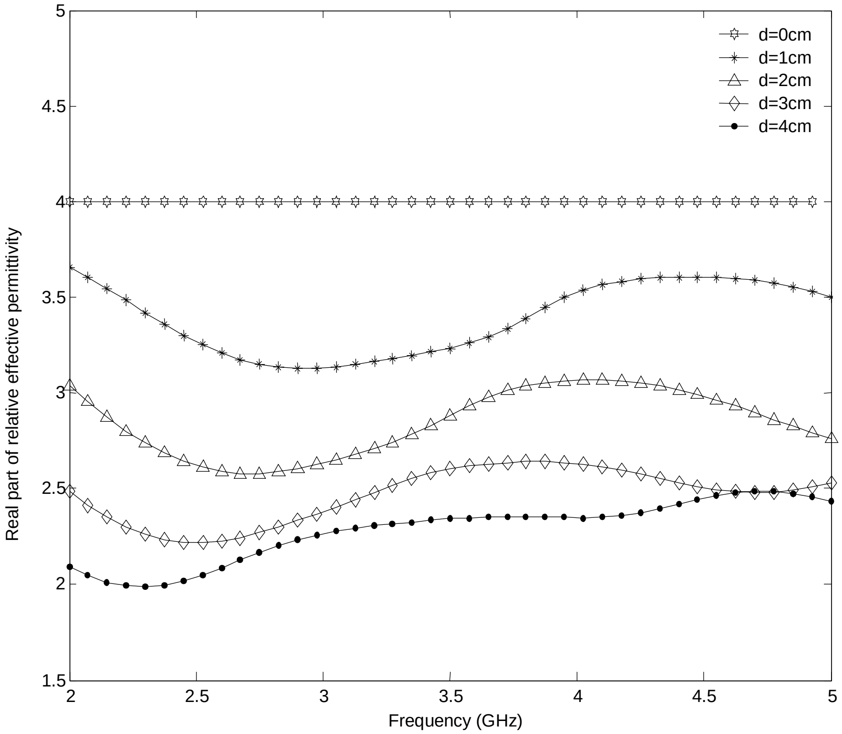

Figure 5.6 Variations of effective dielectric constant versus frequency for a nonuniform wall made of two slabs of dielectric constant ε_r =4.

CHAPTER 6

Concluding Remarks and Suggestions for Further Work

6.1. Conclusions

This thesis has addressed several aspects pertaining to ultra-wideband signal propagation, including the desired radiation characteristics of UWB antennas, frequency-domain measurements of UWB indoor channels, and distortions in UWB signals.

An ideal UWB antenna should maintain a frequency-independent input impedance and produce a radiated electromagnetic field whose magnitude, phase and polarization satisfy certain requirements over the UWB frequency range in order to prevent distortions in radiated signals. The role of UWB antennas in communication links has been discussed. Characterization of the antennas used in the propagation measurements has been carried out. In particular, radiation patterns, gain, and input impedance of two pairs of TEM horns over a bandwidth of nearly 10 GHz have been measured.

A frequency-domain technique based on amplitude measurements only has been presented. The underlying theory of this technique, in which the phase information is extracted from the measured amplitude data by means of a Hilbert transformation, has been analyzed. Extensive frequency-domain measurements aimed at characterizing indoor UWB propagation have been performed. The results have been compared to the time-domain measurements for the same locations and good agreement between the two methods has been noted in most cases. Different scenarios have been considered in this measurement campaign, including LOS, NLOS, within room, room-to-room, hallway-to-room, etc. Two types of antennas, directive TEM horns as well as the omni-directional bicones, have been used in the measurements. Small- as well as large-scale analyses have been performed, and path loss exponents for a large number of cases have been assessed. It has been shown that path loss exponents for LOS scenarios vary between 1 and 2, and for NLOS scenarios between 2 and 3. The frequency-domain measurements of UWB indoor channels reaffirms the fact that UWB systems can be very robust and less sensitive to small-scale fading and multipath interference.

Finally, various mechanisms contributing to distortion of UWB signals have been examined. In particular, pulse distortions resulting from variations of antenna directive gain with frequency and nonlinear phase characteristic of the radiated field have been demonstrated. Also, pulse distortion due to variations of the complex permittivity of walls with frequency has been discussed. It has been further shown that inhomogeneous materials such as brick and concrete block contribute to signal distortions. The results presented in this work may be used in further studies aimed at developing channel models for UWB wireless communication systems.

6.2. Future Work

UWB communication systems are still some steps away from full commercialization. A significant amount of research and development work need be devoted to UWB technology in order to make it efficient and cost effective. There exists a number of hurdles which must be overcome if this technology is to evolve as a viable and effective solution for wireless applications.

For instance, almost all existing antennas which are considered as likely candidates for UWB applications have either large sizes or lack sufficient bandwidth in gain, input impedance, and/or other radiation characteristics. It is thus imperative to improve the existing antennas or introduce novel antenna designs which will be able to meet the desired electrical and structural characteristics deemed necessary for efficient and commercially viable UWB communication systems. Much of the measurement results presented in this work have been for LOS scenarios. Extensive NLOS measurements are needed in order to be able to develop sufficiently accurate channel models. However, accurate calculation of phase from the amplitude data for NLOS scenarios is a challenging task. More research should be devoted to improving the phase extraction. Finally, an investigation of optimum pulse shapes resulting in minimum signal distortions is worth pursuing.

APPENDICES

Appendix A: Blueprints and Photographs of Locations for LOS Measurements

(b)

(c)

(squares represent transmitter locations, circles represent receiver locations)

Figure A.1 Blue prints for Whittemore Hall to illustrate measurement locations and environments.

(a) Hallways in the 2nd floor.
(b) Corridor in the 4th floor.
(c) Conference Room in the 6th floor.

(a) (b)

(c)

Figure A.2 Site Photographs in Whittemore Hall

(a) Hallways in the 2nd floor.
(b) Corridor in the 4th floor.
(c) Conference Room in the 6th floor.

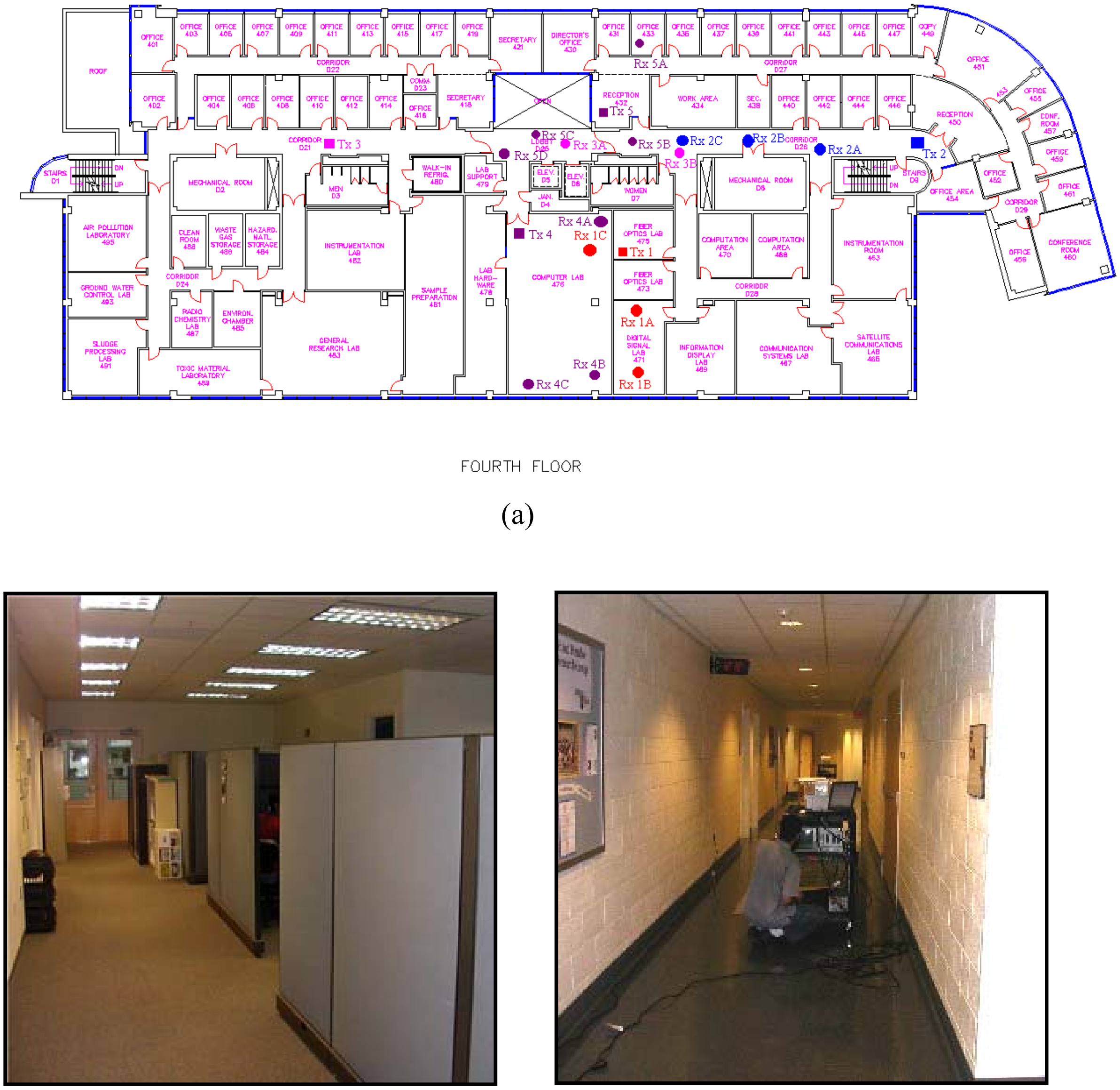

(a)

(b)

(c)

Figure A.3 Measurement Locations in Durham Hall (squares represent transmitter locations, circles represent receiver locations)

(a) Blueprint for the fourth floor of Durham Hall
(b) Photograph of location D4 with cubical partitions
(c) Hallways in Durham Hall, location D4.

Appendix B: Blueprints of Locations for NLOS Measurements

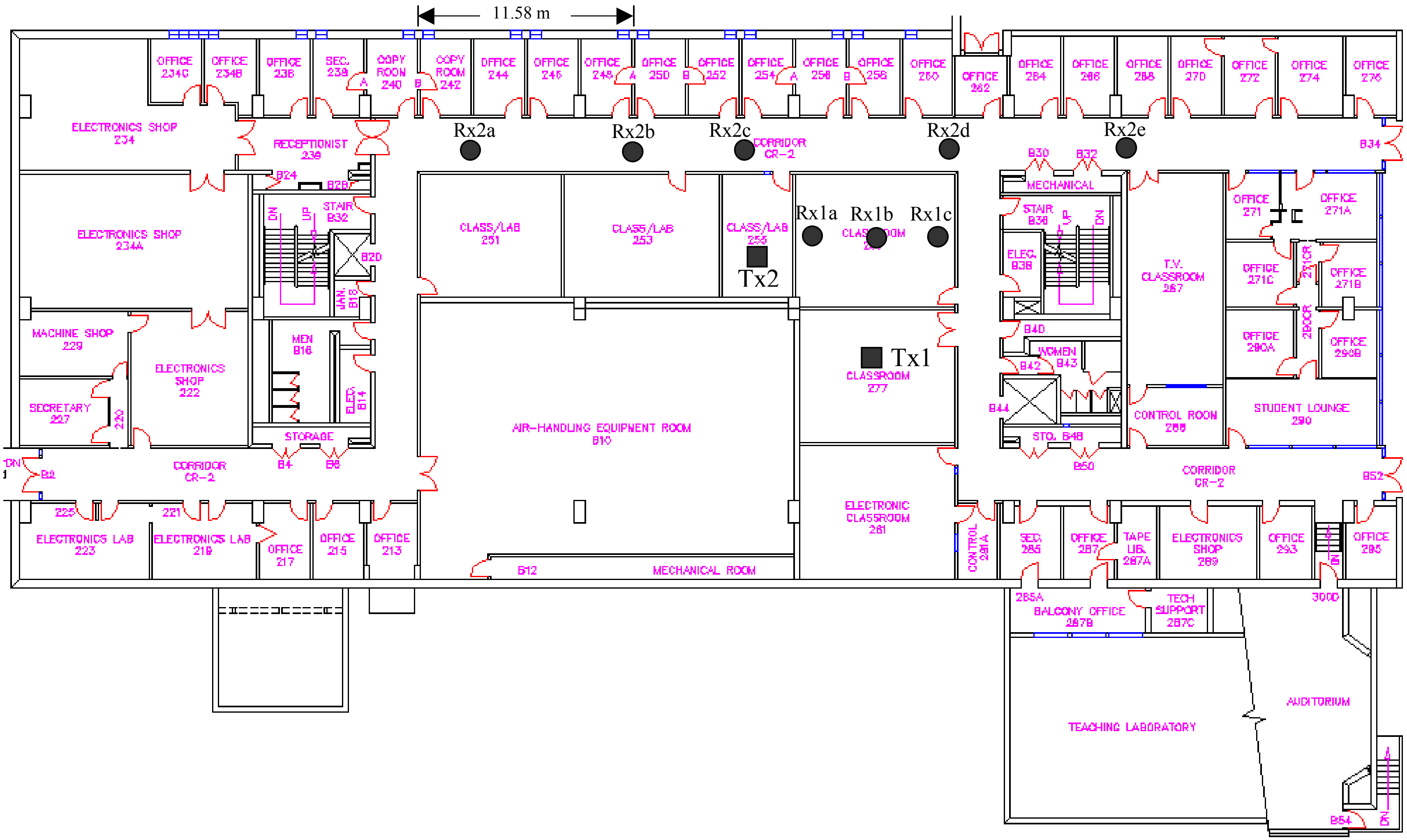

Figure B.1 Blueprint of Whittemore 2nd

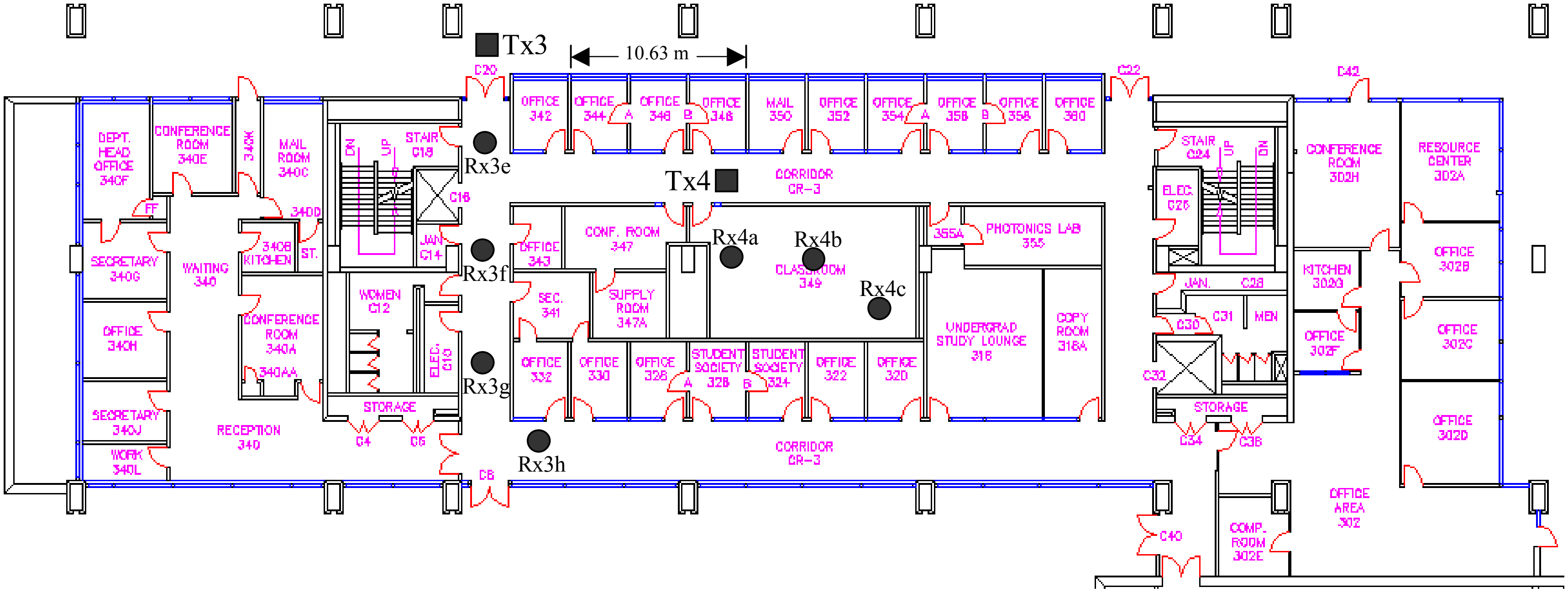

Figure B.2 Blueprint of Whittemore 3rd

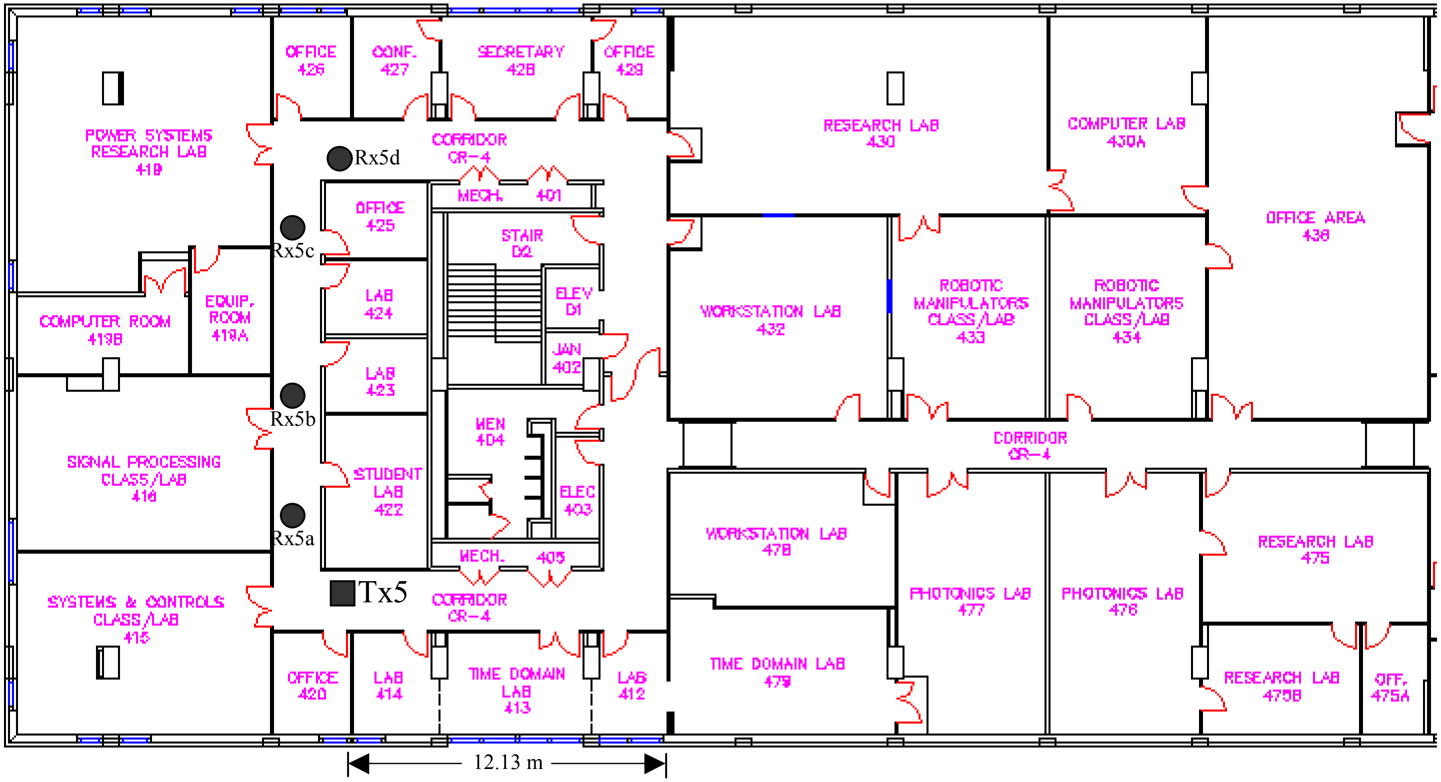

Figure B.3 Blueprint of Whittemore 4^{th} (partial)

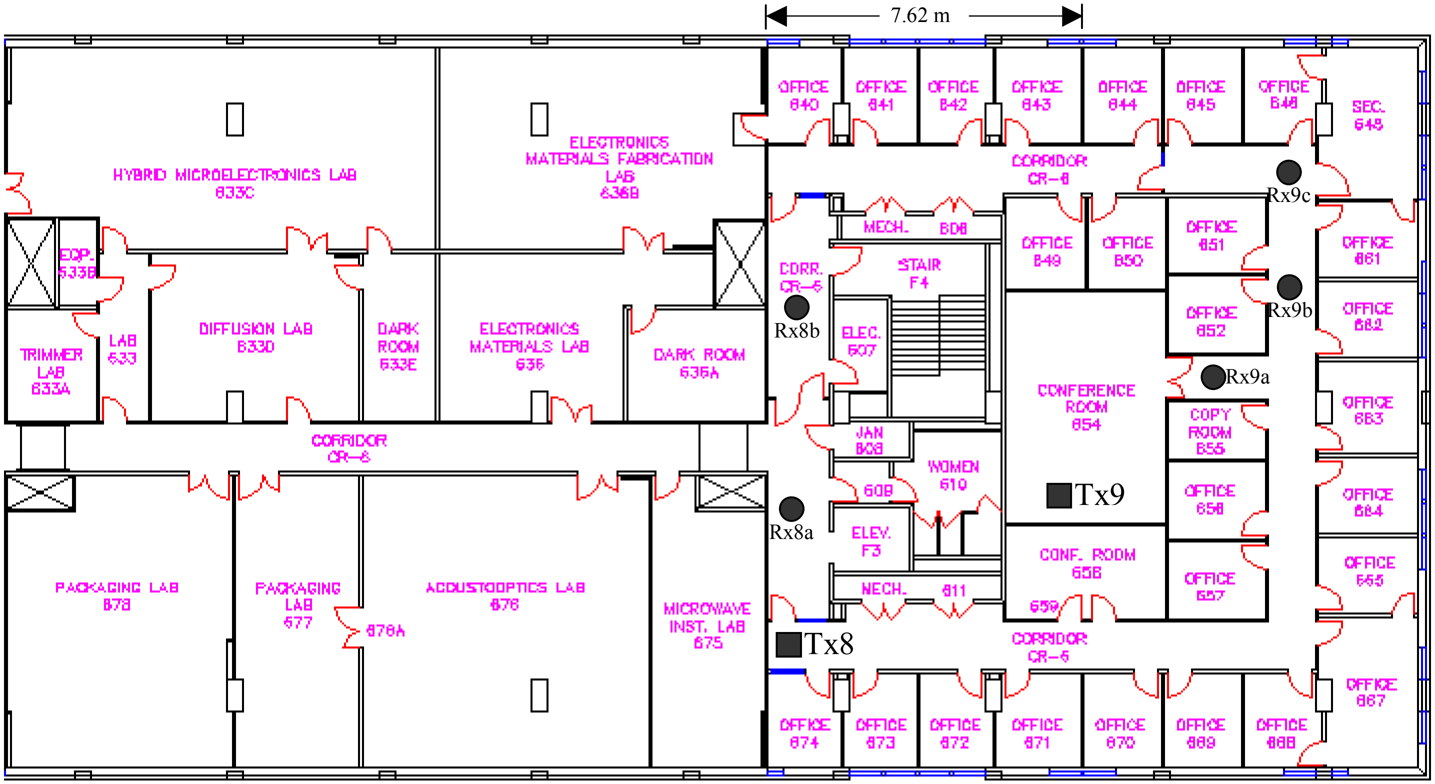

Figure B.4 Blueprint of Whittemore 6th

Appendix C: Sample Measurement Profiles for Indoor UWB Channels

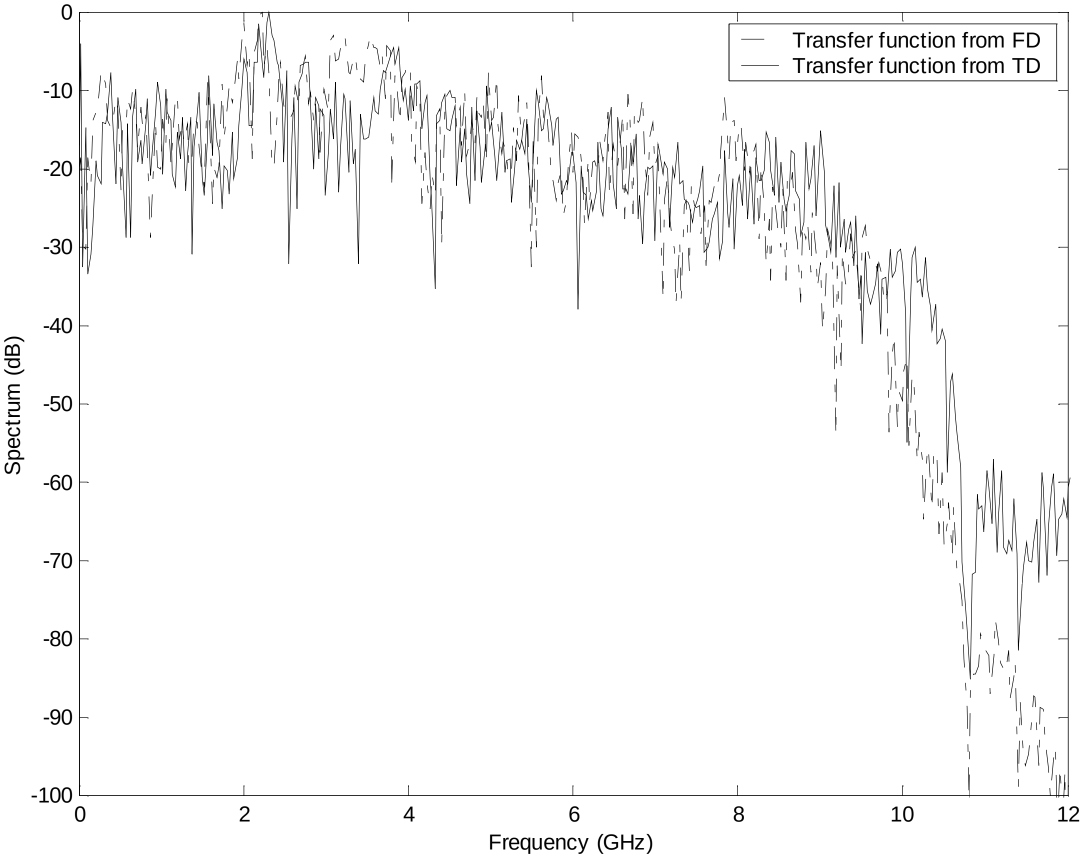
Spectrum (dB)
0
-10
-20
-30
-40
-50
-60
-70
-80
-90
-100
Frequency (GHz)
0
2
4
6
8
10
12
Transfer function from FD
Transfer function from TD

(a)

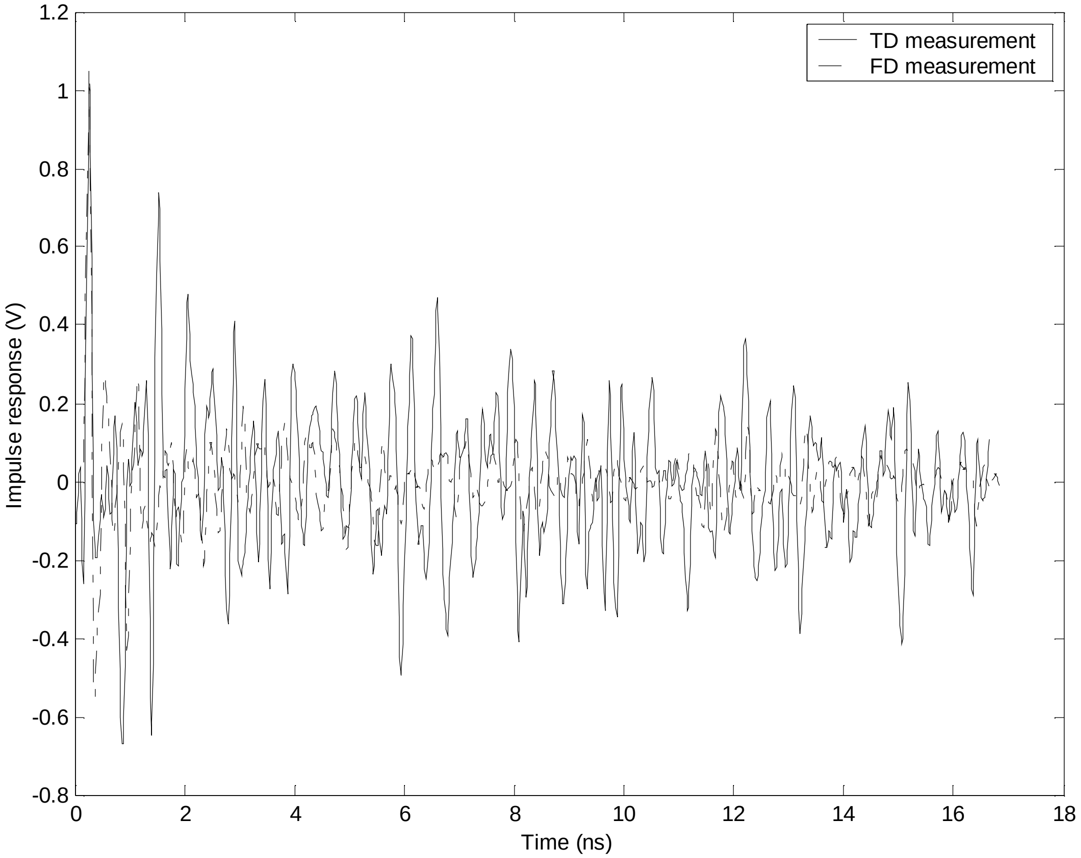
TD measurement
FD measurement
Impulse response (V)
Time (ns)
1.2
1
0.8
0.6
0.4
0.2
0
-0.2
-0.4
-0.6
-0.8
0
2
4
6
8
10
12
14
16
18

(b)

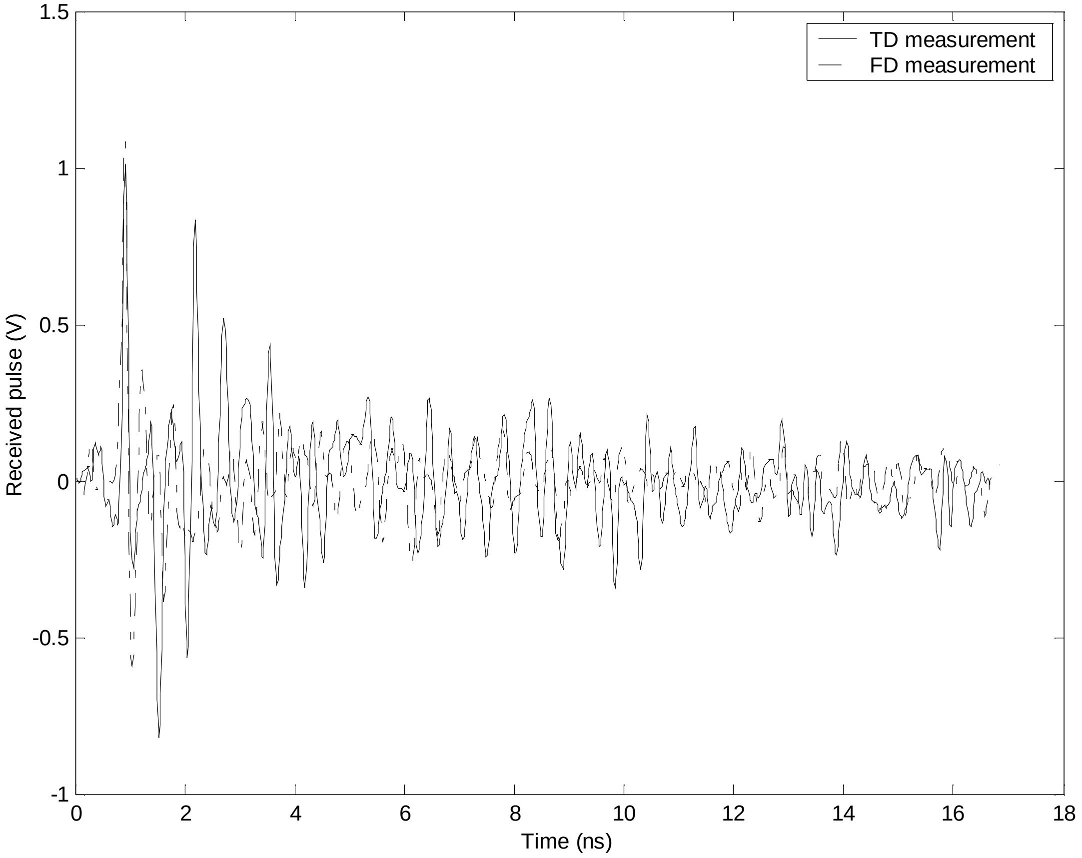

(c)

Figure C.1 LOS measurements with bicone at the location W2.E; d_A=15.4m
(- - - -) FD measurement, (──) TD measurement

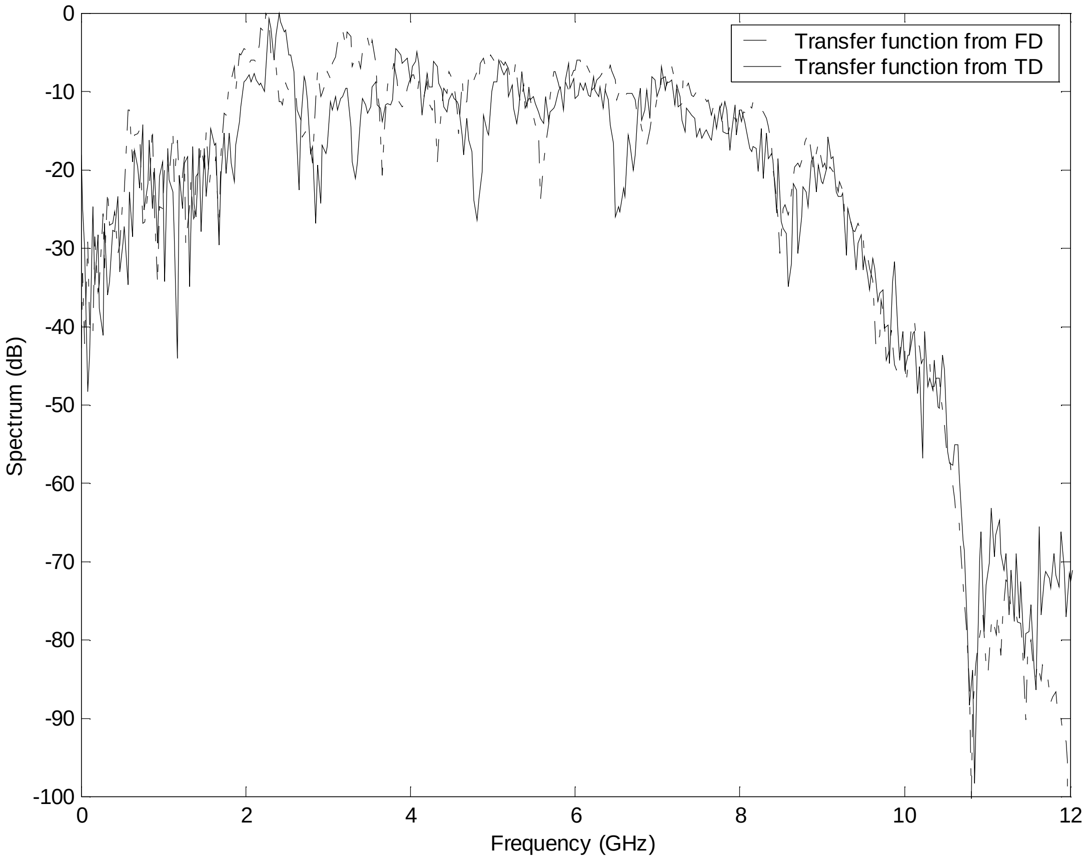

Transfer function from FD
Transfer function from TD
Spectrum (dB)
Frequency (GHz)
0
-10
-20
-30
-40
-50
-60
-70
-80
-90
-100
0
2
4
6
8
10
12

(a)

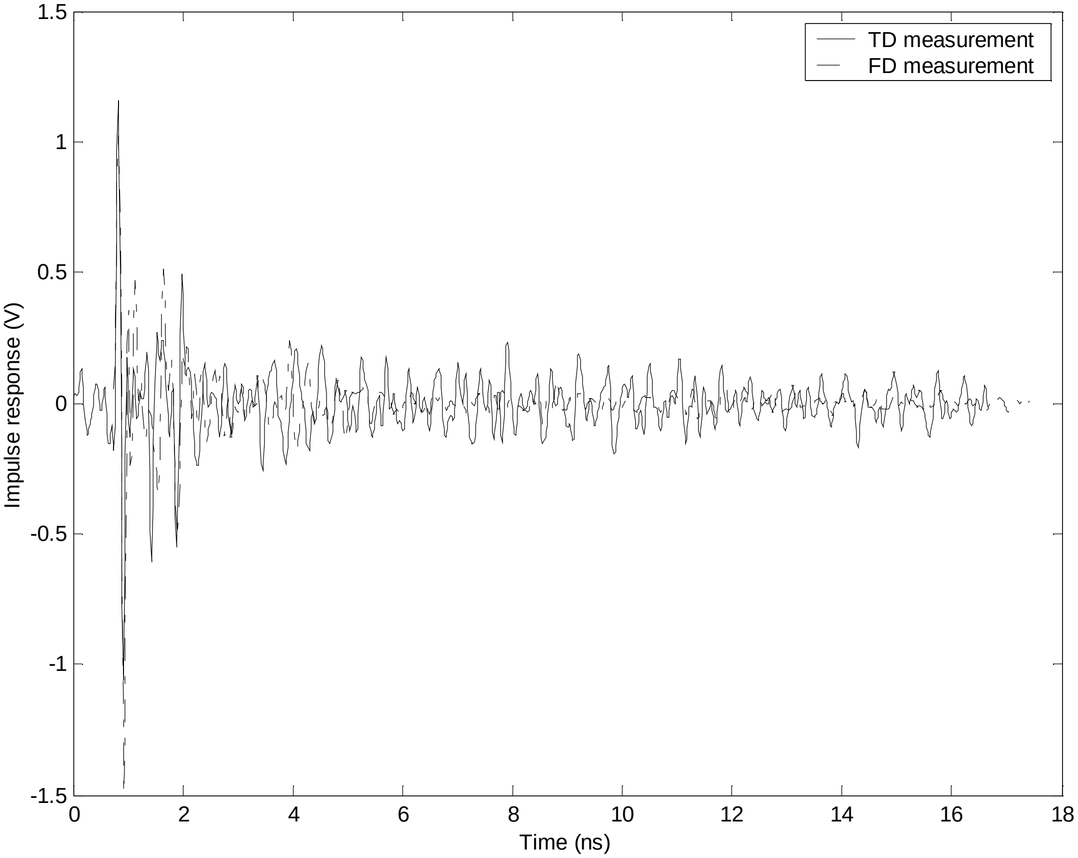
TD measurement
FD measurement
Impulse response (V)
Time (ns)
1.5
1
0.5
0
-0.5
-1
-1.5
0
2
4
6
8
10
12
14
16
18

(b)

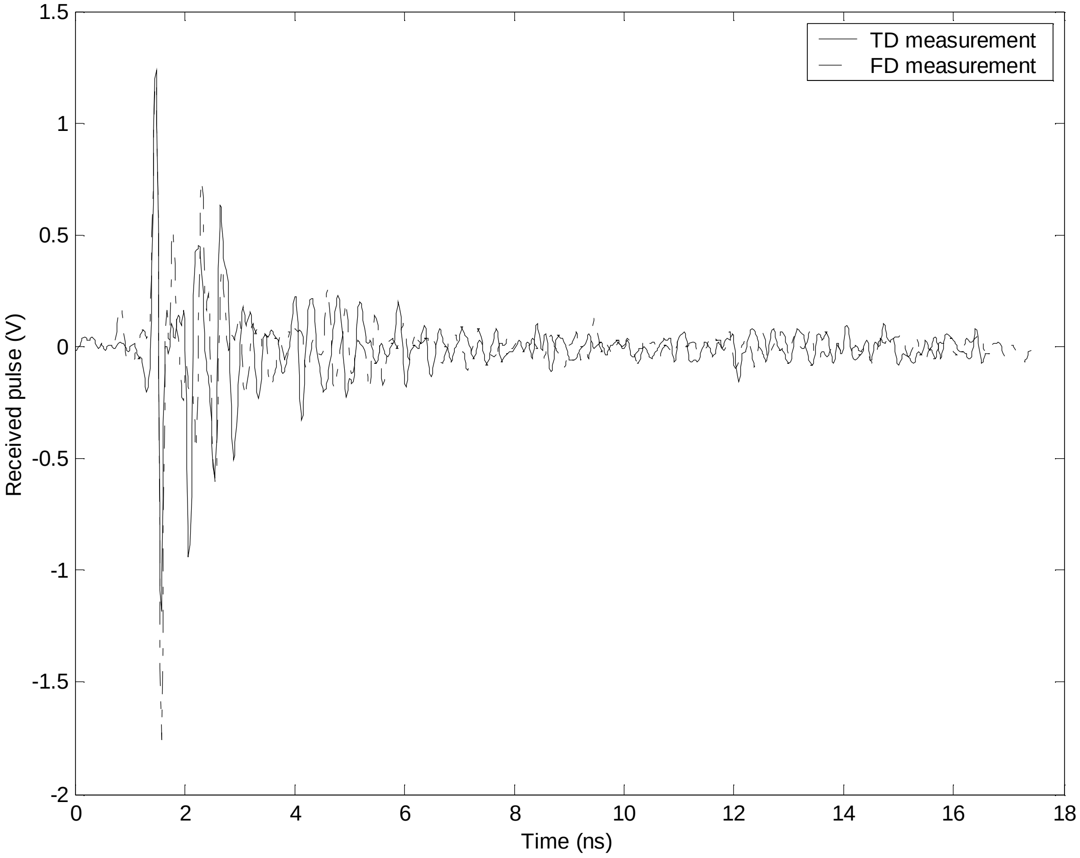

(c)

Figure C.2 LOS measurements with TEM at the location W2.E; d_A=15.4m
(- - - -) FD measurement, (—) TD measurement

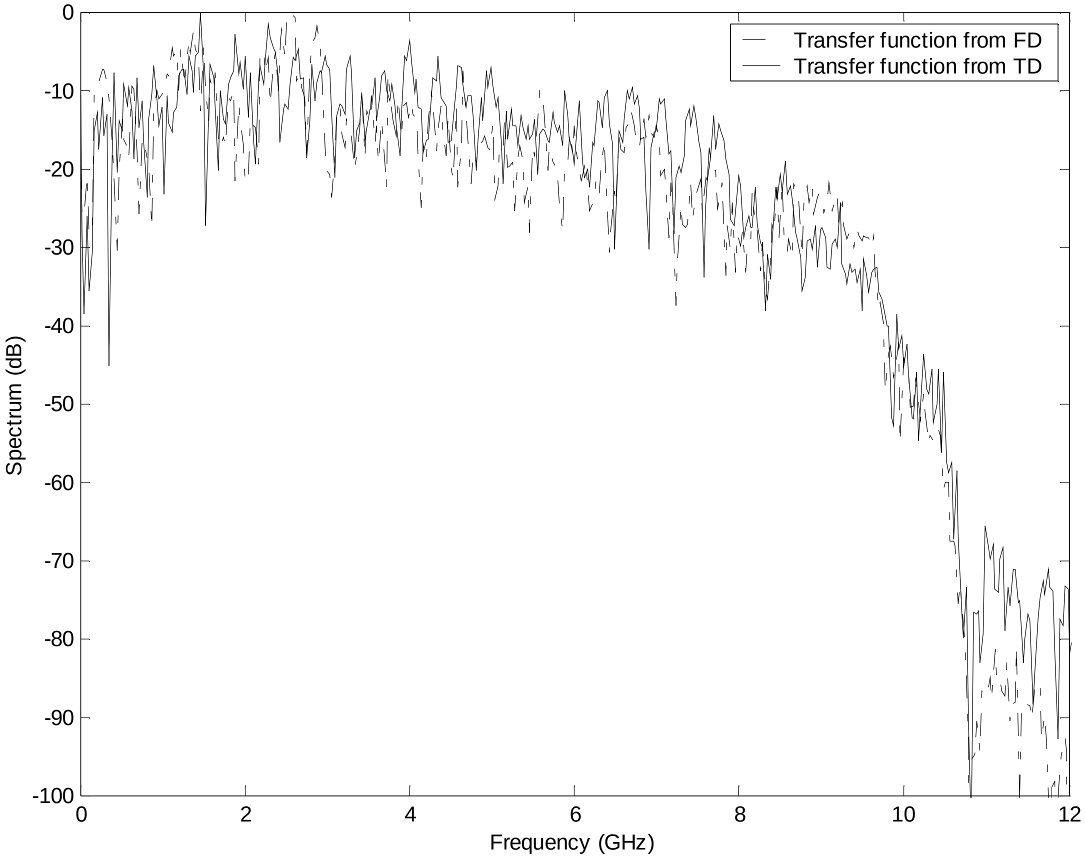
Transfer function from FD
Transfer function from TD
Spectrum (dB)
0
-10
-20
-30
-40
-50
-60
-70
-80
-90
-100
Frequency (GHz)
0
2
4
6
8
10
12

(a)

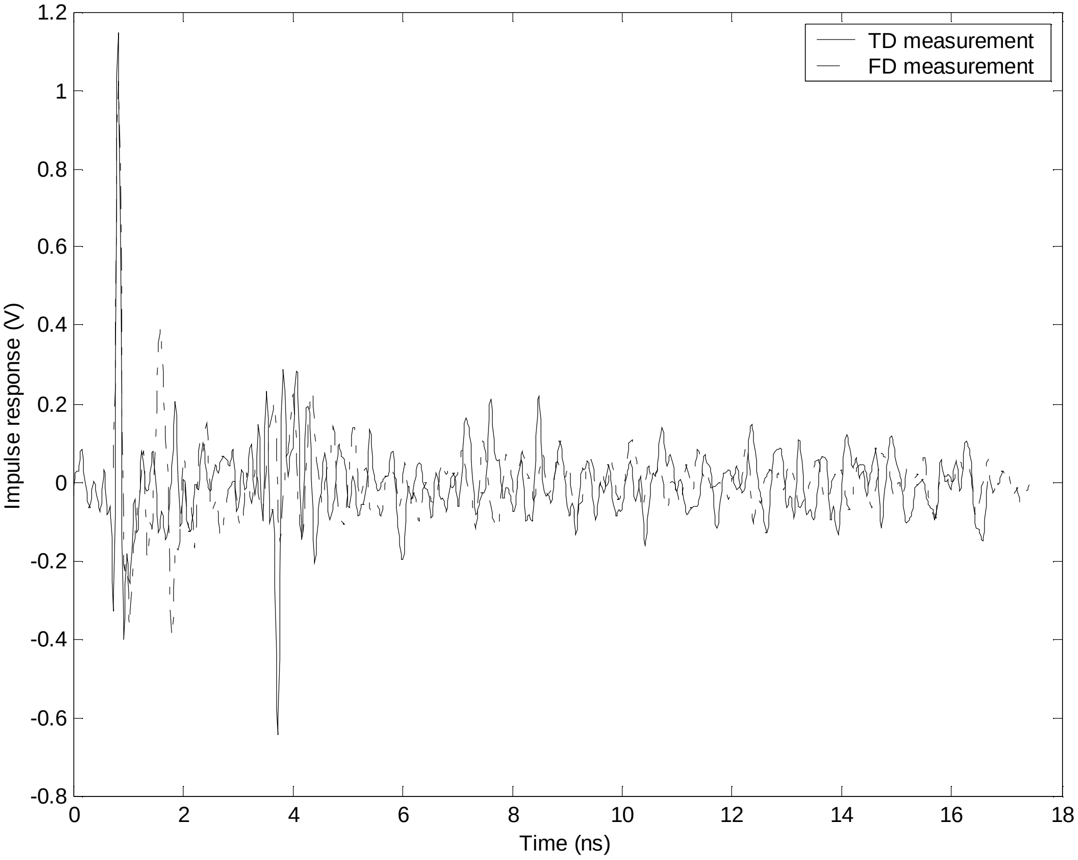
TD measurement
FD measurement
Impulse response (V)
Time (ns)
1.2
1
0.8
0.6
0.4
0.2
0
-0.2
-0.4
-0.6
-0.8
0
2
4
6
8
10
12
14
16
18

(b)

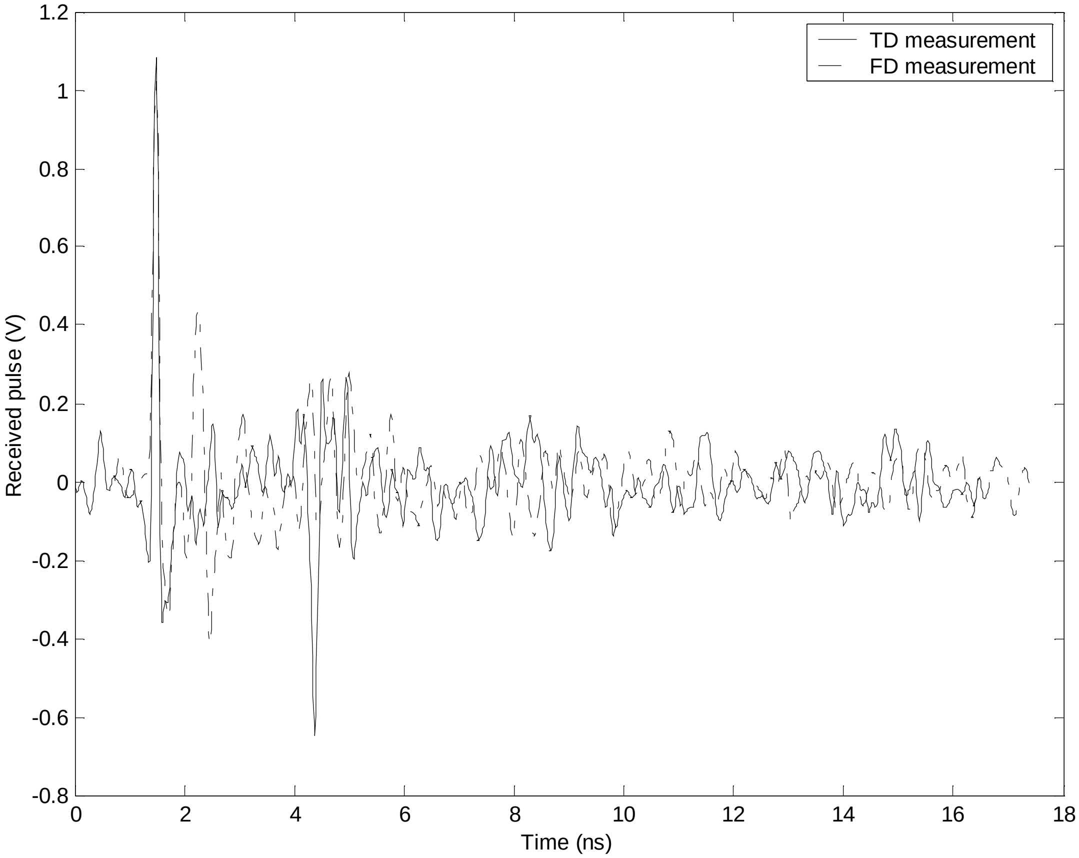

(c)

Figure C.3 LOS measurements with bicone at the location W4.E; d_A=18.2m
(- - - -) FD measurement, (—) TD measurement

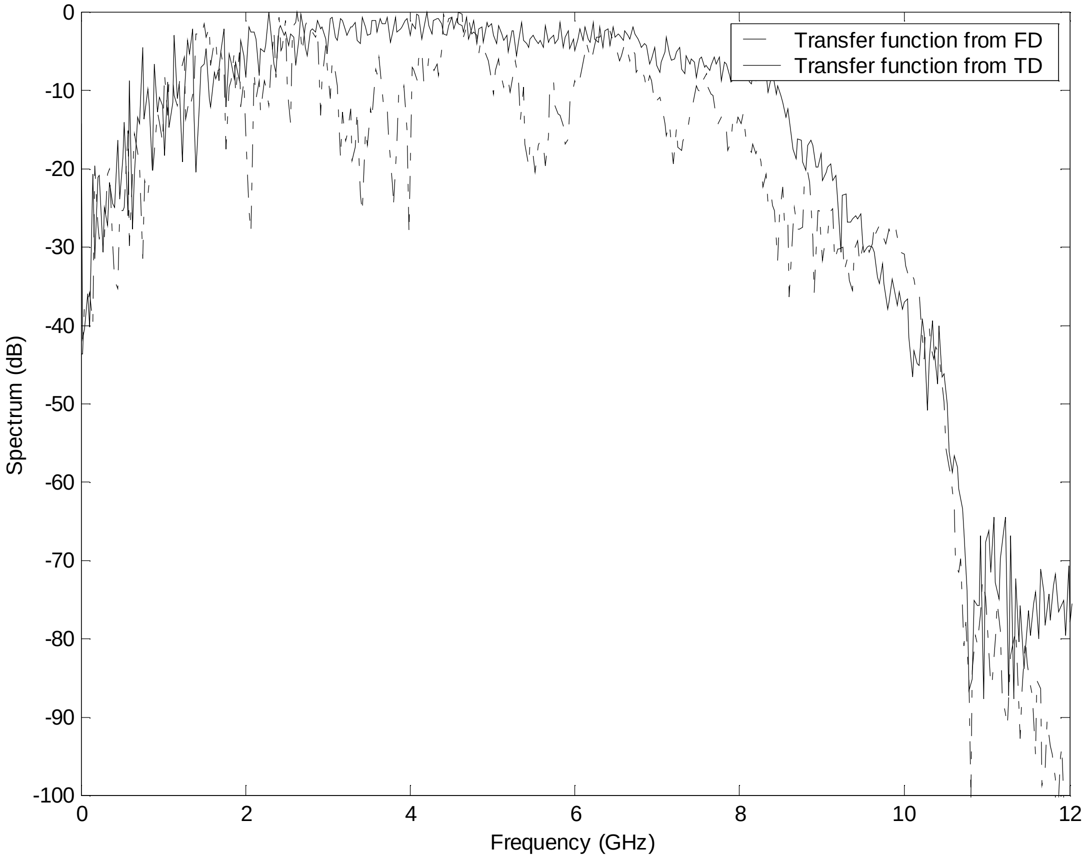
Transfer function from FD
Transfer function from TD
Spectrum (dB)
Frequency (GHz)
0
-10
-20
-30
-40
-50
-60
-70
-80
-90
-100
0
2
4
6
8
10
12

(a)

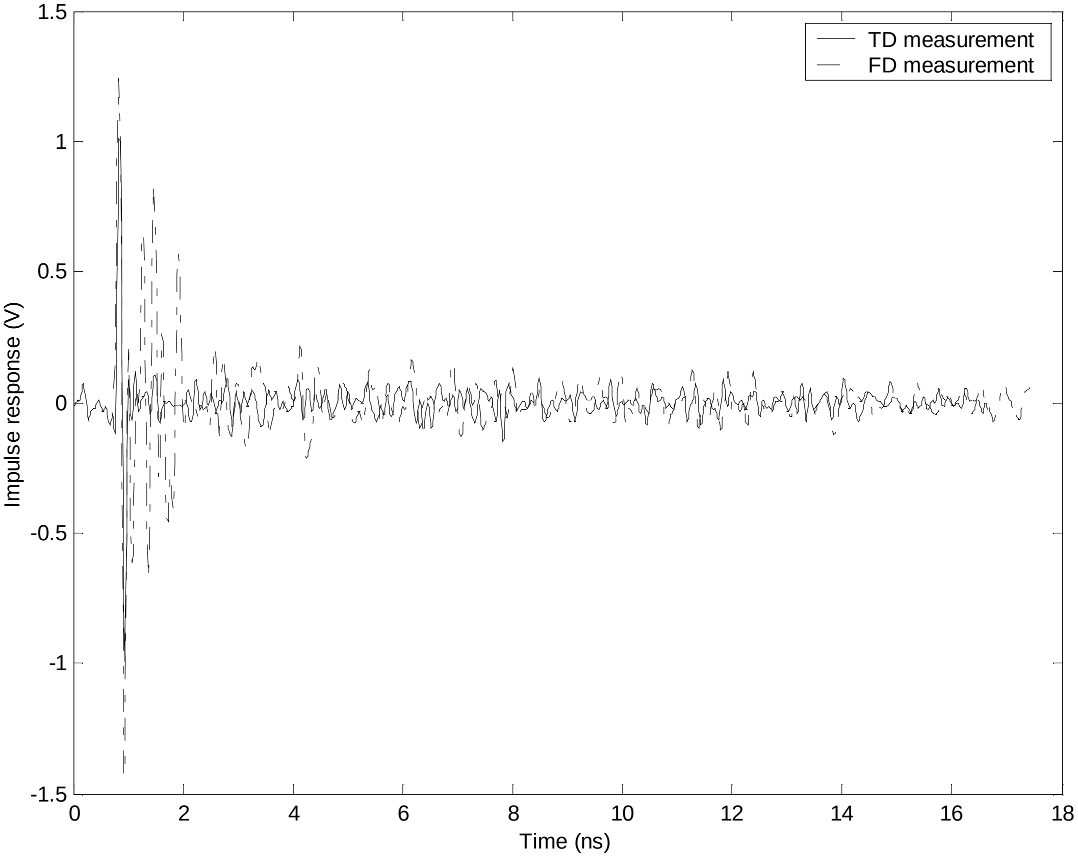

TD measurement
FD measurement
Impulse response (V)
Time (ns)
1.5
1
0.5
0
-0.5
-1
-1.5
0
2
4
6
8
10
12
14
16
18

(b)

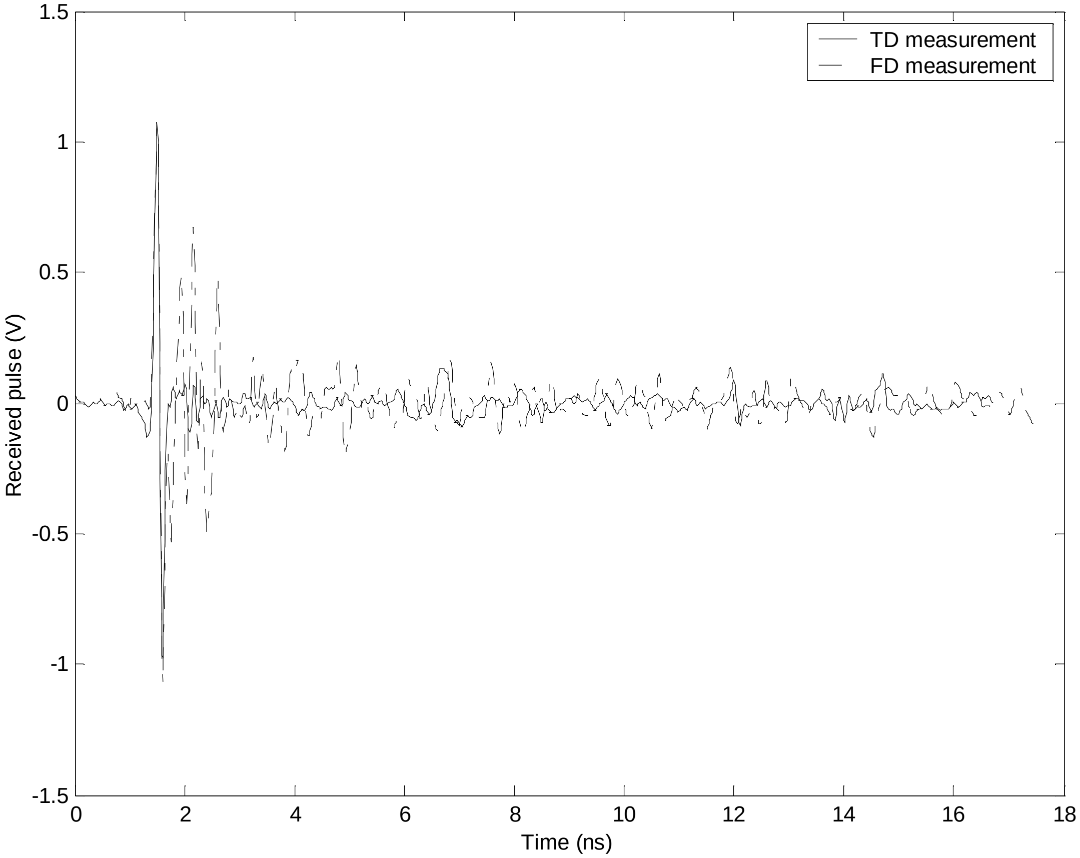

(c)

Figure C.4 LOS measurements with TEM at the location W4.E; d_A=18.2m
(- - - -) FD measurement, (—) TD measurement

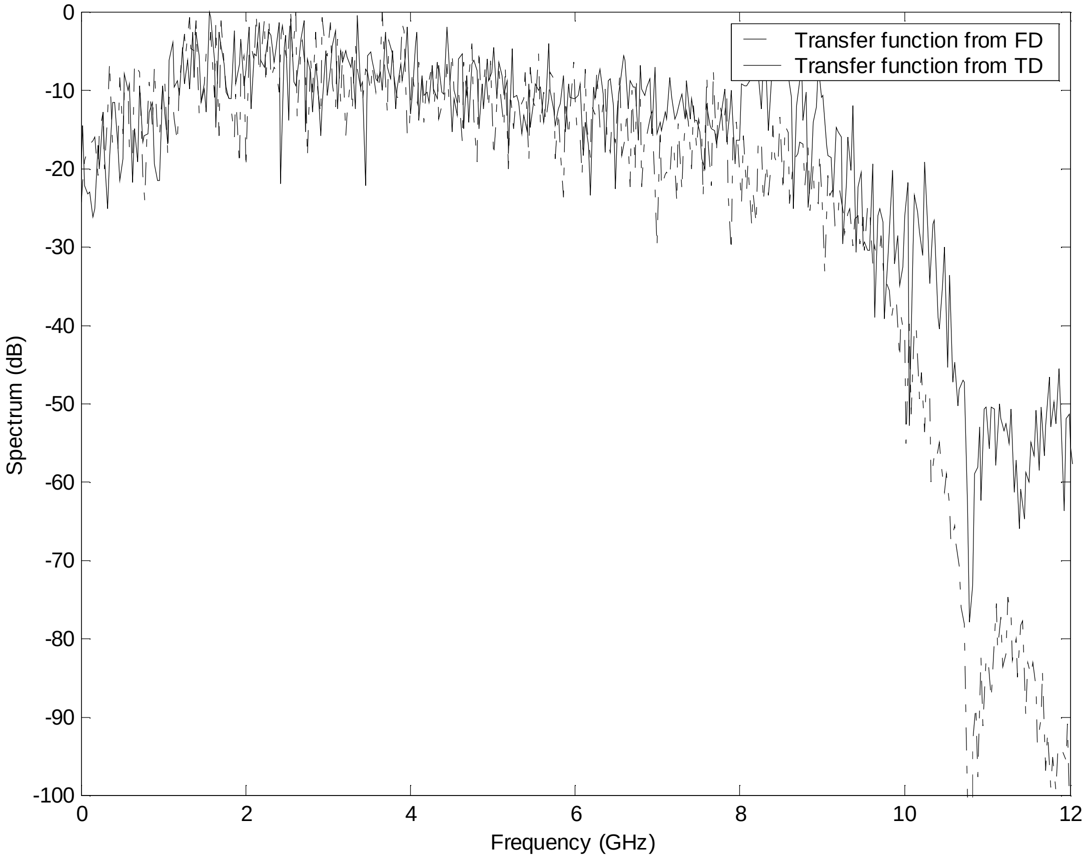
Transfer function from FD
Transfer function from TD
Spectrum (dB)
Frequency (GHz)
0
-10
-20
-30
-40
-50
-60
-70
-80
-90
-100
0
2
4
6
8
10
12

(a)

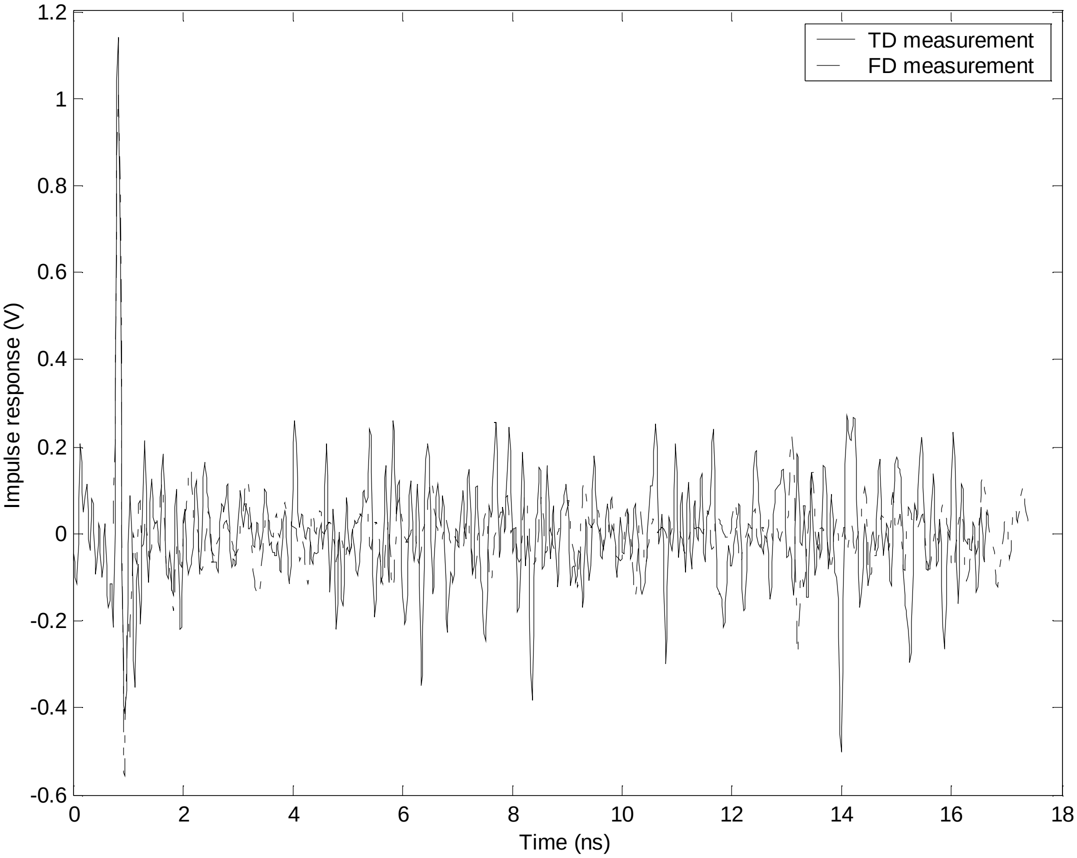
TD measurement
FD measurement
Impulse response (V)
Time (ns)
1.2
1
0.8
0.6
0.4
0.2
0
-0.2
-0.4
-0.6
0
2
4
6
8
10
12
14
16
18

(b)

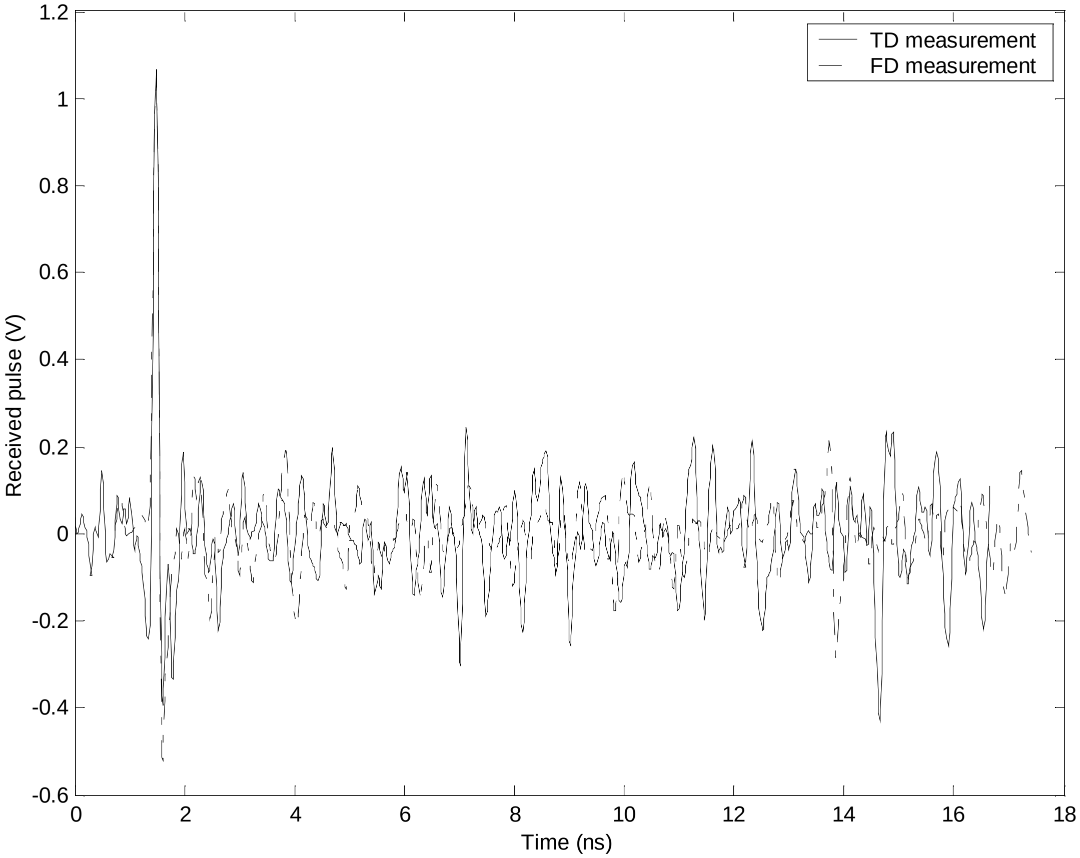

(c)

Figure C.5 LOS measurements with bicone at the location W6.B; d_A=6.2m
(- - - -) FD measurement, (——) TD measurement

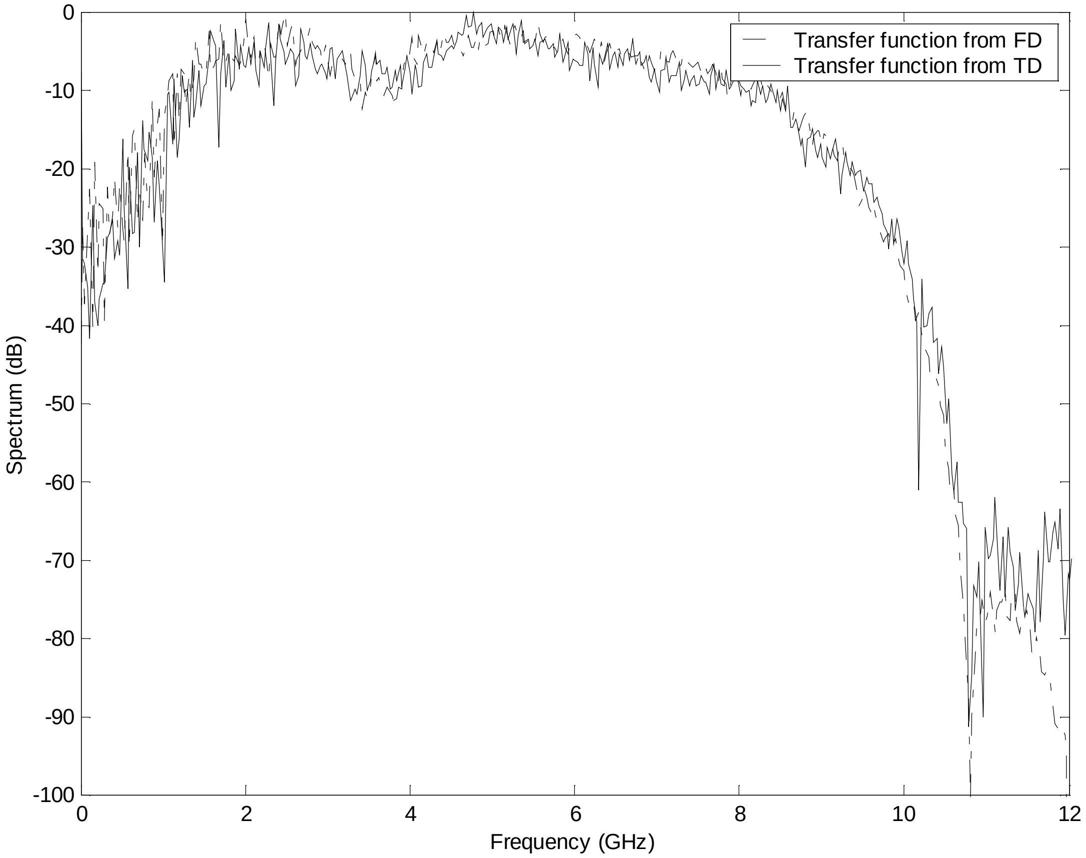

Transfer function from FD
Transfer function from TD
Spectrum (dB)
Frequency (GHz)
0
-10
-20
-30
-40
-50
-60
-70
-80
-90
-100
0
2
4
6
8
10
12

(a)

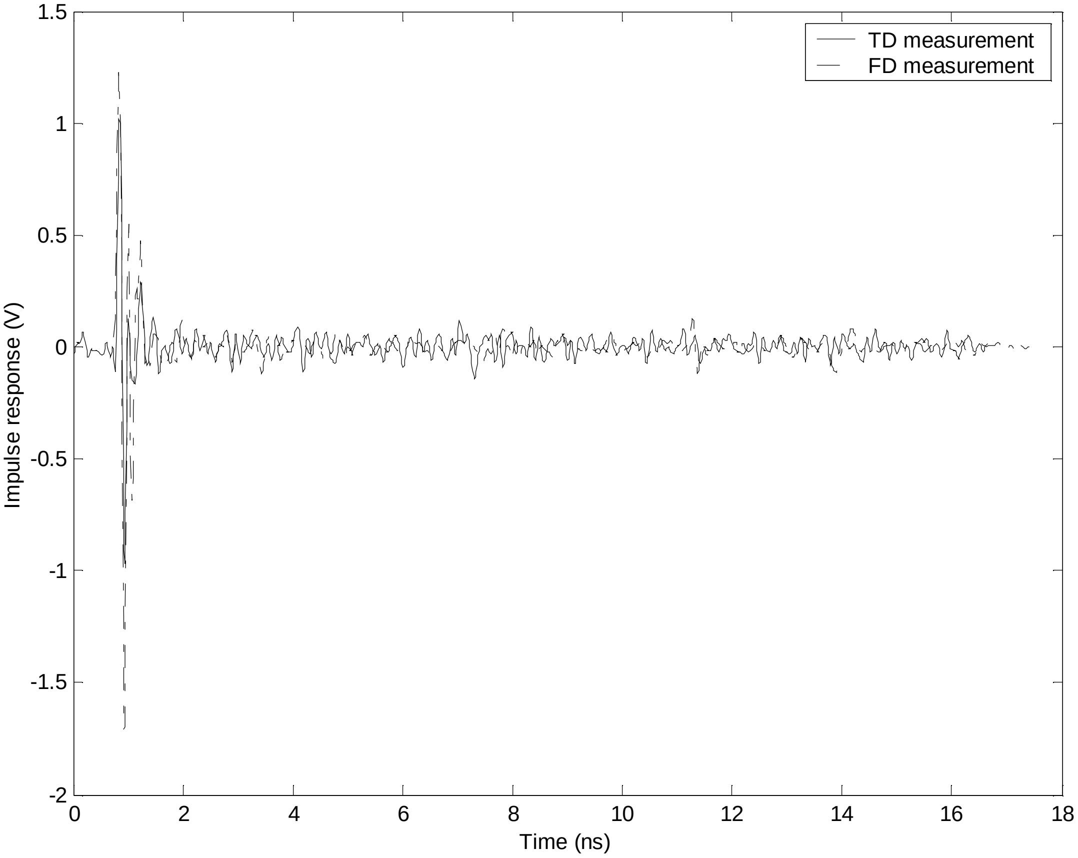
TD measurement
FD measurement
1.5
1
0.5
0
-0.5
-1
-1.5
-2
Impulse response (V)
0
2
4
6
8
10
12
14
16
18
Time (ns)

(b)

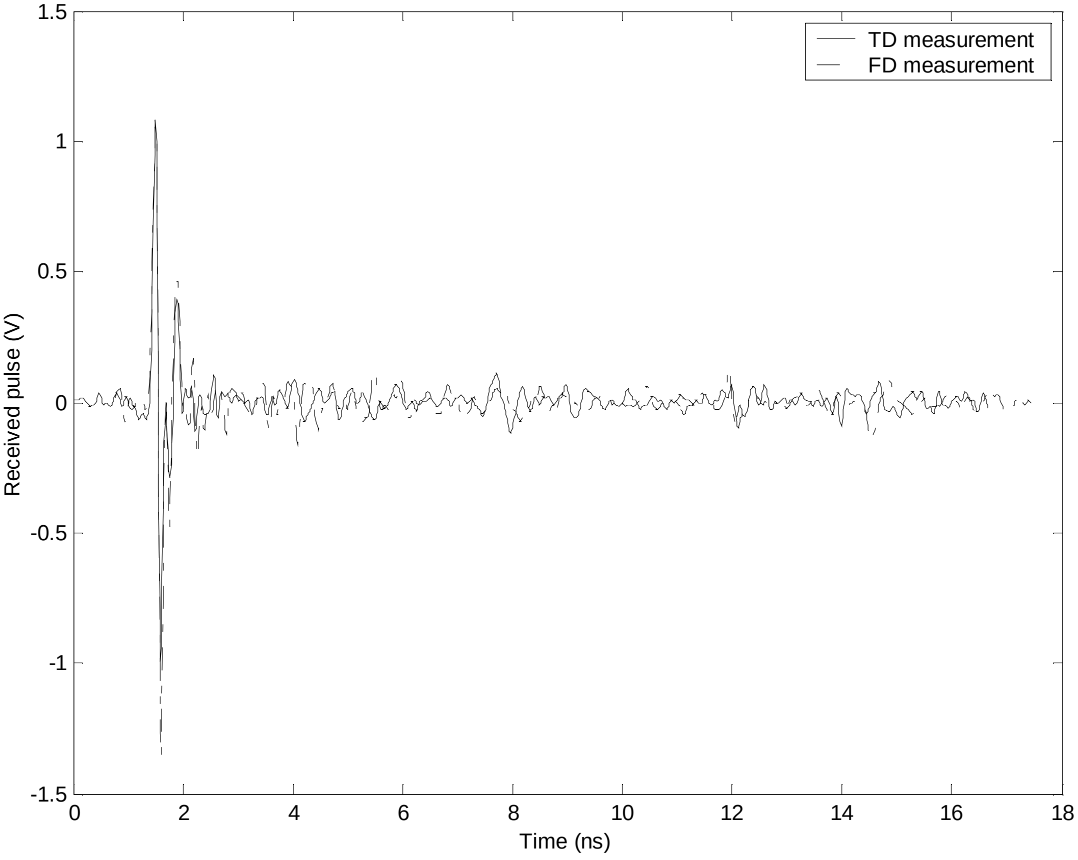

(c)

Figure C.6 LOS measurements with TEM at the location W6.B; d_A=6.2m
(- - - -) FD measurement, (—) TD measurement

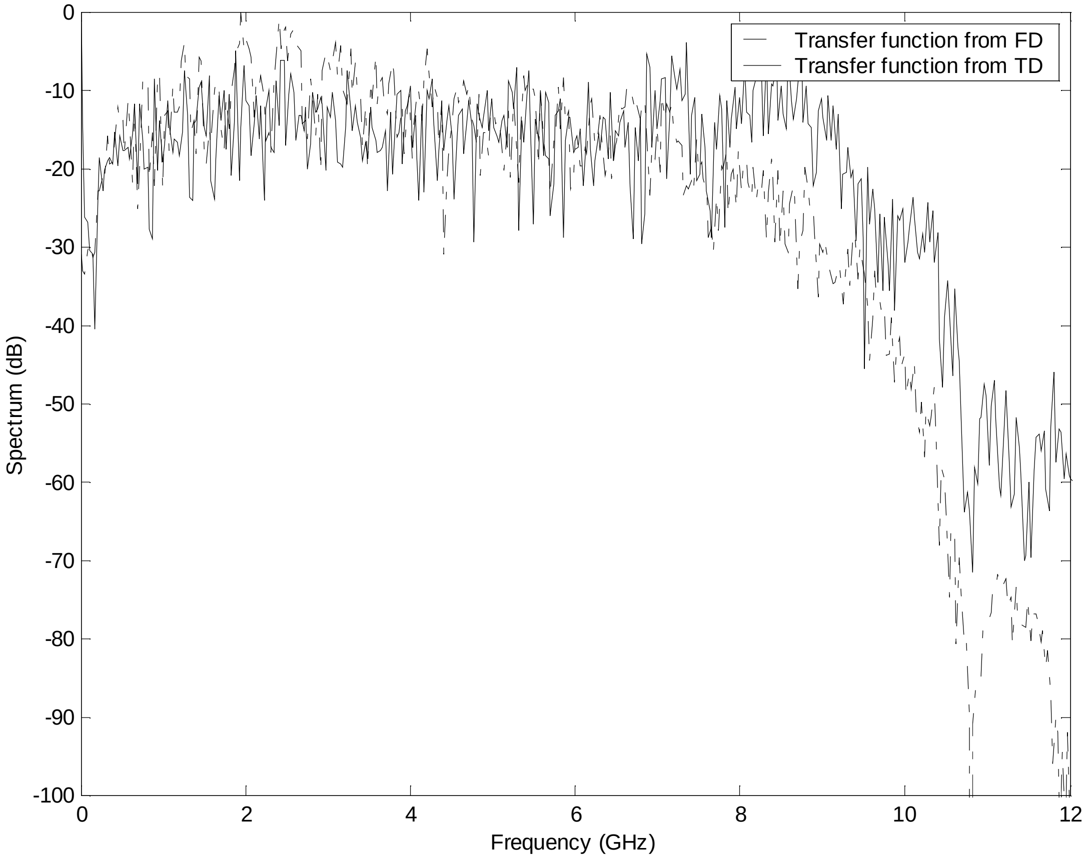
Transfer function from FD
Transfer function from TD
Spectrum (dB)
Frequency (GHz)
0
-10
-20
-30
-40
-50
-60
-70
-80
-90
-100
0
2
4
6
8
10
12

(a)

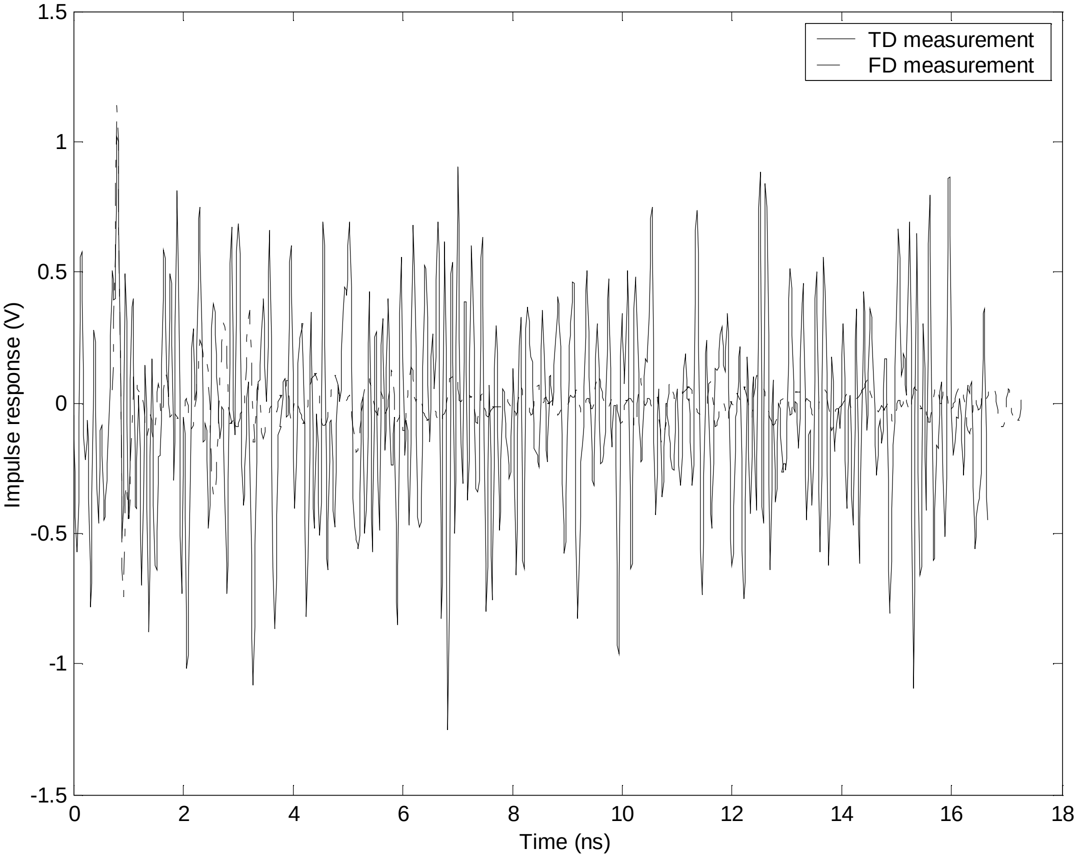

1.5
1
0.5
0
-0.5
-1
-1.5
Impulse response (V)
0
2
4
6
8
10
12
14
16
18
Time (ns)
TD measurement
FD measurement

(b)

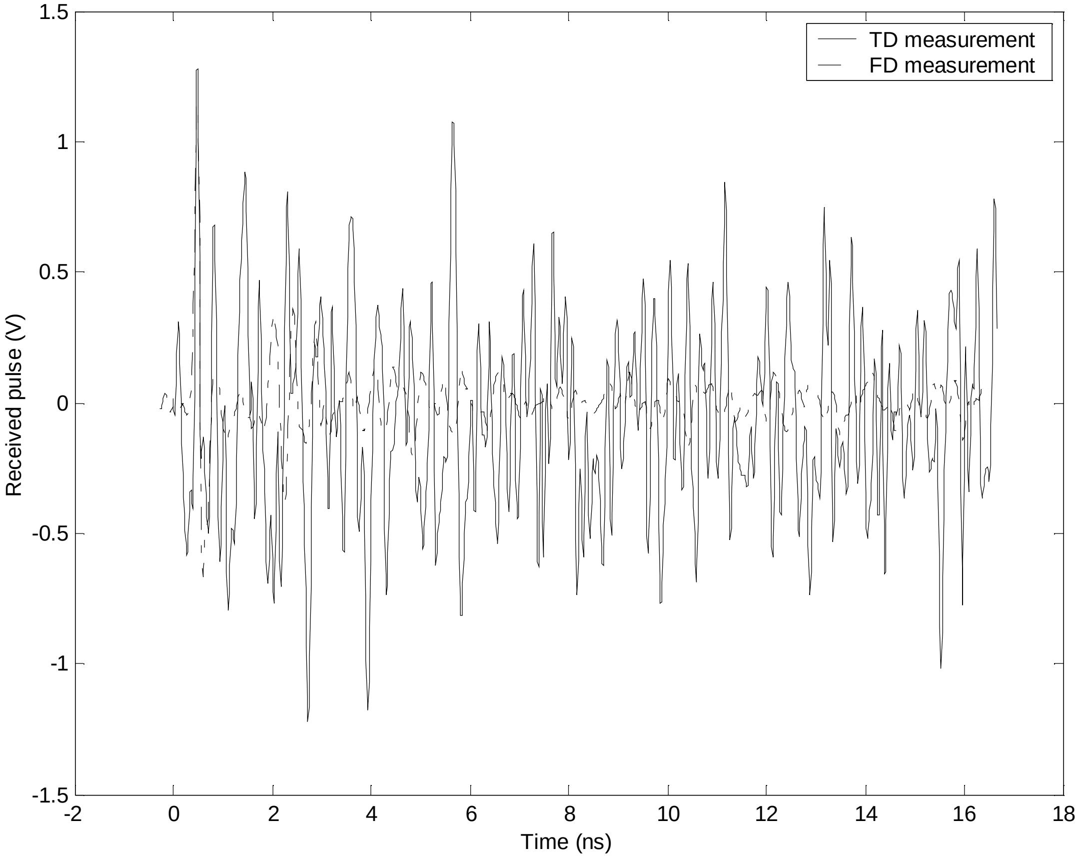

(c)

Figure C.7 LOS measurements with bicone at the location D1.B.
(- - - -) FD measurement, (──) TD measurement

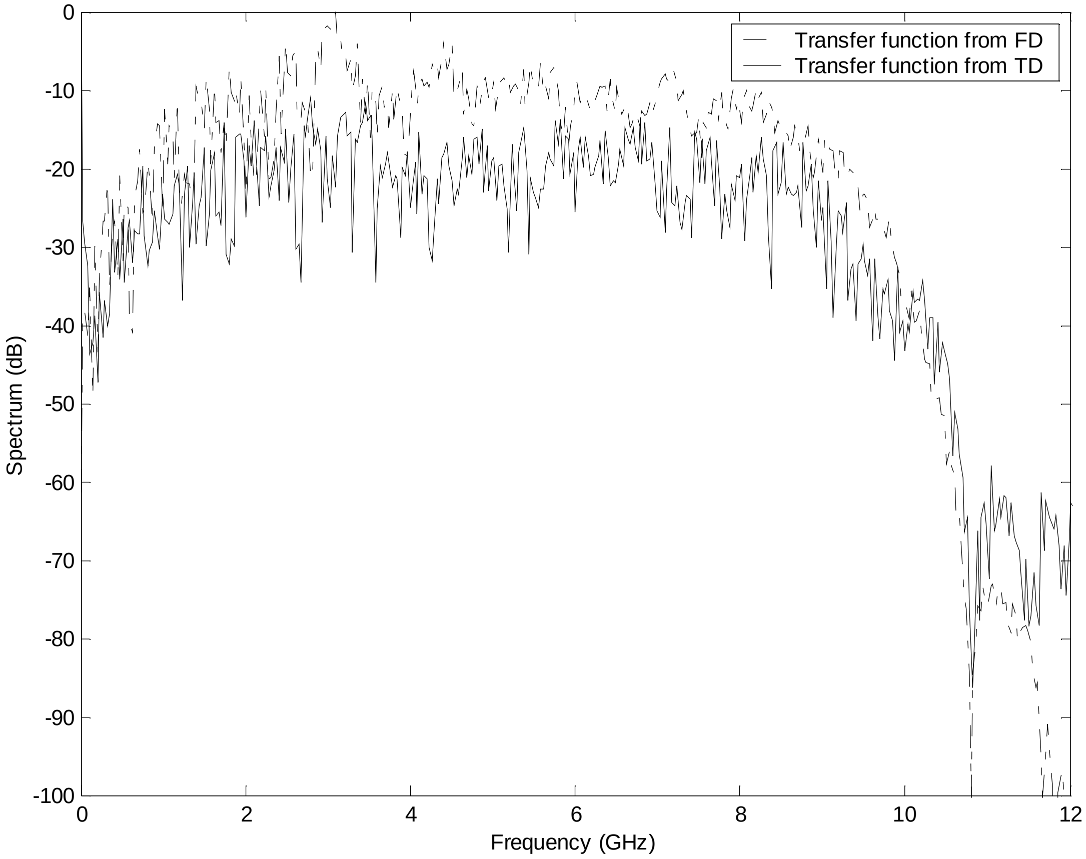

Transfer function from FD
Transfer function from TD
Spectrum (dB)
Frequency (GHz)
0
-10
-20
-30
-40
-50
-60
-70
-80
-90
-100
0
2
4
6
8
10
12

(a)

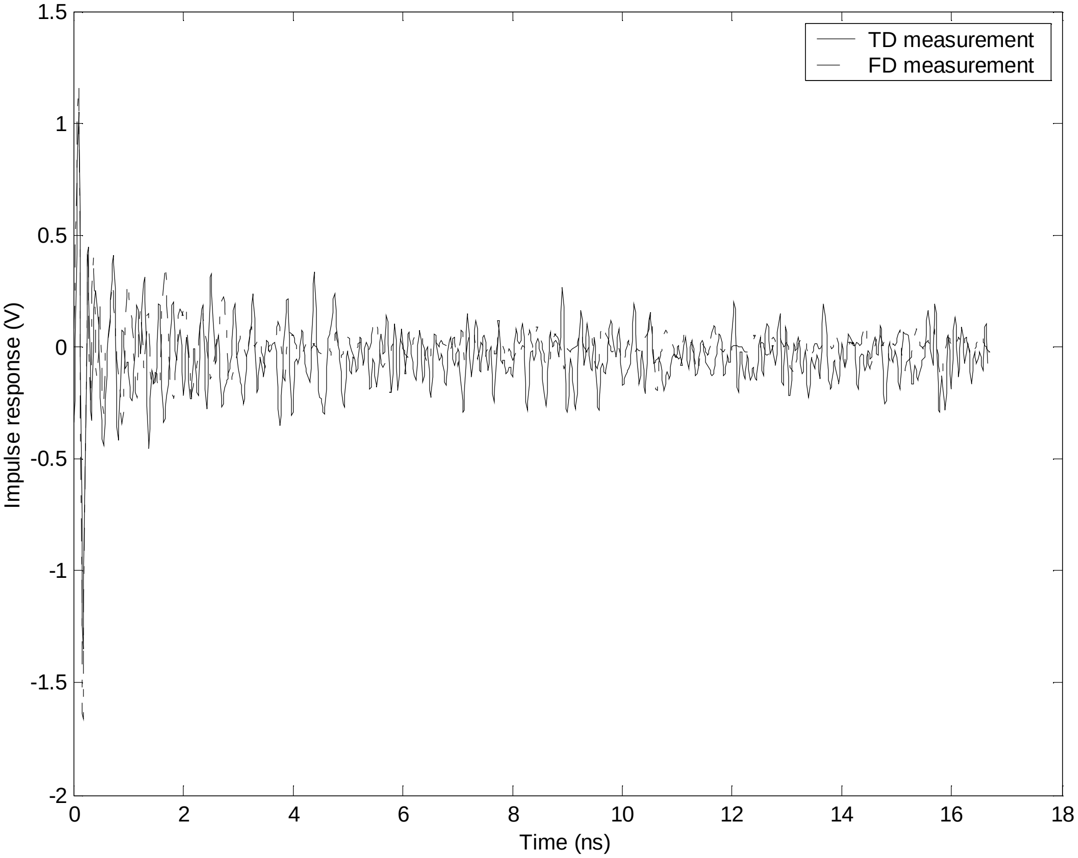

TD measurement
FD measurement
Impulse response (V)
Time (ns)
1.5
1
0.5
0
-0.5
-1
-1.5
-2
0
2
4
6
8
10
12
14
16
18

(b)

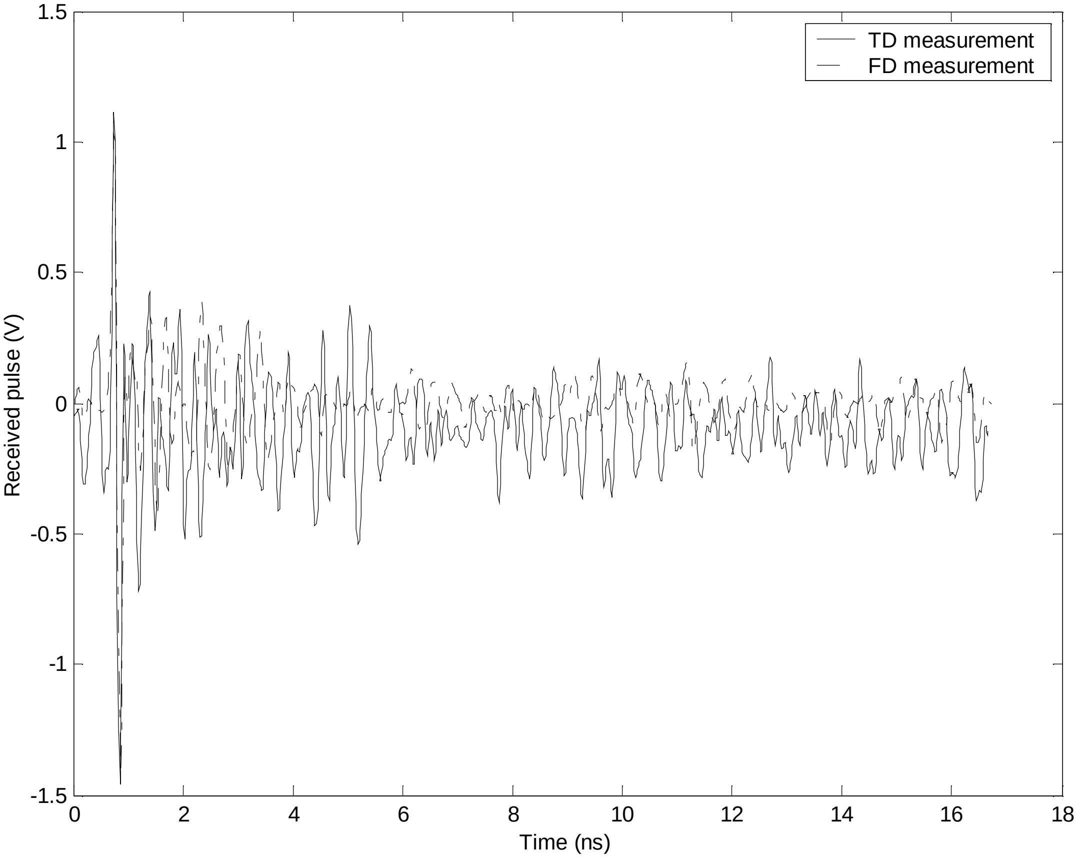

(c)

Figure C.8 Measurements with TEM at the location D1.B.
(- - - -) FD measurement, (—) TD measurement

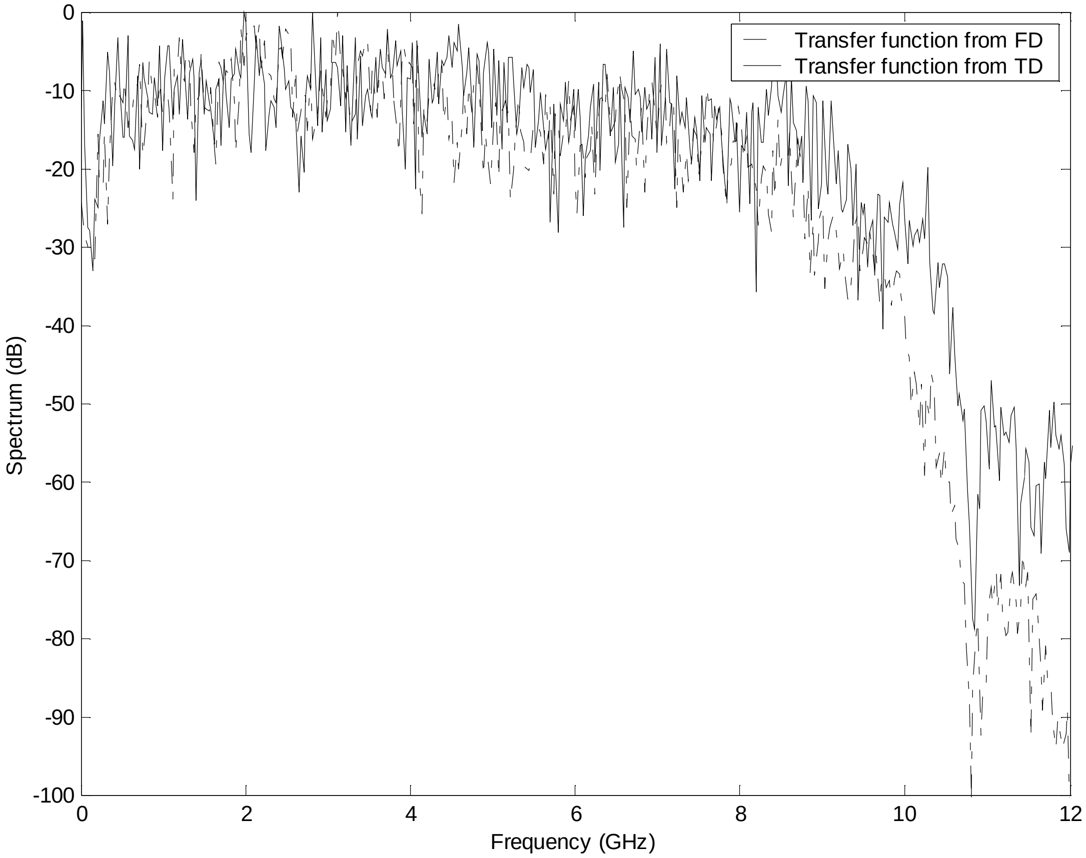
Transfer function from FD
Transfer function from TD
Spectrum (dB)
Frequency (GHz)
0
-10
-20
-30
-40
-50
-60
-70
-80
-90
-100
0
2
4
6
8
10
12

(a)

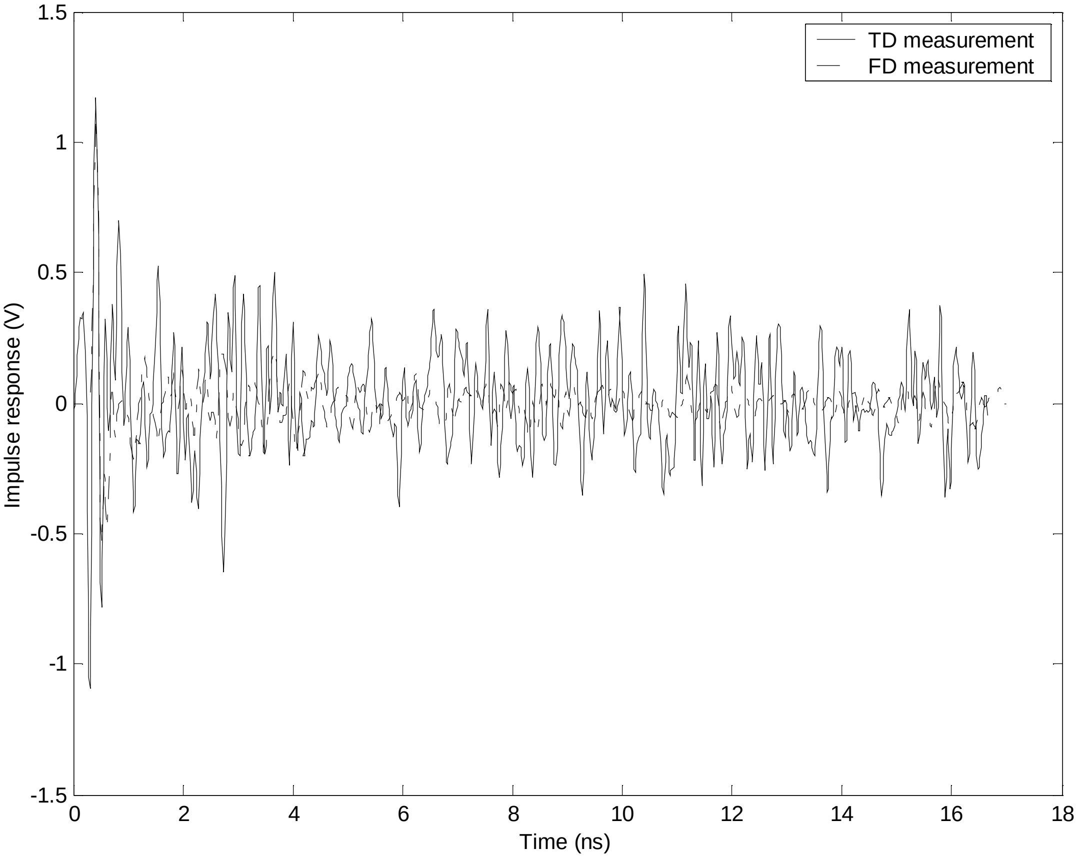

TD measurement
FD measurement
1.5
1
0.5
0
-0.5
-1
-1.5
Impulse response (V)
0
2
4
6
8
10
12
14
16
18
Time (ns)

(b)

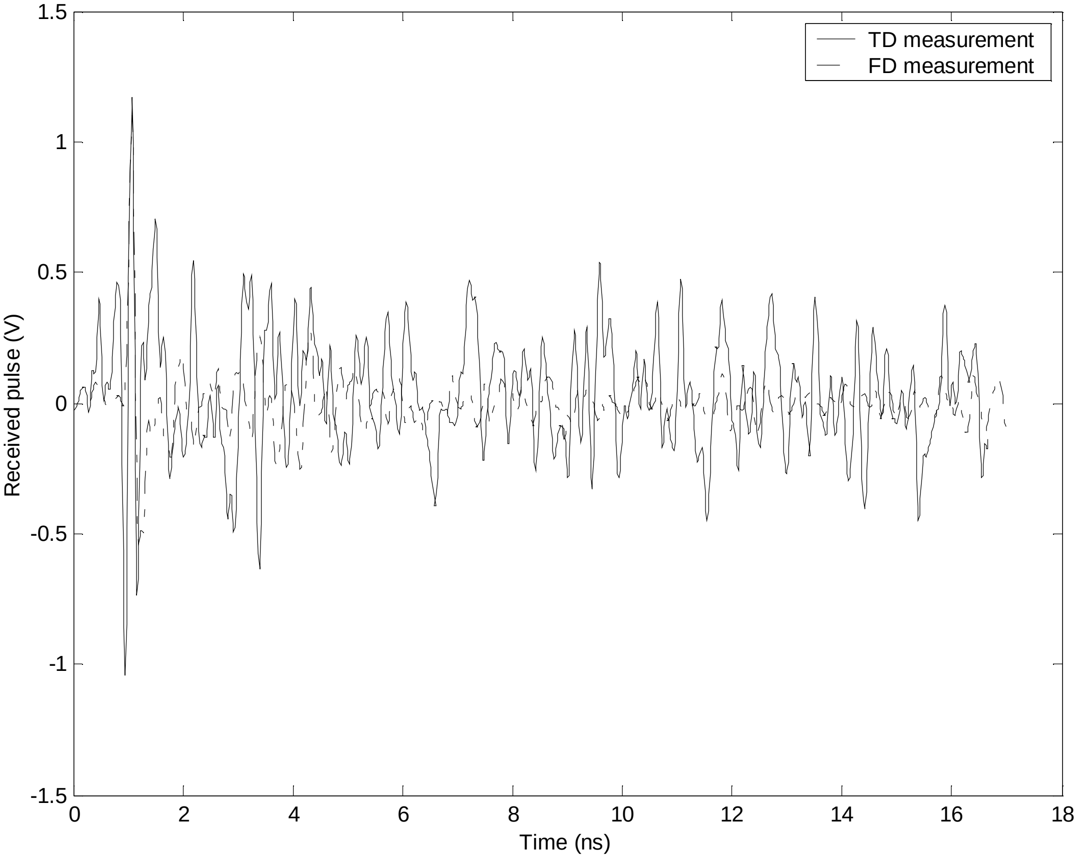

(c)

Figure C.9 Measurements with bicone at the location D4.A.
(- - - -) FD measurement, (——) TD measurement

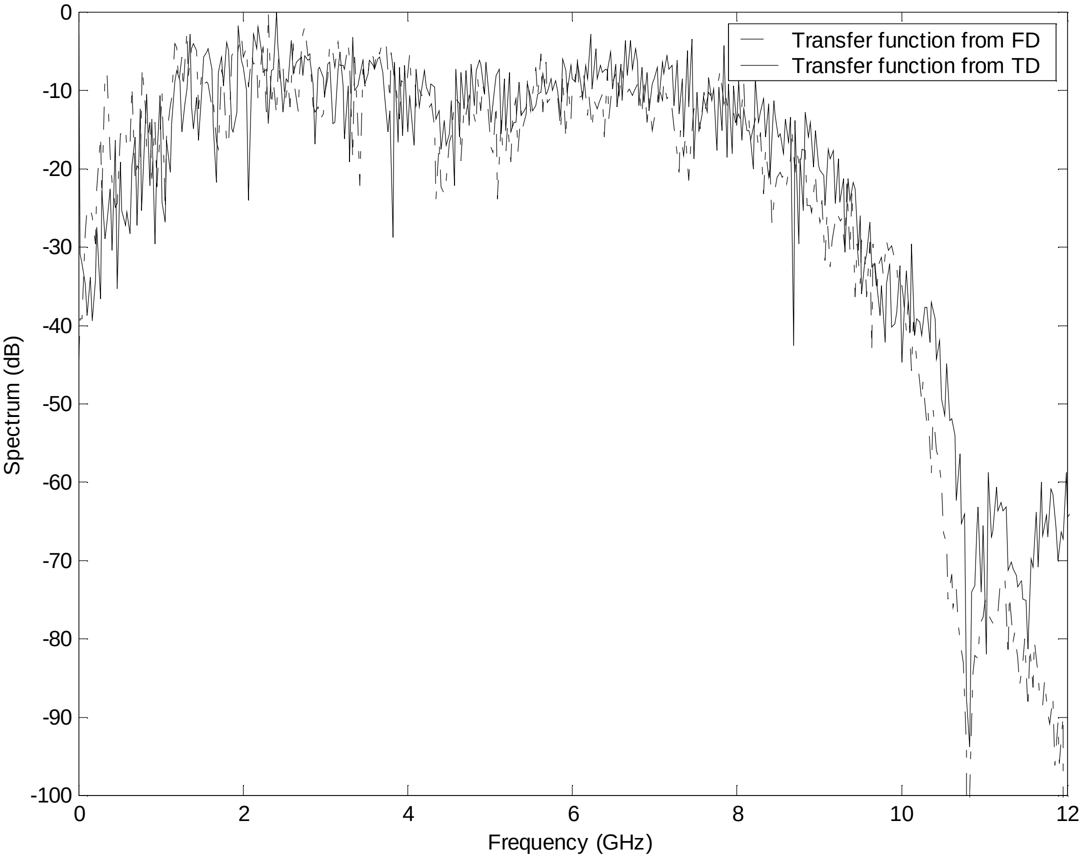
Transfer function from FD
Transfer function from TD
Spectrum (dB)
Frequency (GHz)
0
-10
-20
-30
-40
-50
-60
-70
-80
-90
-100
0
2
4
6
8
10
12

(a)

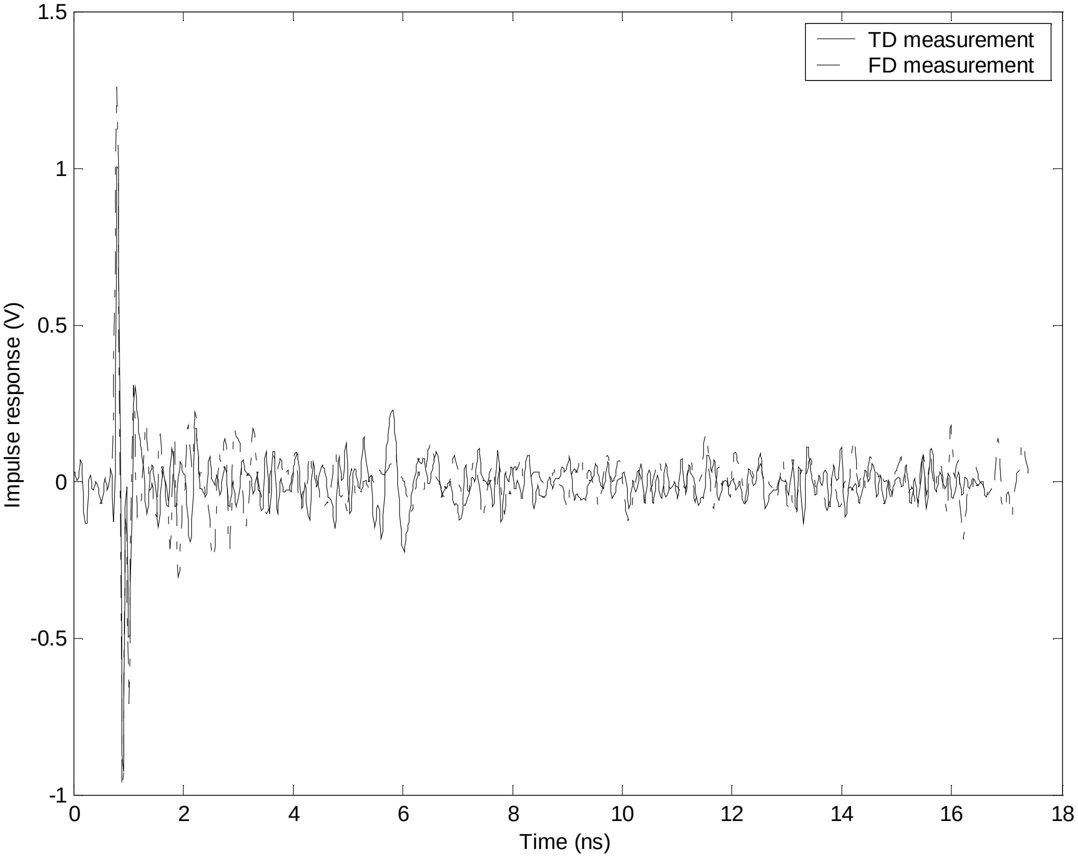
1.5
1
0.5
0
-0.5
-1
Impulse response (V)
0
2
4
6
8
10
12
14
16
18
Time (ns)
TD measurement
FD measurement

(b)

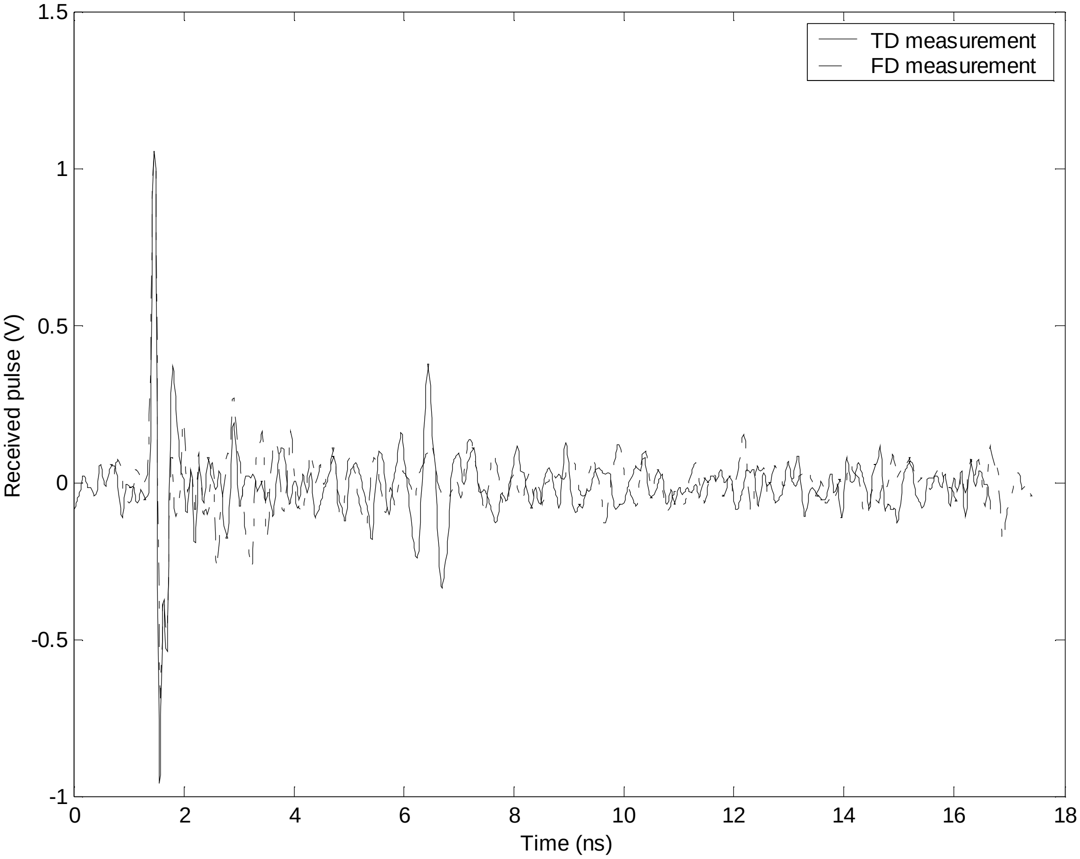

(c)

Figure C.10 Measurements with TEM at the location D4.A.
(- - - -) FD measurement, (—) TD measurement

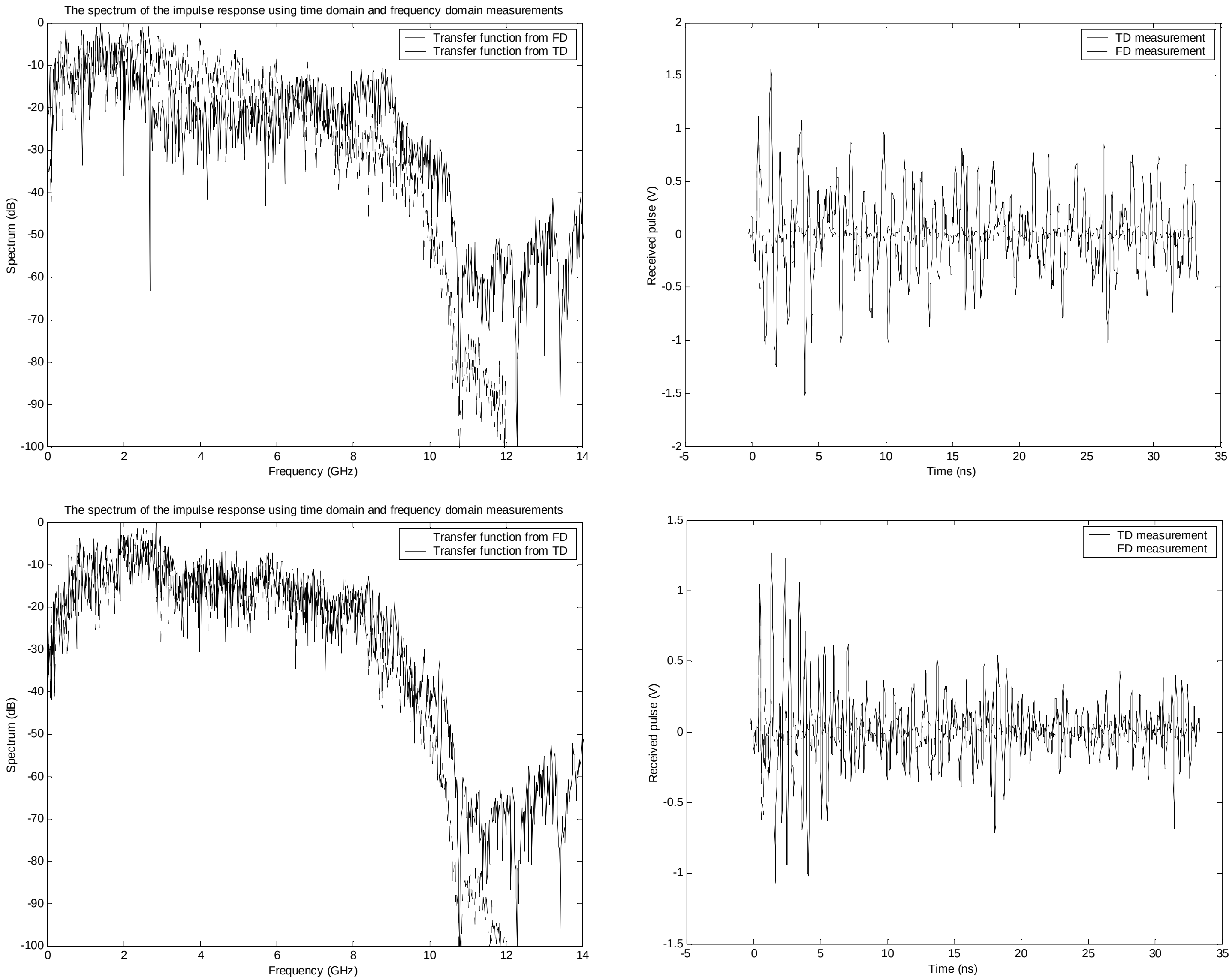

Figure C.11 Measurement results at receiver location RxC on Whittemore 3rd; top row shows the measurements by the bicone and last row by the TEM horns. (- - - -) FD measurement, (—) TD measurement

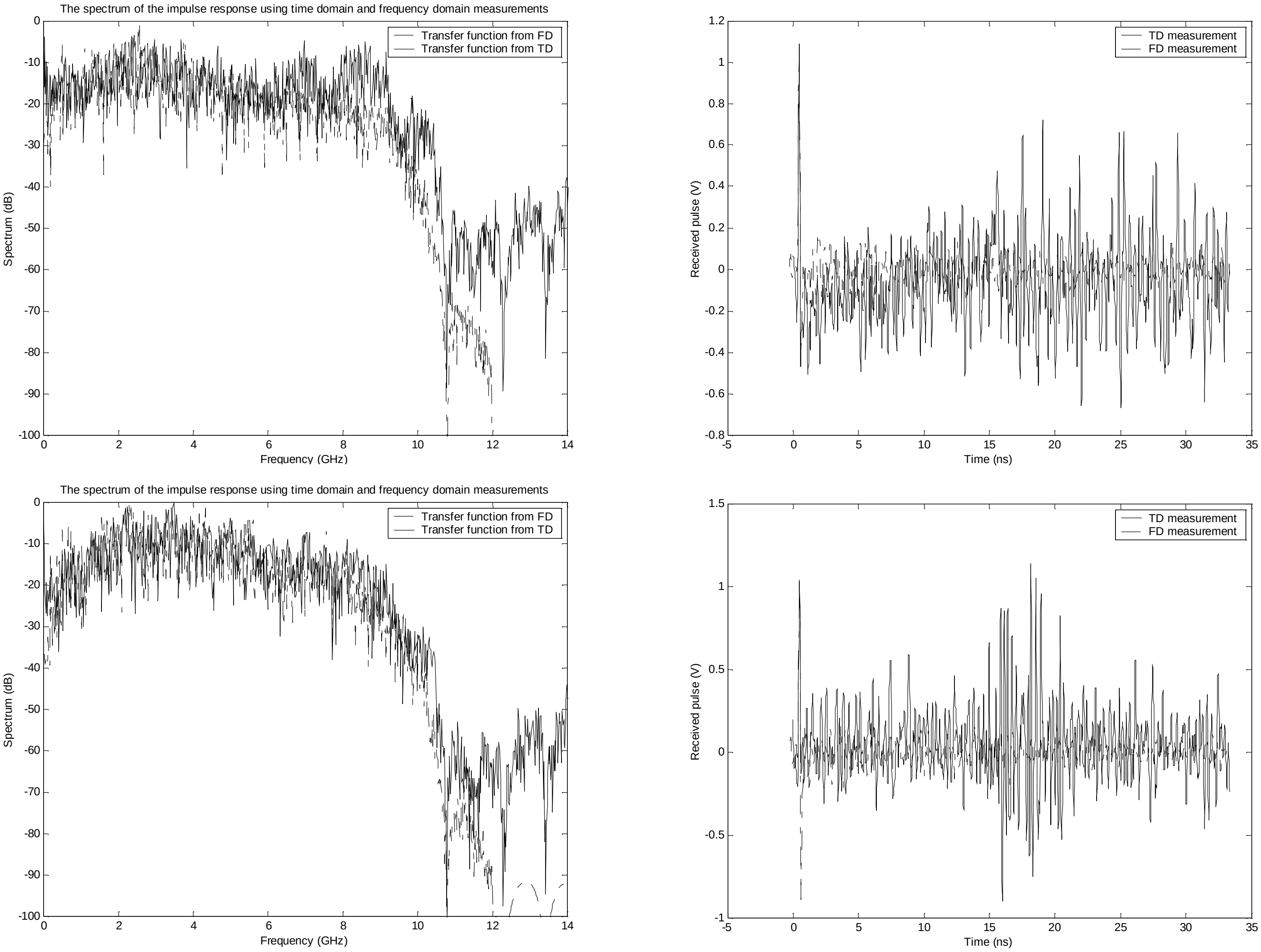

Figure C.12 Measurement results at receiver location Rx5c on Whittemore 4th; top row shows the measurements by the bicone and last row by the TEM horns. (- - - -) FD measurement, (—) TD measurement

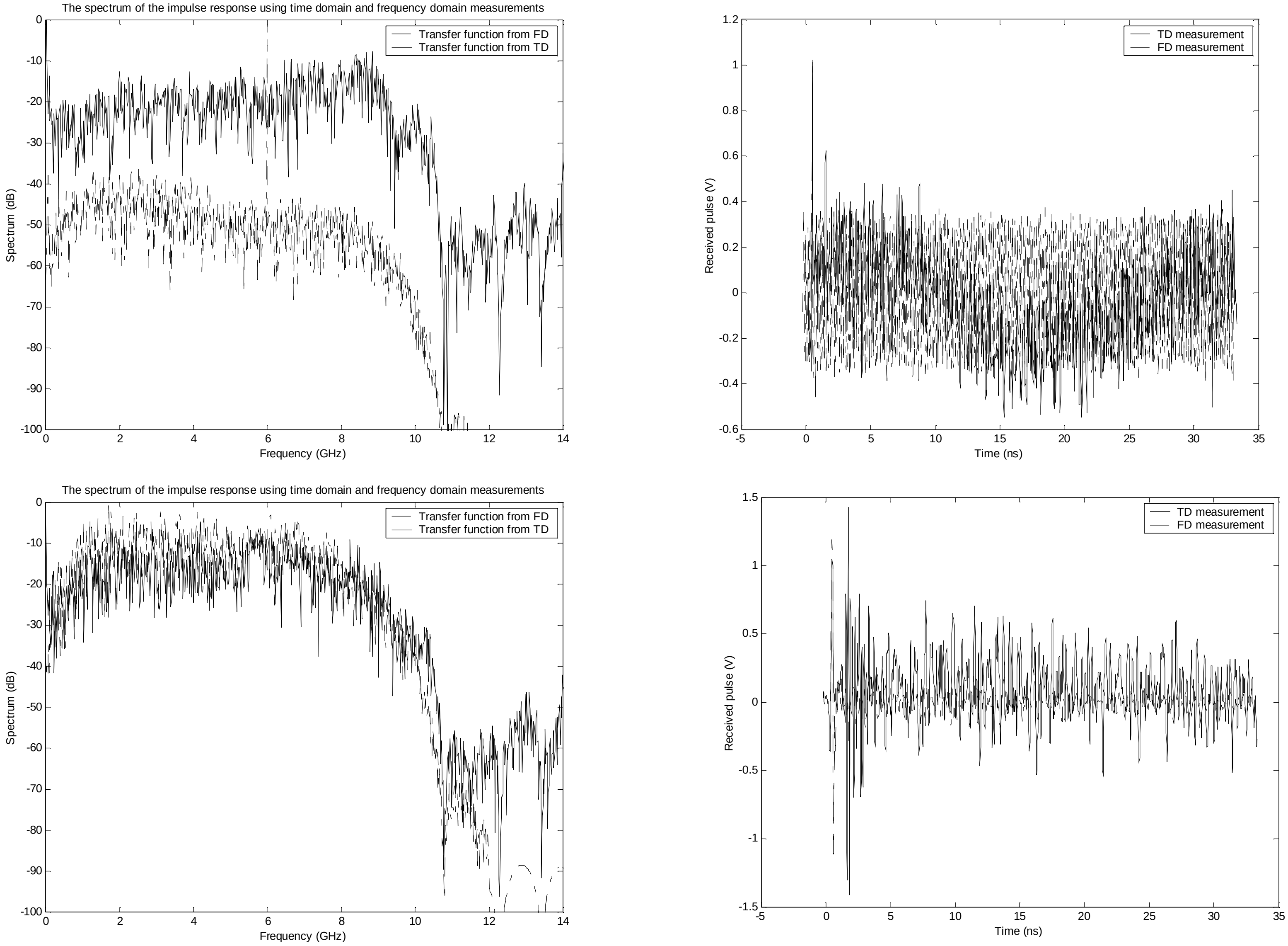

Figure C.13 Measurement results at receiver location Rx 9c on Whittemore 6th; top row shows the measurements by the bicone and last row by the TEM horns. (- - - -) FD measurement, (—–) TD measurement

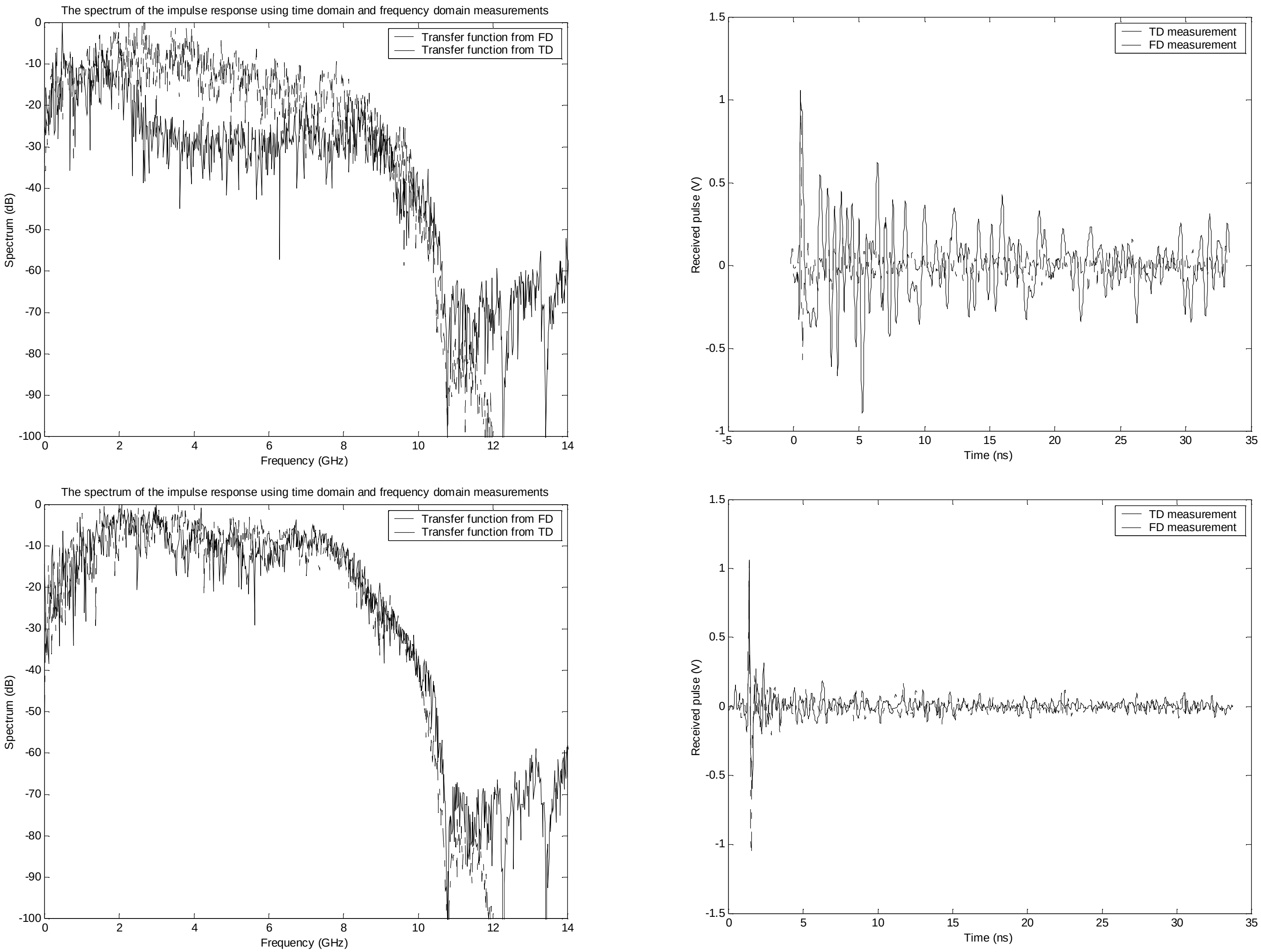

Figure C.14 Measurement results at receiver location Rx 1b on Whittemore 2nd; top row shows the measurements by the bicone and last row by the TEM horns. (- - - -) FD measurement, (──) TD measurement.

Appendix D: Transmission and Reflection for Multiple Walls

This appendix derives equations relating incident and transmitted $\vec{E}$-fields for two systems considered in Section 5.3; first is a system of two dielectric layers separated by air as illustrated in Figure D.1, and second is an equivalent dielectric medium with the same total thickness as the original system as shown in Figure D.2. The purpose of this model is to examine the impact of structural inhomogenieties on the propagation of UWB pulses.

Initially, the incident field in the two-wall system will be derived in terms of the transmitted field. A direct calculation of the same relationship will be obtained for the equivalent system. It is assumed that the separation parameters and the dielectric constants for the first system are known, and the aim is to determine the effective dielectric constant of the equivalent system such that both yield the same transmission coefficient.

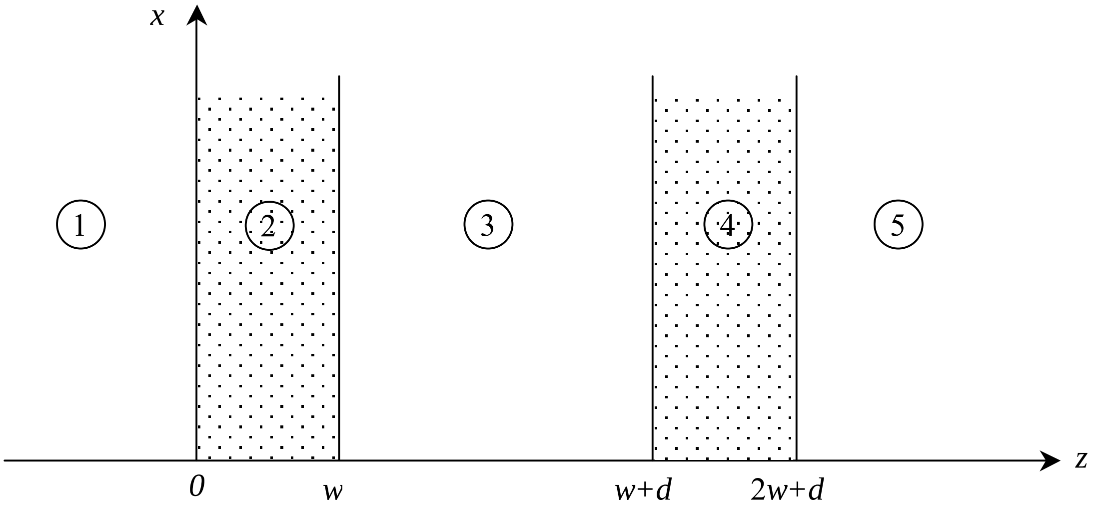

Figure D.1 The schematic diagram and dimensions for a two layer dielectric system.

$$\begin{aligned} \vec{E}_k &= \left(E_{ok}^{i} e^{-j\beta_k z} + E_{ok}^{r} e^{j\beta_k z}\right) \hat{a}_x \\ \vec{H}_k &= \left(\frac{E_{ok}^{i}}{\eta_k} e^{-j\beta_k z} - \frac{E_{ok}^{r}}{\eta_k} e^{j\beta_k z}\right) \hat{a}_y \end{aligned} \tag{D.1}$$

where

$$k = 1,\ 2,\ \ldots,\ 5$$

$$\eta_k = \begin{cases} \eta_o, \quad k = 1,\ 3,\ 5;\ odd \\ \eta_1 = \dfrac{\eta_0}{\eta}, \quad k = 2,\ 4;\ even \end{cases}$$

$$\beta_k = \begin{cases} \beta_o, \quad k = 1,\ 3,\ 5;\ odd \\ \beta_1 = \beta_0 n, \quad k = 2,\ 4;\ even \end{cases}$$

and η is the characteristic impedance, β denotes the phase constant, and n is the refractive index of the medium. Imposing the boundary conditions yields:

at $z = 2w + d$:

$$E_{o5}^{i} e^{-j\beta_0(2w+d)} = E_{o4}^{i} e^{-j\beta_1(2w+d)} + E_{o4}^{r} e^{j\beta_1(2w+d)}, \tag{D.2}$$

$$\frac{E_{o5}^{i}}{\eta_o} e^{-j\beta_0(2w+d)} = \frac{E_{o4}^{i}}{\eta_1} e^{-j\beta_1(2w+d)} - \frac{E_{o4}^{r}}{\eta_1} e^{j\beta_1(2w+d)}, \tag{D.3}$$

at $z = w + d$,

$$E_{o3}^{i} e^{-j\beta_0(w+d)} + E_{o3}^{r} e^{j\beta_0(w+d)} = E_{o4}^{i} e^{-j\beta_1(w+d)} + E_{o4}^{r} e^{j\beta_1(w+d)}, \tag{D.4}$$

$$\frac{E_{o3}^{i}}{\eta_o} e^{-j\beta_0(w+d)} - \frac{E_{o3}^{r}}{\eta_o} e^{j\beta_0(w+d)} = \frac{E_{o4}^{i}}{\eta_1} e^{-j\beta_1(w+d)} - \frac{E_{o4}^{r}}{\eta_1} e^{j\beta_1(w+d)}, \tag{D.5}$$

at $z = w$,

$$E_{o2}^{i} e^{-j\beta_1 w} + E_{o2}^{r} e^{j\beta_1 w} = E_{o3}^{i} e^{-j\beta_0 w} + E_{o3}^{r} e^{j\beta_0 w}, \tag{D.6}$$

$$\frac{E_{o2}^{i}}{\eta_o} e^{-j\beta_1 w} - \frac{E_{o2}^{r}}{\eta_o} e^{j\beta_1 w} = \frac{E_{o3}^{i}}{\eta_1} e^{-j\beta_0 w} - \frac{E_{o3}^{r}}{\eta_1} e^{j\beta_0 w}, \tag{D.7}$$

at $z = 0$.

$$E_{o1}^{i} + E_{o1}^{r} = E_{o2}^{i} + E_{o2}^{r}, \tag{D.8}$$

$$\frac{E_{o1}^{i}}{\eta_o} - \frac{E_{o1}^{r}}{\eta_o} = \frac{E_{o2}^{i}}{\eta_1} - \frac{E_{o2}^{r}}{\eta_1}. \tag{D.9}$$

Solving the system of equations, (D.2) to (D.9), the overall transmission coefficient is obtained as

$$T = \frac{E_{o5}^{i}}{E_{o1}^{i}} = \left(16n^2\right)e^{j2\beta_0 w}\left[\left\{(n+1)^2 e^{j\beta_1 w} - (n-1)^2 e^{-j\beta_1 w}\right\}^2 - \left\{\left(n^2-1\right)e^{-j\beta_0 d}\left(e^{j\beta_1 w} - e^{-j\beta_1 w}\right)\right\}^2\right]^{-1} \qquad \text{(D.10)}$$

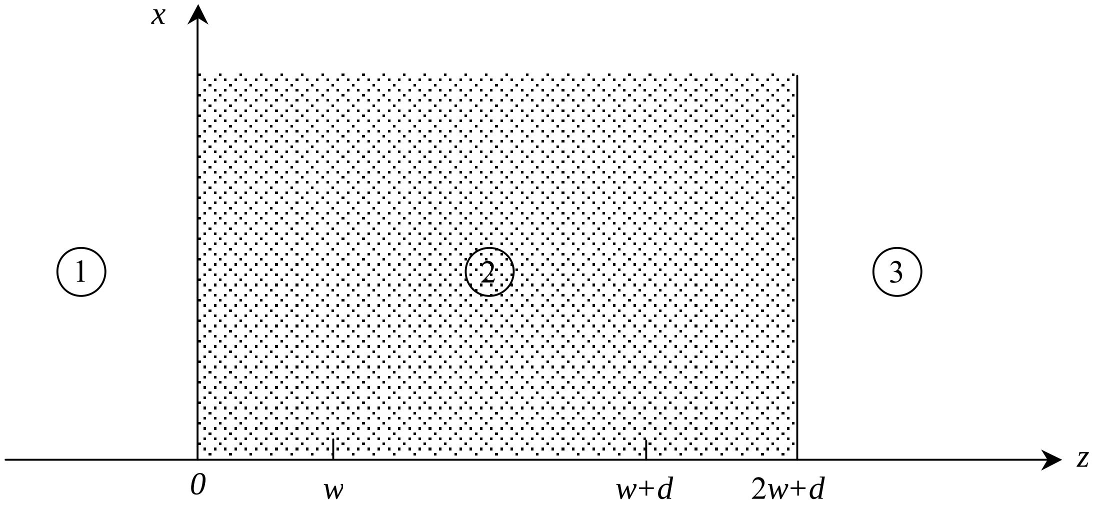

Figure D.2 The schematic and dimensions of the equivalent system.

In a similar manner, we find the following result for the transmission coefficient of the equivalent system:

$$T_{eq} = \frac{E_{o3}^{i}}{E_{o1}^{i}} = 4n_e e^{-j2\beta_0(w+d)}\left[(n_e+1)^2 e^{j\beta_e(2w+d)} - (n_e-1)^2 e^{-j\beta_e(2w+d)}\right]^{-1} \qquad \text{(D.11)}$$

Equating the right-hand sides of (D.10) and (D.11) results in:

$$\frac{(n_e+1)^2}{n_e}e^{j\beta_e(2w+d)} - \frac{(n_e-1)^2}{n_e}e^{-j\beta_e(2w+d)} = \frac{1}{4n^2}e^{j\beta_0 d}\begin{bmatrix}\left\{(n+1)^2 e^{j\beta_1 w} - (n-1)^2 e^{-j\beta_1 w}\right\}^2 \\ -\left\{\left(n^2-1\right)e^{-j\beta_0 d}\left(e^{j\beta_1 w} - e^{-j\beta_1 w}\right)\right\}^2\end{bmatrix}, \qquad \text{(D.12)}$$

which can be solved for complex n_e using two-dimensional search algorithms.

REFERENCES

[Agra98] N. P. Agrawall, G. Kumar, and K. P. Ray, “Wide-band Planar Monopole Antennas,” *IEEE Trans. Antennas Propagat.*, vol. 46, pp. 294-295, Feb. 1998.

[Attiy03] A. Attiya and A. Safaai-Jazi, “Time Domain Characterization of Receiving TEM Horn Antenna,” presented at the 2003 IEEE International Symposium on Antennas and Propagation and USNC/CNC/URSI North American Radio Science Meeting, Columbus, Ohio, Jun. 22-27, 2003.

[BaFa93] E. G. Farr, C. E. Baum, and C. J. Buchenauer, “Impulse Radiating Antennas, Part II,” in *Ultra-Wideband, Short-Pulse Electromagnetics,* H. Bertoni et al., Ed., New York: Plenum, 1993, pp.139-147.

[BaFa95] E. G. Farr, C. E. Baum, and C. J. Buchenauer, “Impulse Radiating Antennas, Part II,” in *Ultra-Wideband, Short-Pulse Electromagnetics 2,* L. Carin and L. B. Felsen, Ed., New York: Plenum, 1995, pp.159-170.

[Bory99] A. Boryssenko, “Time Domain Studies of Ultra-Wide Band Antennas,” *Proc. IEEE Canadian Conf. on Electrical and Computer Engineering*, Edmonton, Alberta, Canada, 1999, pp. 95-100.

[Chev99] Y. Chevalier, *et al.*, “A new broad band resistive wire antenna for ultra-wide-band applications,” in *Ultra-Wideband, Short-Pulse Electromagnetics 4,* L. Carin and L. B. Felsen, Ed., New York: Kluwer Academic/Plenum Publishers, 1999, pp.157-164.

[Dona96] B. P. Donaldson, M. Fattouche, and R. W. Donaldson, “Characterization of In-Building UHF Wireless Radio Communication Channels Using Spectral Energy Measurements,” *IEEE Trans. Antennas Propagat.,* vol. 44, pp. 80-86, Jan. 1996.

[Dur00] G. D. Durgin and T. S. Rappaport, “Theory of Multipath Shape Factors for Small-Scale Fading Wireless Channels,” *IEEE Transactions on Antennas and Propagation*, vol. 48, no. 5, May 2000, pp.682-693.

[Esse91] K. P. Esselle and S. S. Stuchly, “A Broad-Band Resistively Loaded V-Antenna: Experimental Results,” *IEEE Trans. on Antennas Propagat.*, vol. 39, pp. 1587-1591, Nov. 1991.

[Gha02] S. S. Ghassemzadeh, *et al.*, “A statistical path loss model for in-home UWB channels”, *IEEE Conference on Ultra Wideband Systems and Technologies*, pp. 59-64, 2002.

[Hay80] M. H. Hayes, J. S. Lim, and A. V. Oppenheim, “Signal reconstruction from phase or magnitude”, *IEEE Trans. On Acoustics, Speech, and Signal Processing,* Vol. ASSP-28, No. 6, pp. 672-680, Dec. 1980.

[Ishi91] A. Ishimaru, **Electromagnetic Wave Propagation, Radiation and Scattering**, Prentice Hall, Sec. 3-7, 1991.

[Kand86] M. Kanda, “Time-domain sensors and radiators,” in *Time-Domain Measurements in Electromagnetics.* New York: Van Nostrand Reinhold, 1986, Ch 5.

[Kei02] J. Keignart and N. Daniele, “Subnanosecond UWB channel sounding in frequency and temporal domain”, *IEEE Conference on Ultra Wideband Systems and Technologies*, pp. 25-30, 2002.

[Ko02] J. Koh, Y. Cho, and T. K. Sarkar, “Reconstruction of Non-minimum Phase Function from Only Amplitude Data,” *Microwave and Optical Technology Letters*, Vol. 35, No. 3, pp. 212-216, Nov. 2002.

[Law78] R. Lawton and A. Ondrejka, “Antennas and the Associated Time-Domain Range for the Measurement of Impulsive Fields,” National Bureau of Standards Technical Note 1008, Boulder, CO, Nov. 1978.

[Mac02] L. H. Macdo, *et al.*, “Mobile indoor wide-band 1.8 GHz sounding: measurement-based time dispersion analysis”, *Vehicular Technology Conference, 2002.* VTC Spring 2002. IEEE 55th,Vol.1, pp. 375 –379,2002.

[Mal93] J. G. Manoley and G. S. Smith, “Accurate Modeling of Antennas for Radiating Short Pulses, FDTD Analysis and Experimental Measurements,” in *Ultra-Wideband, Short-Pulse Electromagnetics,* H. Bertoni et al., Ed., New York: Plenum, 1993, pp.149-156.

[Mal95] J. G. Maloney, B. L. Shirley, and G. S. Smith, “The reception of short pulses by antennas: FDTD results and reciprocity,” in *Ultra-Wideband, Short-Pulse*

Electromagnetics 2, L. Carin and L. B. Felsen, Ed., New York: Plenum, 1995, pp.187-195.

[Mikh01] O. V. Mikheev, *et al.*, "Approximate Calculation Methods for Pulse Radiation of a TEM-Horn Array," *IEEE Trans. on Electromagnetic Compatibility*, vol. 43, pp. 67-74, Feb. 2001.

[Muq03] A. H. Muqaibel, *et al.*, "Pathloss and Time Dispersion Parameters for Indoor UWB Propagation," *IEEE Transactions on Wireless Communications*, submitted, May 2003.

[Muq03a] A. H. Muqaibel, *et al.*, "Measurement and Characterization of Indoor Ultra-Wideband Propagation," *IEEE Conference on Ultra Wideband Systems and Technologies*, Virginia, USA, 16-19 Nov. 2003.

[Muq04] A. H. Muqaibel, *et al.*, "Ultra Wideband Through-the-Wall Propagation and Material Characterization," *IEEE Transactions on Wireless Communications*, submitted, Feb. 2003.

[Ngu01] C. Nguyen, J-S. Lee, and J-S. Park, "Ultra-wideband microstrip quasi-horn antenna," *Electronic Letters*, vol. 37, pp. 731-732, 7th Jun. 2001.

[Ond93] O. E. Allen, D. A. Hill, and A. R. Ondrejka, "Time-domain Antenna Characterizations," *IEEE Trans. on Electromagnetic Compatibility*, vol. 35, pp. 339-346, Aug. 1993.

[Opp99] A. V. Oppenhein and R. W. Schafer, "Discrete-Time Signal Processing", 2nd Ed. Prince Hall, Sec. 11.3, 1999.

[Paez02] I. Páez, *et al.*, "Experimental Estimation of Wideband Radio Channel Parameters with the Use of a Spectrum Analyzer and the Hilbert Transform," *Microwave and Optical Technology Letters,* vol. 34, No.5, pp.393-397, Sep. 2002.

[Pic03] J. R. Andrews, "UWB Signal Sources & Antennas," *Application Note AN-14*, Picosecond Pulse Labs, Boulder, CO, Feb. 2003.

[Pod96] S. A. Podosenov, A. A. Sokolov, and S. V. Al'betkov, "Excitation of a V-Antenna by a Pulse Electromagnetic Field," *IEEE Trans. on Electromagnetic Compatibility*, vol.38, pp. 31-42, Feb. 1996.

[Rap89] T. S. Rappaport, “Characterization of UHF multipath radio channels in factory buildings,” *IEEE Transactions on Antennas and Propagation*, vol. 37, no. 8, pp. 1058 –1069, Aug. 1989.

[Rap96] T. S. Rappaport, **Wireless Communications, Principles & Practice**, Prentice Hall, Inc. 1996.

[Rober95] R. C. Robertson and M. A. Morgan, “Ultra-wideband impulse receiving antenna design and evaluation,” in *Ultra-Wideband, Short-Pulse Electromagnetics 2,* L. Carin and L. B. Felsen, Ed., New York: Plenum, 1995, pp.179-186.

[Sand96] F. J.Aurand, “Measurements of Transient Electromagnetic Propagation Through Concrete and Sand”. Sandia National Laboratories, Sandia Report SAND96-2254 UC-706, Livermore, CA. Sep. 1996.

[Sar98] T. K. Sarkar, “Generation of Nonminimum Phase from Amplitude-only Data,” *IEEE Trans. Microwave Theory Tech.*, Vol 46, No.8, pp. 1079-1084, Aug. 1998.

[Sch01] H. G. Schantz and L. Fullerton, “The diamond dipole: a gaussian impulse antenna,” *Antennas Propagat. Soc.*, IEEE Int. Sym., vol. 4, pp. 100-103, 8-13 Jul. 2001.

[Sch97] R. A. Scholtz and M. Z. Win , “Impulse Radio” Invited paper , *IEEE PIMRC’97*-Helsinki, Finland. pp. 245-267.

[Shla96] K. L. Shlager, G. S. Smith, and J. G. Maloney, “Accurate Analysis of TEM Horn Antennas for Pulse Radiation,” *IEEE Trans. on Electromagnetic Compatibility*, vol. 38, pp. 414-423, Aug. 1996.

[Smit02] G. S. Smith, “Teaching Antenna Reception and Scattering from a Time-domain Perspective,” *Am. J. Phys.* **70** (8), pp. 829-844, Aug. 2002.

[Str01] A. M. Street, L. Lukama, and D. J. Edwards, “Use of VNAs for wideband propagation measurements”, *Proc. Inst. Elect. Eng.,* Vol. 148, pt. I, No. 6, pp. 411-415, Dec. 2001.

[Stutz98] W. L. Stutzman and G. A. Thiele, **Antenna Theory and Design**, 2nd Ed., John Wiley & Sons, Inc., 1998.

[Tak02] T. Taniguchi and T. Kobayashi, “An Omnidirectional and Low-VSWR Antenna for Ultra-Wideband Wireless Systems,” in Radio and Wireless Conference, *RAWCON*, Aug. 2002, pp. 145 –148.

[TDC01] H. G. Schantz, (2001, Jan./Feb.). “Ultra Wideband Technology Gains a Boost from New Antennas”. [Online]. Available: http://www.AntennasOnline.com

[Tes92] F. M. Tesche, “On the use of the Hilbert transform for processing Measured CW data”, IEEE Trans. Electromag. Comp., Vol. EMC-34, No. 3,Aug. 1992, pp.259-266. F.M. Tesche, “Correction to ‘On the use of the Hilbert transform for processing Measured CW data’ ”, *IEEE Trans. Electromag. Comp.,* Vol. EMC-35, No. 1, pp.115, Feb. 1993.

[Wick93] M. C. Wicks and P. Antonik, “Polarization Diverse Ultra-wideband Antenna Technology,” in *Ultra-Wideband, Short-Pulse Electromagnetics,* H. Bertoni et al., Ed., New York: Plenum, 1993, pp.177-187.

[Win97] M. Z. Win, R. A. Scholtz, and M. A. Barnes, “Ultra-wideband signal propagation for indoor wireless communication”, *Proc. IEEE Int. Conf. Commun.,* pp. 56-60, June 1997.

[Win98b] M. Z. Win, *Ultra-Wide Bandwidth Spread-Spectrum Techniques for Wireless Multiple-Access Communications*, Ph.D. dissertation, University of southern California, Electrical Engineering, Los Angeles, 1998.

[Win02] M. Z. Win and R. A. Scholtz, “Characterization of ultra-wide bandwidth wireless indoor channels: A communication-theoretic view”, *IEEE J. Selected Areas in Commun.,* Vol. 20, No. 9, pp. 1613-1627, Dec. 2002.

[Yag99] A. E. Yagle and A. E. Bell, “One- and Two-dimensional Minimum and Nonminimum Phase Retrieval by Solving Linear Systems of Equations,” *IEEE Trans. Signal Processing*, Vol 47, No. 11, pp. 2978-2989, Nov. 1999.

[Yar02] A. G. Yarovoy, *et al.*, “The Dielectric Wedge Antenna,” *IEEE Trans. Antennas Propagat.*, vol. 50, pp. 1460-1472, Oct. 2002.

VITA

Ahmet Bayram was born on 27 November, 1980 in Lekfoşa, Cyprus. He attended Grinnell College in 1997 where he received his Bachelor's of Arts degree with highest distinction. He was also awarded upon graduation the Scholastic Athlete Award which was granted to the student with highest GPA and playing in Varsity Sports for at least three years. In 2002, Mr. Bayram joined Time Domain and RF Measurements Laboratory (TDL) at Virginia Polytechnic Institute and State University and has been working towards his Master's degree in Electrical Engineering since then. Upon graduation, he will start working as a Design Engineer and Project Manager at SAWTEK Inc. located at Orlando, FL.

Mr. Bayram worked as a teaching assistant at Virginia Tech for a year and has been involved in research afterwards. He is a member of IEEE and Phi Beta Kappa. His research interests include UWB communication systems, time- and frequency-domain channel measurements and analysis, and analysis of antennas. He has co-authored several technical reports as well as conference and journal papers.